Modal Interference Techniques for Strain Detection in Few-Mode Optical Fibers

by

Bradley Dean Duncan

Thesis submitted to the Faculty of the

Virginia Polytechnic Institute and State University

in partial fulfillment of the requirements for the degree of

Master of Science

in

Electrical Engineering

APPROVED:

Richard O. Claus

Richard O. Claus, Chairman

A. Safaai-Jazi

Ahmad Safaai-Jazi

Ronald J. Pieper

Ronald J. Pieper

April 1988

Blacksburg, Virginia

Modal Interference Techniques for Strain Detection in Few-Mode Optical Fibers

by

Bradley Dean Duncan

Richard O. Claus, Chairman

Electrical Engineering

(ABSTRACT)

Interference between the modes of an optical fiber results in specific intensity patterns which can be modulated as a function of disturbances in the optical fiber system. These modulation effects are a direct result of the difference in propagation constants of the constituent modes. In this presentation it is shown how the modulated intensity patterns created by the interference of specific mode groups in few-mode optical fibers ($V < 5.0$) can be used to detect strain. A detailed discussion of the modal phenomena responsible for the observed strain induced pattern modulation is given and it is shown that strain detection sensitivities on the order of 10^{-9} can be expected. Data taken during the evaluation of an actual experimental strain detection system based on the developed theory is also presented.

Acknowledgements

I would like to express my sincere gratitude to Dr. R.O. Claus, my graduate advisor, for his guidance, assistance and patience. Special thanks goes to Dr. A. Safaai-Jazi for his encouragement and help in understanding the many subtle concepts of modal analysis. Thanks also goes to Dr. R. Pieper for serving on my graduate Committee.

I wish also to gratefully acknowledge Brian Brennan, Bill Spillman, Jeff Lord and the other members of the Advanced Development Organization of Simmonds Precision, Vergennes, VT, for providing me with the resources with which to carry out the experimental tests of the modal domain sensing concepts developed in this thesis and for making my brief stay in Vermont a very pleasant one.

Many thanks to my fellow graduate students at the Fiber & Electro-Optics Research Center, Virginia Tech, for their advice, consultation and lasting friendship. Thanks also to Robin Rogers for her assistance in preparing the figures. And finally, sincere thanks to my parents and to my very dear friend Lucie Pelletier for their unending support and encouragement.

This work has been sponsored in part by Simmonds Precision ISD, Panton Road, Vergennes, VT.

Table of Contents

List of Illustrations

1.0 INTRODUCTION

The past several years have given rise to many optical fiber sensing techniques which may be employed in systems to detect such physical observables as temperature, pressure, displacement and strain [1]. As sensing devices, optical fibers are attractive in part due to their small size, flexibility, ruggedness and intrinsic dielectric nature. In addition, their proclivity to be highly sensitive to external perturbations is quickly making optical fibers the sensing devices of choice for many passive non-intrusive sensor applications.

Simply put, optical fiber sensors exploit the effects of perturbations and external factors on the light in the fiber. Specifically, the intensity, phase and polarization are among those properties of light which are available for alteration and the detection of these changes is the basis of most fiber optic

sensors. Unparalleled in sensitivity are the phase modulated sensors, a classic example of which is the dual-fiber Mach-Zehnder interferometer [2]. Because it is based on an absolute phase modulation scheme, however, such a sensor tends to be quite complex, with the reference phase and quadrature point often needing to be actively controlled.

By comparison, sensor systems utilizing single-fiber modal interference schemes, such as those to be discussed in this thesis, essentially have the two arms of the interferometer within the same environment. This provides for a high common mode rejection capacity while affording the system the further advantages of simplicity and increased ruggedness, with no need for couplers. Though remaining highly sensitive, as will be shown, some sensitivity will be sacrificed in a single-fiber interferometer, or modal domain sensor, due to the fact that the sensor mechanism will now be based on differential phase modulation.

Previous work with modal domain sensors has involved the detection of such observables as quasi-static strain [3,4], vibration [5], and acoustic emission [6]. Often, though, this work was done without the prior benefit of a rigorous theoretical basis for interpreting the sensor output. Also, no effort as yet has been made to theoretically predict and experimentally verify the ultimate sensitivities achieveable with given modal domain sensor systems. Finally,

no attempt has yet been made to use anything but large discrete optical components in a modal domain sensor system design. This last point will, of course, limit the practicality of single-fiber modal interference based systems.

The objectives of this thesis are therefore several. First the theoretical considerations of the behavior of the intensity patterns caused by the interference of specific mode groups in few-mode optical fibers ($V < 5.0$) will be thoroughly discussed and it will be shown how these intensity patterns, when modulated as a function of strain, can be used as a sensor mechanism. Secondly, the ultimate sensitivities achieveable with modal domain sensor systems will be investigated both theoretically and experimentally. And finally, a discussion of how modal interference techniques can be used in simple, practical sensor systems which avoid the use of large discrete optics will be presented. To begin, however, a brief review of several topics relevant to the understanding of fiber optics will be presented.

2.0 REVIEW OF BASIC FIBER OPTICS

This chapter primarily consists of a series of discussions of topics relevant to the understanding of basic fiber optics and is meant as a review. More detailed considerations of all topics may be obtained from their respective references. Subjects to be addressed include linearly polarized (LP) modes in weakly guiding fibers, photodetectors and their associated noise factors and the photoelastic effect in optical fibers under strain. We will begin, however, with a brief review of optical fiber classification.

2.1 Optical Fiber Classification

Fibers used for optical communications and sensing are waveguides made of transparent dielectrics whose function is to guide visible and infrared light. A typical optical fiber consists of an inner cylinder of glass, called the core, surrounded by a cylindrical shell of slightly lower index of refraction called the cladding. Optical fibers may be classified in terms of the refractive index profile of the core and whether one mode (single-mode) or many modes (multimode) are allowed to propagate in the waveguide. If the core has a uniform index of refraction n_1 it is called a *step-index fiber*. If the core has a nonuniform index of refraction that gradually decreases from the center toward the core-cladding interface the fiber is called a *graded-index fiber*. The cladding surrounding the core typically is of a uniform index of refraction n_2, where

$$n_2 = n_1(1 - \Delta) \tag{2.1.2}$$

in a step-index fiber. This relation is also approximately true for graded-index fibers where n_1 would then represent the index of refraction at the center of the core. The parameter Δ is called the *core-cladding index difference* and nominally $\Delta \leq 0.01$. Figure 1 shows typical dimensions of commonly used optical fibers. And finally, as the chapters to follow will be dedicated to

describing modal interference as a sensor mechanism in step-index optical fibers we note here that a typical value of the core index in a step-index fiber is $n_1 \simeq 1.458$ [7]. We now turn our attention to the guided modes allowed to propagate in step-index optical fibers.

2.2 Linearly Polarized Modes

Put simply, a *mode* in an optical fiber waveguide (or any other waveguide) is an allowable field configuration, for a given waveguide geometry, that satisfies Maxwell's equations (or the derived wave equations) and all the boundary conditions of the problem [7]. In an optical fiber a guided mode is one in which electromagnetic energy is carried along the fiber axis only and whose transverse field components decay to zero in an approximately exponential manner at distances far from the core. For these modes the integral

$$P = \int_{z=const.} |\vec{E}|^2 \, dx \, dy \,, \tag{2.2.1}$$

which is a measure of the power flow, is finite. Also, at any given operating frequency the number of guided modes is finite with each mode being associated with a cutoff frequency. That is, for a guided mode to be allowed

to exist, its cutoff must be less than the frequency of operation. It can further be shown that a mode will remain guided as long as its propagation constant β satisfies the condition

$$n_2 < \beta/k_0 \leq n_1 , \tag{2.2.2}$$

where in the case of the step-index fiber, as presently under consideration, n_1 and n_2 are the indicies of refraction of the core and cladding, respectively, and where $k_o = 2\pi/\lambda_o$, with λ_o being the free space source wavelength. Note, though, that in order for a guided mode to carry power along the fiber it must be excited by an external source. Indeed, since modes are simply analytical solutions to the wave equations in a waveguide and represent *allowed* field configurations it is quite possible to have mode solutions of a fiber (or other waveguide) which do not carry power due to their not being externally excited [8]. A detailed discussion of selective mode excitation will not be given here, but it will be seen later that the excitation of specific mode groups in an optical fiber will give rise to some very interesting sensor mechanisms. Recall, however, that for light entering a fiber to excite a guided mode it must in general satisfy the condition that it enters the core through an acceptance cone defined by the numerical aperture, or NA, of the fiber. A physical interpretation of a fiber NA is given in Figure 2 with the analytical value of NA given as

$$NA = \sqrt{n_1^2 - n_2^2} \simeq n_1\sqrt{2\Delta} \qquad (2.2.3)$$

in a step-index optical fiber. This result is derived from considering that light guided in a fiber must satisfy the total internal reflection requirements at the core-cladding interface according to Snell's law of refraction [9].

In practical optical fibers the refractive indices of the core and cladding are nearly equal with $n_1 \geq n_2$ and $\Delta << 1.0$. The condition $\Delta << 1.0$ is called the *weak guidance* condition, and the corresponding optical fibers are called *weakly guiding fibers*. The concept of weak guidance is better appreciated if one notes that for $\Delta = 0$ the infinite clad optical fiber reduces to a homogeneous medium with no guidance properties. For $\Delta << 1.0$ but $\Delta \neq 0$ the guidance of energy is considered weak. However, this does not imply loose confinement of power to the core; at very high frequencies the energy can be tightly bound to the core, even in a weakly guiding fiber. Furthermore, the condition $\Delta << 1.0$ is mandated in both single-mode and multimode fibers. In multimode fibers $\Delta << 1.0$ is required for low inter-modal dispersion since the delay time between the lowest order and highest order modes is proportional to Δ. In a single mode fiber $\Delta << 1.0$ is necessary in order to have manageable core sizes. In addition, the weak guidance condition leads to greatly simplified modal expressions which are quite valid for short lengths of fiber, as is the case with typical fiber sensors.

In a step-index, lossless and non-magnetic optical fiber that is translationally invariant along the axial direction, the guided mode solutions can be summarized in phasor form as follows:

$$\vec{e}(r,\phi) = A\, J_\ell(Ur/a) \begin{Bmatrix} \cos(\ell\phi) \\ \sin(\ell\phi) \end{Bmatrix} \begin{Bmatrix} \hat{a}_x \\ \hat{a}_y \end{Bmatrix} \qquad r<a \qquad (2.2.4)$$

$$\vec{h}(r,\phi) = -Y_1\left(\vec{e}(r,\phi) \times \hat{a}_z\right)$$

and

$$\vec{e}(r,\phi) = A\, K_\ell(Wr/a) \begin{Bmatrix} \cos(\ell\phi) \\ \sin(\ell\phi) \end{Bmatrix} \begin{Bmatrix} \hat{a}_x \\ \hat{a}_y \end{Bmatrix} \qquad r>a\,, \qquad (2.2.5)$$

$$\vec{h}(r,\phi) = -Y_2\left(\vec{e}(r,\phi) \times \hat{a}_z\right)$$

where there is an implied multiplicative factor of $e^{-j(\beta z-\psi)}$, which represents the phase of the mode and where $\ell = 0,1,2,\ldots$, with r, ϕ, and z being the cylindrical coordinates representative of the fiber geometry. Also, $J_\ell(x)$ is the Bessel function of the first kind, order ℓ, and $K_\ell(x)$ is the modified Bessel function of the second kind, order ℓ. $J_\ell(x)$ is plotted for orders 0,1 and 2 in Figure 3. The amplitude coefficient A is determined by the source input conditions and is assumed to absorb any signs (plus or minus) at present, while Y_1 and Y_2 are the characteristic admittances of the core and cladding, respectively. In addition, the parameters U and W are given by

$$U = K_0 a\sqrt{n_1^2 - \overline{\beta}^2} \tag{2.2.6}$$

$$W = K_0 a\sqrt{\overline{\beta}^2 - n_2^2}\ , \tag{2.2.7}$$

where "a" is the fiber core radius and $\overline{\beta} = \beta/k_0$, with β being the modal propagation constant [8].

Notice in equations (2.2.4) and (2.2.5) that the electric fields are either x or y directed. Since polarization is defined by the direction of the electric field, the modes described by equations (2.2.4) and (2.2.5) are linearly polarized and are thus called *linearly polarized* or *LP* modes. The bracketed quantities in equations (2.2.4) and (2.2.5) may be taken as multiplicative factors in any combination with the only stipulation being that the magnetic field vectors be orthogonally oriented with respect to the electric field vectors. Modes containing the $\cos(\ell\phi)$ multiplicative factor are called *even* modes while modes containing the $\sin(\ell\phi)$ multiplicative factor are called *odd* modes. For all cases except when $\ell = 0$ the modes have a degeneracy of four (i.e.: even, x-polarized; even, y-polarized; odd, x-polarized and odd, y-polarized). When $\ell = 0$ it is obvious that *LP* modes are independent of ϕ and therefore have a degeneracy of two (i.e., x-polarized and y-polarized) [8].

The propagation constants β for *LP* modes are found by solving the following characteristic equation, the solutions of which are plotted in Figure 4 [9,10]:

$$\frac{J_\ell(U)}{UJ_{\ell-1}(U)} + \frac{K_\ell(W)}{WK_{\ell-1}(W)} = 0\,, \quad \ell = 0,1,2,\ldots \quad . \tag{2.2.8}$$

Note that the solutions to this characteristic equation actually appear as functions of β vs. ω, where ω is related to the source wavelength λ_0 by $\omega\lambda_0 = 2\pi c$, with c being the speed of light in free space. The solutions are, however, plotted in Figure 4 in the normalized form of b versus V where b is the normalized propagation constant given by

$$b = \frac{(\beta/k_0)^2 - n_2^2}{n_1^2 - n_2^2} \quad . \tag{2.2.9}$$

The normalized frequency V is given in terms of the source wavelength and fiber parameters by

$$V = k_0 a\sqrt{{n_1}^2 - n_2^2} \;\; = \;\; k_0 a(NA) \;\simeq\; k_0 a n_1\sqrt{2\Delta} \quad . \tag{2.2.10}$$

Note also that there are multiple solutions to the characteristic equation for each value of ℓ. Therefore, specific *LP* modes are typically labeled $LP_{\ell m}$, where the propagation constant for the $LP_{\ell m}$ mode is the m^{th} solution for β, at a given frequency (or source wavelength), when the principal mode number ℓ takes a particular value. For example, the LP_{23} mode is the mode whose propagation

constant β is found from the third solution to the characteristic equation when $\ell = 2$ [8].

Guided mode cutoff occurs when $b = 0$ and as can be seen in Figure 4, a fiber is operated in a single-mode regime when $V \leq 2.405$. As V increases (by decreasing the source wavelength λ_0 or by increasing the core radius a) more and more modes are allowed to propagate in a fiber until the fiber enters the multimode operating regime. Strictly speaking a fiber is a multimode fiber if more than one mode is allowed to propagate. Practically, though, multimode fibers are taken as those fibers with extremely high V values, typically in excess of $V = 50$. To achieve these high V values the core radii are usually made very large in multimode fibers, thus making the fiber multimode for a wide range of source wavelengths. By comparison, single-mode fibers typically have very small core radii. For example, a fiber intended for single mode operation at a nominal source wavelength of 1300 nm will have a core radius of approximately 4.5 μm (see again Figure 1). Using these values in equation (2.2.10), with $n_1 = 1.458$, we can solve for Δ to find $\Delta \simeq 0.003$. It is therefore obvious that, as mentioned earlier, Δ must be much less than unity for single-mode fibers to have manageable core sizes.

Of interest in the study of modal domain sensing techniques are those fibers which allow the propagation of only a few modes. Such fibers will often be

called *few-mode fibers*, typically with $V < 5$, and are of interest since it is much simpler to study and characterize the interference of a few modes than it is the many modes in a true multimode optical fiber. Recall that modal domain sensors are essentially self-referenced interferometers which exploit modal interference as the basis for a sensor mechanism. Few-mode fibers are also attractive for use in modal domain sensors since, as in all fiber optic sensors, the sensor data will be collected by monitoring the modulated intensity distribution at the fiber/sensor output. These intensity distributions (or patterns) at the output of modal domain sensors are created due to the interference of the guided modes in the fiber and are modulated as a function of the environmental disturbances being detected. For modal domain sensors using few-mode fibers these output intensity patterns are often qualitatively simple and well behaved as a function of disturbance and therefore give rise to simple sensor systems.

One can cause a fiber to be few-moded by simply injecting into a single-mode fiber light of a shorter wavelength than that typically injected for single mode operation. For example, it will later be shown that a 4.5 μm core radius fiber, usually intended for single-mode operation at $\lambda_0 = 1300$ nm, will have $V = 4.616$ when the source wavelength is reduced to $\lambda_0 = 633$ nm, as with He-Ne gas laser injection. We can thus see from Figure 4 that only the LP_{01}, LP_{11}, LP_{21} and LP_{02} modes and their degeneracies will be allowed to

propagate. Such a fiber is easily seen to be few-moded. Plots of the intensity distributions of the LP_{01}, LP_{11}, LP_{21} and LP_{02} modes can be found in Figures 5-8, respectively. These and other similar plots to be addressed later were created using the numerical expansions for $J_0(x)$ and $J_1(x)$ given in Appendix C and the FORTRAN programs given in Appendix D. It should be mentioned that the x and y values of Figures 5-8 are given in microns and that these figures are valid only for $r = \sqrt{x^2 + y^2} \leq 4.5\,\mu m$, as these plots were created considering only the modal solutions in the core for the case of 633 nm light injection into a 4.5 μm radius fiber, as discussed above. The intensity beyond $r = 4.5\,\mu m$ decays approximately exponentially. Finally, it should also be mentioned that in Figures 5-8 no interference has been considered and that the amplitudes of the modal intensity distributions are quite arbitrary with only the general pattern shape being of any importance at present.

2.3 Photodetectors

Data is collected from a fiber optic sensor by monitoring the modulated intensity distribution at the sensor output. Typically this monitoring is achieved through the use of a photodetection circuit. Such a photodetection circuit is shown in Figure 9 with its equivalent circuit. It is seen that the

photodiode is modeled by a series bulk resistance R_s and a total capacitance C_d consisting of junction and packaging capacitances. A bias (or load) resistance is given by R_L and the amplifier following the photodiode has an input capacitance C_a and a shunt resistance R_a. In a practical circuit, however, R_s is much smaller than R_L and can be neglected. Also, C_d is usually small and only affects the high frequency response (rise time) of the photodetection circuit. Thus, for low frequency input signals, such as those created at the output of the modal domain sensors to be discussed later, the capacitance C_d is seen essentially as an open circuit. Furthermore, for the present discussion it will be assumed that the amplifier is used as a high impedence buffer with unity gain, as would be the case at the input to an oscilloscope, for instance. For low frequency or DC signals the photodetection circuit is therefore seen to reduce quite simply to a photodiode in parallel with a load resistance [9].

Optical power incident on the photodiode is converted into a photocurrent when the excess electron-hole pairs created by the incident light are swept out of the photodiode depletion region by the fields created by the high reverse bias voltage ($\sim$ 10 V for *pin* photodiodes). The photocurrent is related to the incident optical power P_0 by the relation

$$I_p = \mathcal{R} P_0 \quad , \tag{2.3.1}$$

where $\mathscr{R}$ is called the *responsivity* of the photodiode and has the units of amps per watt. $\mathscr{R}$ is given in turn by the expression

$$\mathscr{R} = \frac{\eta q}{h\nu} \quad , \tag{2.3.2}$$

where $h\nu$ is the energy of the incident photon, q is the electronic charge and η is the photodiode quantum efficiency which relates the number of electron-hole pairs created to the number of incident photons. For silicon photodiodes a nominal value of responsivity is $\mathscr{R} = 0.5$ A/W for common detection wavelengths [9]. The photocurrent thus created causes a voltage across the load resistor given by

$$V_0 = \mathscr{R} P_0 R_L \ . \tag{2.3.3}$$

This is the quantity typically recorded when using simple photodetection circuits and the measured quantity V_0 is easily converted to a measure of incident optical power if the load resistance R_L and the responsivity $\mathscr{R}$ at the detection wavelength are known. If we now consider that the incident optical power P_0 consists of an average or quadrature point component P_Q and a signal component ΔP such that $P_0 = P_Q + \Delta P$ we see that the electrical signal power created by the signal component of the incident optical power is given by

$$P_{ES} = (\mathscr{R}\,\Delta P)^2\, R_L \quad . \tag{2.3.4}$$

The principal noises associated with photodetectors are quantum or shot noise, dark-current noise generated in the bulk material of the photodiode, and the surface leakage current noise. For small and well packaged photodiodes, however, the surface leakage current noise is small and can be neglected. The shot noise arises from the statistical nature of the production and collection of photoelectrons when an optical signal is incident on a photodetector and sets a fundamental lower limit on receiver sensitivity when all other conditions are optimum. The RMS shot noise power is given as

$$P_{SN} = 2q\mathrm{I}_Q B R_L \quad , \tag{2.3.5}$$

where B is the detection bandwidth and I_Q is the average photocurrent given as $\mathrm{I}_Q = \mathscr{R}P_Q$ where P_Q can be measured with no signal applied.

The photodiode dark current is the current that continues to flow when no light is incident on the photodiode. This is in general a combination of bulk and surface currents. However, the bulk dark current is usually dominant and arises from the electron-hole pairs which are thermally generated in the *pn* junction of the photodiode. The RMS bulk dark current noise is given as

$$P_{DB} = 2q\mathrm{I}_D B R_L \tag{2.3.6}$$

where I_D is the primary detector bulk dark current and can be found for specific photodiodes in various vendor catalogs [9].

In addition to the detector noise factors just discussed the photodetector load resistor contributes an RMS thermal (Johnson) noise power given as

$$P_T = 4k_BTB \quad , \tag{2.3.7}$$

where k_B is Boltzman's constant and T is the absolute temperature. This noise can be reduced by cooling the detection circuit [9].

The power signal-to-noise ratio S/N at the output of an optical receiver is now easily seen to be

$$S/N = \frac{P_{ES}}{P_{SN} + P_{DB} + P_T} \quad , \tag{2.3.8}$$

or

$$S/N = \frac{(\mathscr{R}\Delta P)^2}{2qB(\mathscr{R}P_Q + I_D) + \dfrac{4k_BTB}{R_L}} \quad . \tag{2.3.9}$$

Of special interest is the case when S/N goes to unity. At this point the signal power just equals the noise power and enables one to determine the minimum

detectable optical signal ΔP_{min}. When only photodetector and load resistor noise factors are accounted for, we find that

$$\Delta P_{min} = \frac{1}{\mathscr{R}}\left(4qB(\mathscr{R}P_Q + I_D) + \frac{8k_BTB}{R_L}\right)^{1/2} \qquad (2.3.10)$$

and in the shot noise limited case we find that

$$\Delta P_{min(SN)} = \frac{1}{\mathscr{R}}(4qB(\mathscr{R}P_Q + I_D))^{1/2} \quad , \qquad (2.3.11)$$

where a factor of 2 has been included in the noise power terms of equations (2.3.10) and (2.3.11) due to the fact that at the operating point the incident optical power is uncertain to within ±(shot noise and/or thermal noise).

Note that this analysis has been for *pin* photodiodes only and that the shot noise limit of detection is practically unrealizable. In addition, if one must operate a photodetection circuit at elevated temperatures or if it is impractical to use a large load resistor, which would reduce the thermal noise component of equation (2.3.10), one may have to resort to the use of an avalanche photodiode (or APD). An APD will also give a sharper system rise time for detection of high frequency signals but should not be used unless thermal noise is excessive. This is due to the generation of excess shot noise during the avalanche process in APD's. At reasonable temperatures and for reasonable values of R_L the signal-to-noise ratio will be reduced by using an

APD. Finally, it should be mentioned that it has been assumed in the previous discussions that noise factors arising from sources other than the photodiode or its load resistor are negligible. This is reasonable only in a laboratory or other situation where environmental factors can be controlled. We now turn our attention to a discussion of the photoelastic effect in optical fibers under strain.

2.4 The Photoelastic Effect

Recall that the phase of a mode is given by $\phi = \beta z - \psi$ where ψ is a random phase term. Since the modal domain sensors to be discussed in the next chapter will derive their output from a differential modal phase modulation (i.e., modal interference) as a function of strain, it is important to discuss how the phase of a mode changes as a function of fiber strain.

As a fiber is strained three principal factors act to change the modal phase. First, the fiber length changes. Second, the index of refraction changes due to the photoelastic effect and finally, the fiber diameter reduces. The change in phase due to these effects is thus

$$\Delta\phi = \frac{\partial\phi}{\partial z}\Delta z + \frac{\partial\phi}{\partial n_1}\Delta n_1 + \frac{\partial\phi}{\partial D}\Delta D$$

$$\Delta\phi \simeq \beta\Delta z + z\frac{\beta}{n_1}\Delta n_1 \quad , \tag{2.4.1}$$

where the effect of the change in fiber diameter is considered negligible and where $\partial\beta/\partial n_1 = \beta/n_1$ [1]. Also from [1], for low order modes, we have

$$\Delta n_1 = \left\{ -\frac{1}{2} n_1^3[\varepsilon_z(1-\nu)p_{12} - \nu\varepsilon_z p_{11}] \right\} \quad , \tag{2.4.2}$$

where ε_z is the axial strain, ν is Poisson's ratio, n_1 is the index of the core and p_{11} and p_{12} are the photoelastic constants. Reasonable values of these unitless constants are given for silica as follows [4]:

$$\begin{aligned} \nu &= 0.17 \\ p_{11} &= 0.12 \\ p_{12} &= 0.27 \\ n_1 &= 1.458 \end{aligned}$$

By substituting equation (2.4.2) into equation (2.4.1) and rearranging terms we find that

$$\Delta\phi = \beta\Delta z\left\{1 - \frac{1}{2} n_1^2[(1-\nu)p_{12} - \nu p_{11}]\right\}$$

$$\Delta\phi = \beta\, \Delta z\, \{\alpha\}\,, \tag{2.4.3}$$

where the relation $z \times \varepsilon_z = \Delta z$ has been used. Using the constants given above we see that $\alpha = 0.78$. Although this is a reasonable value of α, the true value may change from fiber to fiber. Experimentally determined values have been found as large as $\alpha = 0.92$, as will be seen later. In any case, though, it is clear that due to the photoelastic effect a fiber under strain will see a significant reduction of the core index of refraction and therefore a significant reduction in the effective optical pathlength of the modes in the fiber. This results in a change in modal phase in a fiber under strain which is less than that expected if the fiber simply undergoes pure elongation.

When a fiber supports more than one mode it is also important to investigate how the differential phase of the modes is influenced by strain. Consider two modes with phases $\phi_1 = \beta_1 z - \psi_1$ and $\phi_2 = \beta_2 z - \psi_2$, respectively. The differential phase is given as

$$\phi_{12} = (\beta_1 - \beta_2)z - (\psi_1 - \psi_2) = \Delta\beta z - \Delta\psi \quad . \tag{2.4.4}$$

We may now consider that $\phi_{12} = \phi_0 + \Delta\phi_{12}$, where ϕ_0 is the initial differential phase of the modes in a no strain situation and where $\Delta\phi_{12}$ is the differential phase change induced as the fiber is strained. In an exactly analogous manner that was used to prove the result of equation (2.4.3) we can show that

$$\Delta\phi_{12} = \Delta\beta\, \Delta z\, \{\alpha\} \quad , \tag{2.4.5}$$

so that

$$\phi_{12} = \Delta\beta\varepsilon_z L_f(\alpha) + \phi_0 \quad , \tag{2.4.6}$$

where $\varepsilon_z L_f = \Delta z$ and L_f is the gage length of, say, a fiber optic sensor. Note also that $\phi_0 = -\Delta\psi$. As will be evident in the next chapter the relationship given in equation (2.4.6) is extremely important in the study of fiber optic strain sensors.

One last comment should be made before concluding this discussion. That is, note that in the previous analyses it has been assumed that the amplitudes of the modes in a fiber under strain remain constant and that only the modal phase is influenced as strain is varied. This is not exactly the case since the amplitude of a mode is a function of $U = k_0 a\sqrt{n_1^2 - \overline{\beta}^2}$, in the core region, and both n_1 and $\overline{\beta}$ are functions of strain. However, only very large amounts of strain vary n_1 or $\overline{\beta}$ appreciably so that U will essentially remain constant with strain. For instance,

$$n_1 = n_1(\varepsilon_z) \simeq 1.458 + \Delta n(\varepsilon_z) = 1.458 - (0.32)\varepsilon_z \tag{2.4.7}$$

using the previous calculation for Δn in equation (2.4.2). It is thus seen that for strains even on the order of one percent (which is near the breaking point of

most fibers) n_1 remains nearly constant. A similar result can be obtained for $\overline{\beta}$ as a function of strain, making the assumption of constant field amplitudes quite valid.

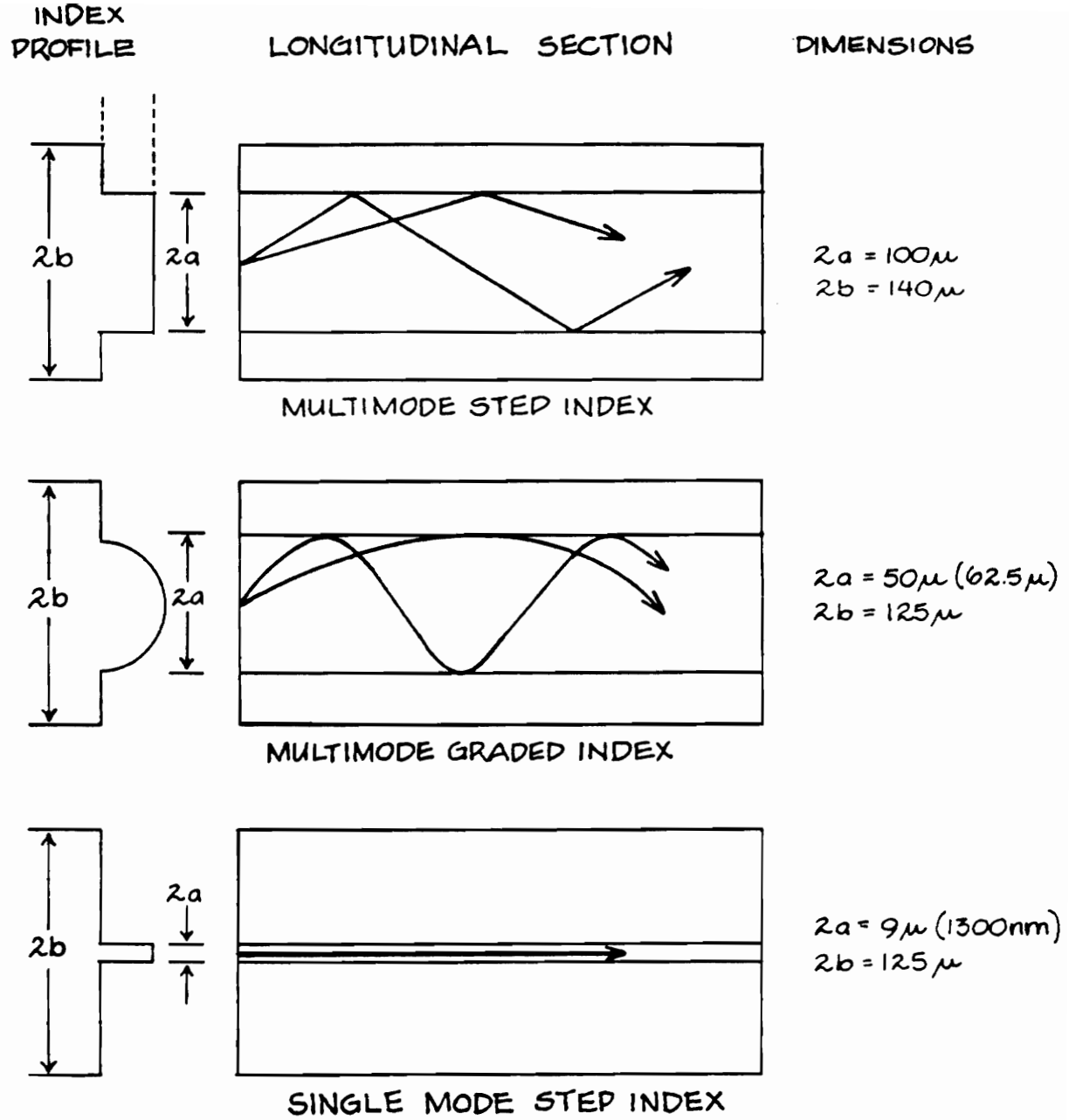

Figure 1. Optical fiber geometry summary

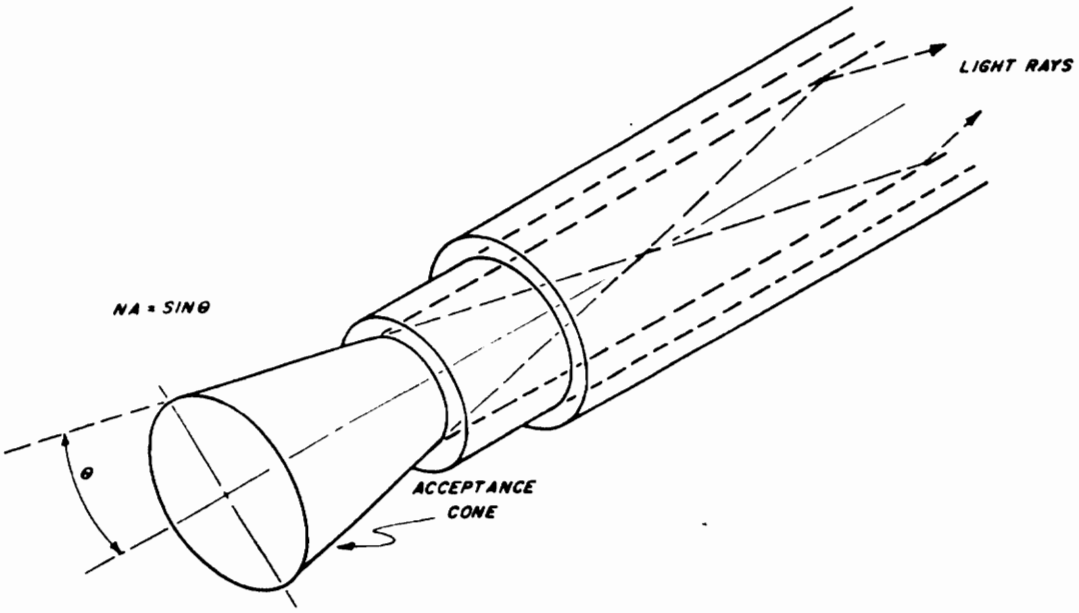

Figure 2. Numerical aperture (NA) of an optical fiber [16]

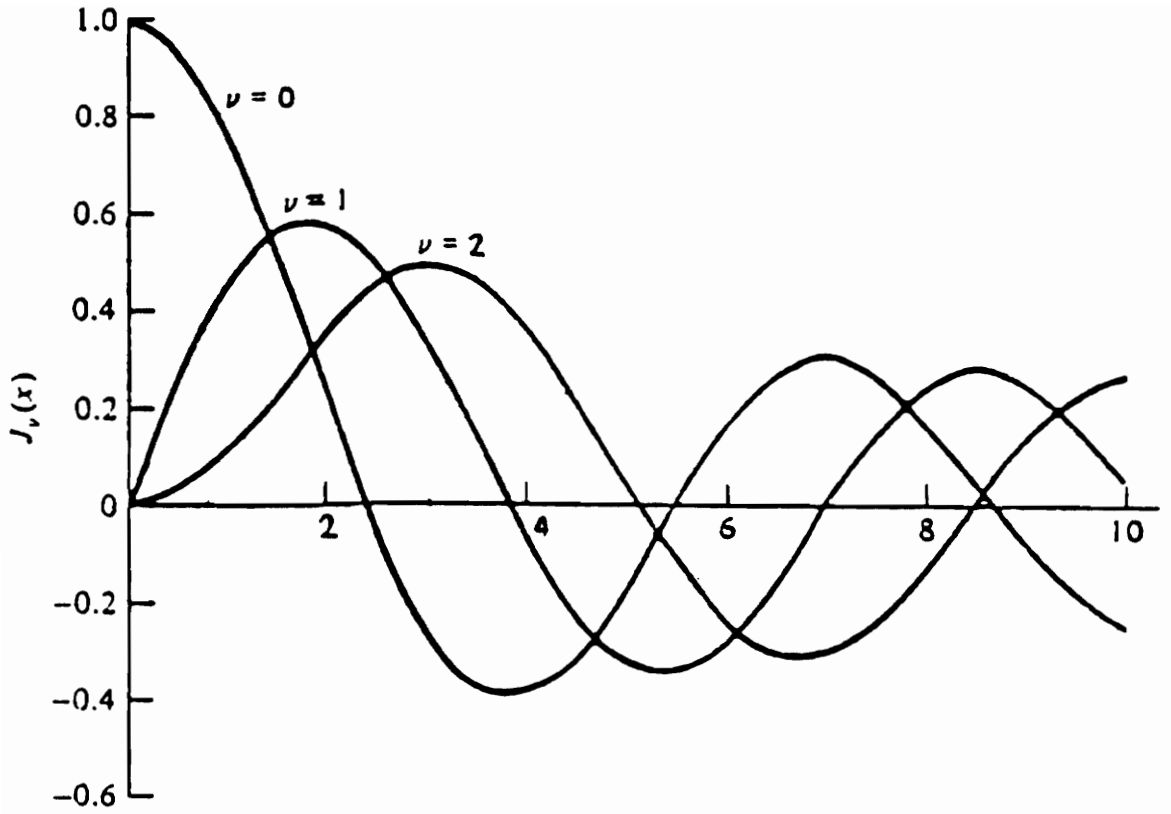

Figure 3. Bessel's function of the first kind for the first three orders [9]

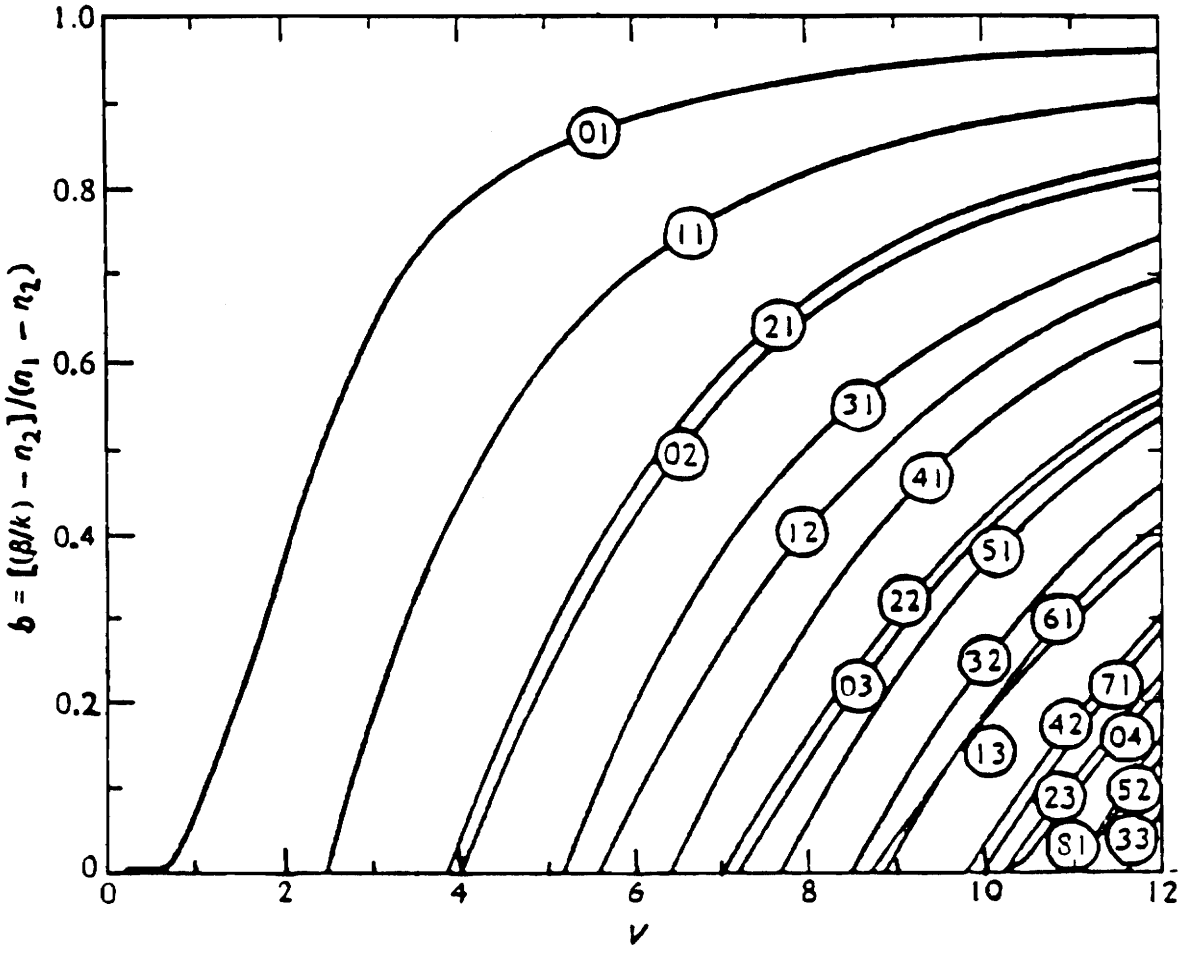

Figure 4. The normalized b versus V curves [9]

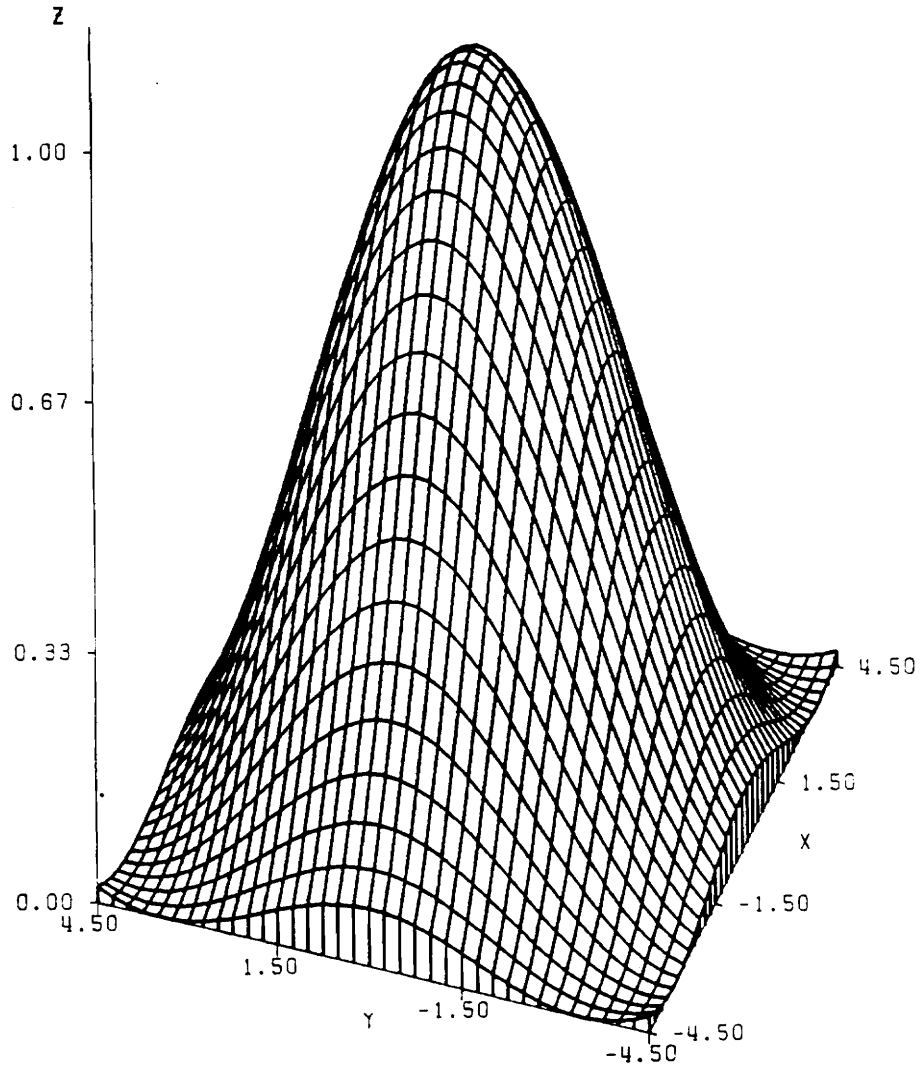

Figure 5. Intensity distribution of the LP_{01} mode

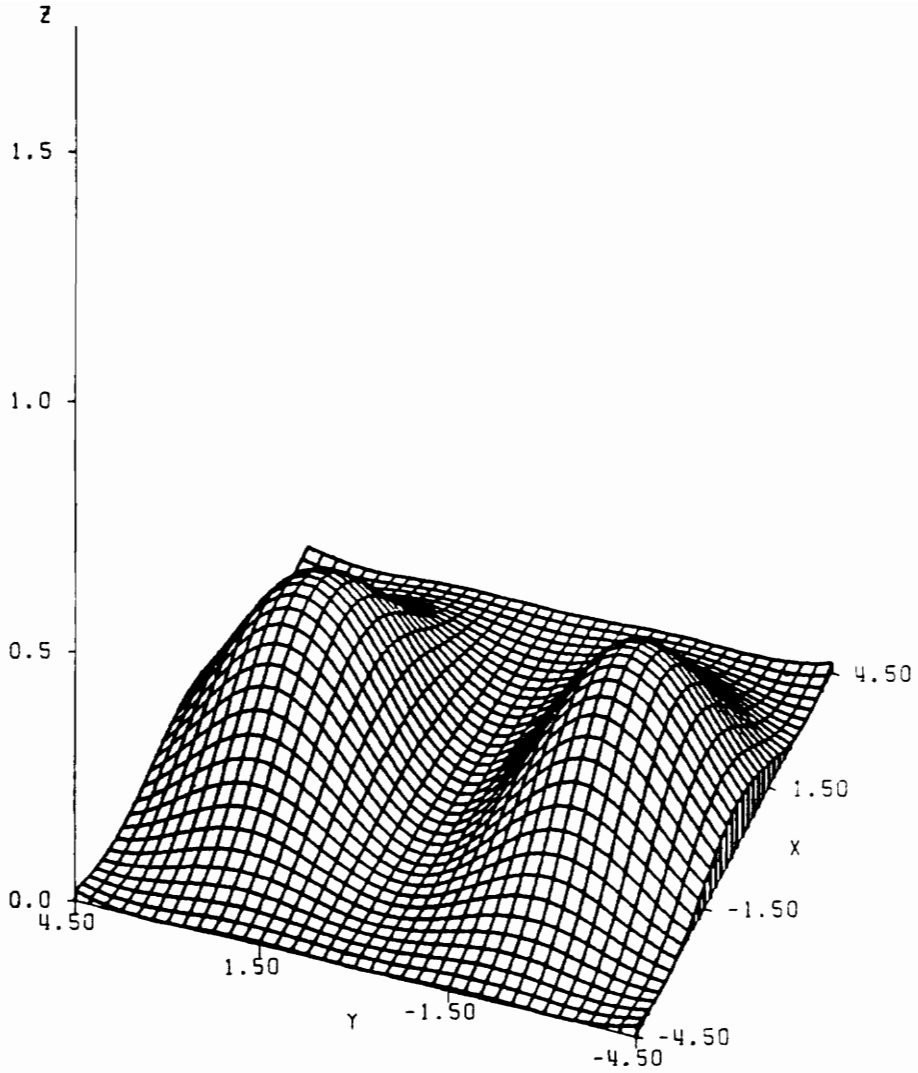

Figure 6. Intensity distribution of the LP_{11} mode

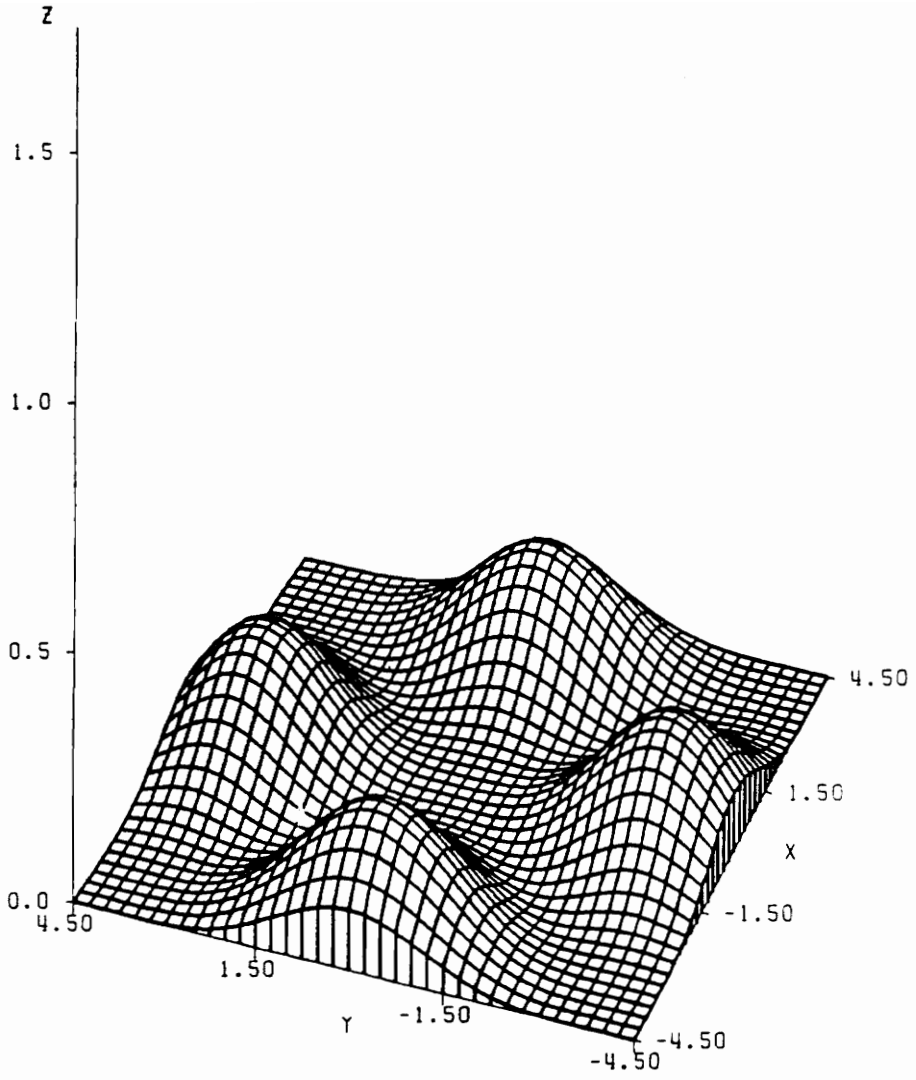

Figure 7. Intensity distribution of the LP_{21} mode

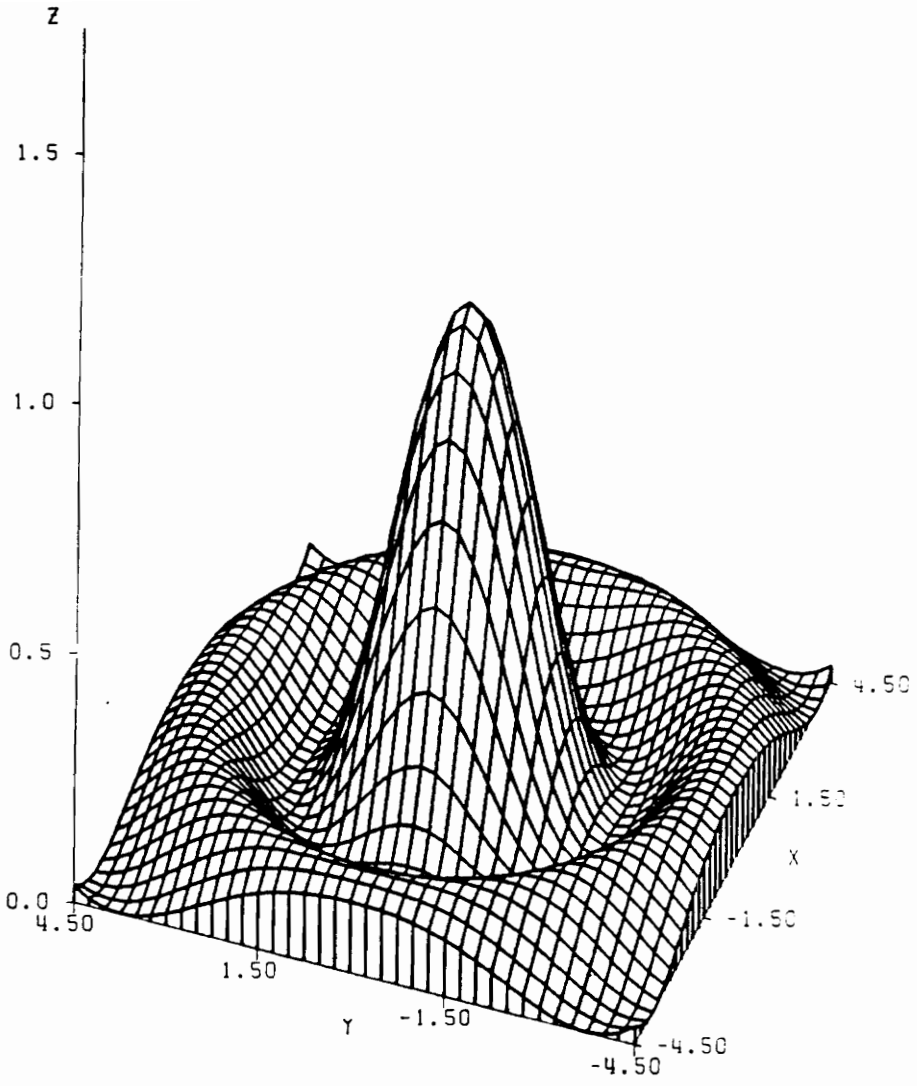

Figure 8. Intensity distribution of the LP_{02} mode

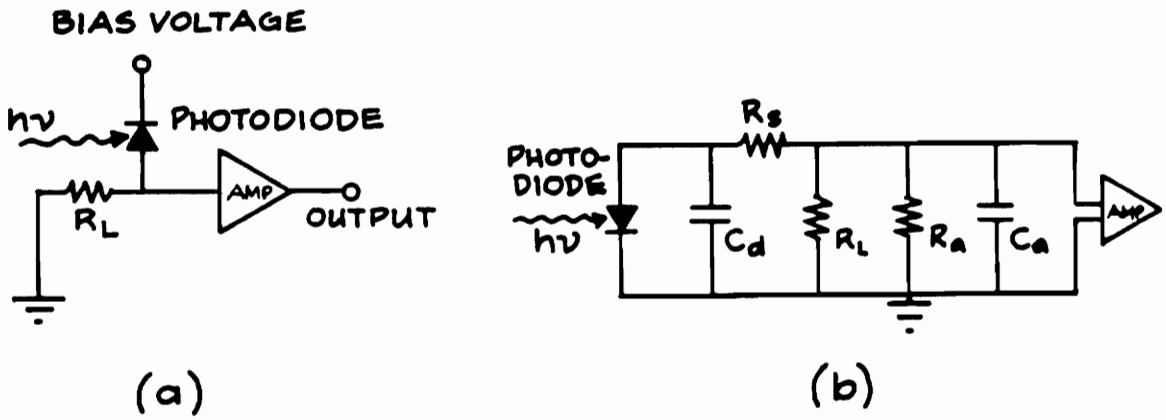

Figure 9. A simple photodetector and its equivalent circuit [9]

3.0 MODAL DOMAIN SENSING

Modal domain sensing is a fiber optic sensing technique based on the differential phase modulation occuring as a function of disturbance between the interfering guided modes of an optical fiber. As we know, specific mode groups will propagate in a fiber and interfere to cause characteristic intensity distributions, or patterns, at the fiber output, as is shown in a very simple fashion in Figure 10. When the fiber is subjected to a disturbance, these intensity patterns are modulated as a direct function of the external disturbance and by monitoring this pattern modulation, often by using simple spatial filters, one can obtain information about the disturbance.

Strictly speaking, any sensor based on the interference of modes in an optical fiber can be called a "modal domain sensor." However, of special interest are those sensors based on modal interference in few-mode optical fibers with

$V < 5.0$. Such sensors are qualitatively simple in that since only a few modes are allowed to propagate it is possible to obtain simple, closed form solutions for the modulated output patterns which may manifest themselves. This is obviously an advantage when one wishes to design *a predictable* sensor. As a result, only modal domain sensors utilizing few-mode fibers will be discussed in the remainder of this chapter.

Specifically, this chapter will be dedicated to describing the electromagnetic basis of the observed intensity pattern modulation, as a function of axial strain, of modal domain sensors using 9μm core diameter fiber at source wavelengths of 633 nm and 850 nm. For simplicity we will use the notation MDS/9-633 and MDS/9-850 to describe these modal domain sensors at the source wavelengths of 633 nm and 850 nm, respectively. Also, note that although only axial strain considerations will be described here, modal domain sensors are not limited to measuring only axial strain. Axial strain is simply one of the most fundamental disturbances to which a fiber can be subjected and a detailed analysis of how axial strain affects an optical fiber sensor will provide the basis for designing sensors to measure other disturbances. For instance, if a sensing length of fiber is embedded in a material with known thermal expansion characteristics, a thermal sensor based on modal interference could be designed since the thermal expansion of the material can be related to induced axial strain in the embedded fiber

sensor. Sensors designed to detect many other environmental influences are also possible. We now proceed to a detailed discussion of the MDS/9-633 sensor.

3.1 The MDS/9-633 Sensor

It has been observed that when 633 nm light from a He-Ne gas laser is injected into a 9 μm core diameter fiber a symmetric three lobe pattern can be created at the output which exhibits pure rotation when the fiber is subjected to axial strain. Using a Photon Kinetics FOA-2000 fiber optic analyzer, the second mode cutoff for the above mentioned fiber, which is designed for single-mode operation at 1300 nm, has been determined to be 1215 nm (i.e., V = 2.405 at λ_o = 1215 nm). Also, this fiber has a measured numerical aperture of NA = 0.1 (refer to Figure 11 for plots of the data generated by the FOA-2000 unit). At a source wavelength of 633 nm this fiber is easily seen to have a normalized frequency of

$$V = 2.405 \frac{1215\,nm}{633\,nm} = 4.616 \quad .$$

This allows the propagation of the LP_{01}, LP_{11}, LP_{21} and LP_{02} modes and their degeneracies, as discussed in section 2.2. However, as the three lobe pattern

under discussion exhibits a central null, it is evident from Figures 5 and 8 that the LP_{01} and LP_{02} must not be excited in the fiber for the three lobe pattern to be created. If we further require that our source emits polarized light, say x-polarized, we are left with only four modes which may interfere to cause the rotating three lobe pattern of interest. Specifically, these modes are the x-polarized odd LP_{11}, even LP_{11}, odd LP_{21} and even LP_{21} modes and it can be shown that with a proper choice of amplitude coefficients, determined in reality by the launch conditions of the fiber, that these modes do interfere to cause the observed three lobe pattern and its well defined rotational behavior [11]. From equation (2.2.4) we see that the electric fields in the core of the above mentioned modes are given as

$$\begin{aligned}
\vec{E}^{e}_{11} &= A^{e}_{1}\, J_1(U_{11}r/a)\, cos\phi\; e^{-j(\beta_{11}z - \psi^{e}_{11})}\, \hat{a}_x \\
\vec{E}^{o}_{11} &= A^{o}_{1}\, J_1(U_{11}r/a)\, sin\phi\; e^{-j(\beta_{11}z - \psi^{o}_{11})}\, \hat{a}_x \\
\vec{E}^{e}_{21} &= A^{e}_{2}\, J_2(U_{21}r/a)\, cos2\phi\; e^{-j(\beta_{21}z - \psi^{e}_{21})}\, \hat{a}_x \\
\vec{E}^{o}_{21} &= A^{o}_{2}\, J_2(U_{21}r/a)\, sin2\phi\; e^{-j(\beta_{21}z - \psi^{o}_{21})}\, \hat{a}_x
\end{aligned} \qquad (3.1.1)$$

Since the sensor behavior can be completely described by investigating only the interference of the mode solutions in the core, no further consideration will be given to the modal solutions for $r \geq a$.

The intensity pattern present at the fiber output is found from

$$I = \frac{1}{2} Re\left\{ (E_x \hat{a}_x \times Y_1 E_x \hat{a}_y) \cdot \hat{a}_z \right\} = \frac{1}{2} Y_1 |\vec{E}_x|^2 \ , \qquad (3.1.2)$$

where

$$E_x = (E_{11}^e + E_{11}^o) + (E_{21}^e + E_{21}^o) \qquad (3.1.3)$$

and Y_1 is the characteristic admittance of the core region.

We now assume that the amplitude coefficients are real and that $A_1^e = A_1^o = A_1$ and $A_2^e = A_2^o = A_2$ with the further assumption that the odd terms of equation (3.1.1) are 90° out of phase with relation to their respective even terms, so that

$$\psi_{11}^o = \psi_{11}^e + 90° = \psi_{11} + 90°$$

and

$$\psi_{21}^o = \psi_{21}^e - 90° = \psi_{21} - 90° \ .$$

Adding the even and odd terms of the LP_{11} mode, it is easy to see that

$$(E_{11}^e + E_{11}^o) = A_1 J_1\left(\frac{U_{11} r}{a} \right) (\cos\phi + j\sin\phi)\, e^{-j(\beta_{11} z - \psi_{11})}$$

or

$$(E_{11}^{e} + E_{11}^{o}) = A_1 J_1\left(\frac{U_{11} r}{a}\right) e^{-j(\beta_{11} z - \psi_{11} - \phi)} \quad . \tag{3.1.4}$$

Similarly, adding the even and odd terms of the LP_{21} mode it is seen that

$$(E_{21}^{e} + E_{21}^{o}) = A_2 J_2\left(\frac{U_{21} r}{a}\right) e^{-j(\beta_{21} - \psi_{21} + 2\phi)} \tag{3.1.5}$$

With these last two results in mind we now find the output intensity distribution using equations (3.1.2) and (3.1.3). The result is

$$\begin{aligned} I = I_0 \Bigg(& A_1^2 J_1^2\left(\frac{U_{11} r}{a}\right) + A_2^2 J_2^2\left(\frac{U_{21} r}{a}\right) \\ & + 2A_1 A_2 J_1\left(\frac{U_{11} r}{a}\right) J_2\left(\frac{U_{21} r}{a}\right) \cos(\Delta\beta z - \Delta\psi - 3\phi) \Bigg), \end{aligned} \tag{3.1.6}$$

where $\Delta\beta = \beta_{11} - \beta_{21}$, $\Delta\psi = \psi_{11} - \psi_{21}$ and $I_o = Y_1/2$.

It should be evident that the intensity distribution of equation (3.1.6) results in a pattern consisting of three equal lobes displaced azimuthally by 120°. It should also be evident that this pattern rotates as the modes propagate through the fiber. The first two terms of equation (3.1.6) are simply background intensity terms and are constant. The sum of these two terms is plotted in Figure 12, where it is assumed that $A_1 = A_2 = 1.0$ and where the x and y values are given in microns. The third term of equation (3.1.6) is the

term which gives rise to the pattern shape and rotational behavior as the modes advance in the z-direction and is plotted in Figure 13. The entire intensity distribution of equation (3.1.6) is plotted in Figure 14. As with Figure 12, Figures 13 and 14 are plotted assuming $A_1 = A_2 = 1.0$, with the x and y values being given in microns. The choice of A_1 and A_2 was made after evaluating several plots of equation (3.1.6), with the amplitude coefficients taken as parameters. For $A_1 \simeq A_2$ it was seen that there were approximate radial intensity nulls in the calculated intensity distrubution, displaced by 120°, which agree very closely with experimental observations. In addition, the plots in Figures 12-14 are valid only for the core region of the fiber (i.e., the plots are valid only for $r = \sqrt{x^2 + y^2} \leq 4.5\,\mu m$) and were plotted using the Bessel function mumerical expansions given in Appendix C and the FORTRAN programs of.Appendix D. Notice also that for $A_1 = A_2$, the amplitudes of the plots of Figures 13 and 14 are approximately equal in the radial region where the plotted functions are maximum, indicating that for this region in equation (3.1.6)

$$J_1^2\left(\frac{U_{11}r}{a}\right) + J_2^2\left(\frac{U_{21}r}{a}\right) \cong 2\,J_1\left(\frac{U_{11}r}{a}\right) J_2\left(\frac{U_{21}r}{a}\right) \quad . \qquad (3.1.7)$$

Using this result we can simplify equation (3.1.6) at the radial position where the function goes through a maximum to find

$$I = I'_0[1 + \cos(\Delta\beta z - \Delta\psi - 3\phi)]$$

$$I = I_p \cos^2\left(\frac{\Delta\beta z - \Delta\psi - 3\phi}{2}\right) , \qquad (3.1.8)$$

where I'_0 has incorporated into it the terms of equation (3.1.7) after they are factored from equation (3.1.6). In addition, to obtain the result of equation (3.1.8), the trigonometric identity $1 + \cos(2x) = 2\cos^2(x)$ has been used, with the peak lobe intensity I_p taken as $I_p = 2I'_0$. Now let us discuss how this rotating three lobe pattern can be used to detect axial strain.

If we observe the three lobe pattern as it emerges from the end face of the fiber, we will see an intensity distribution similar to that shown in Figure 15(a). If we then increase the optical pathlength of the fiber by inducing an axial strain, we will observe a pattern rotation. Due to the cosine squared nature of this pattern along the circular path which contains the lobe peaks, as given in equation (3.1.8) and as shown in Figures 15(a) and 15(b), it is seen that the most sensitive and linear position for monitoring the pattern rotation for the detection of axial strain is along this path at a position where the intensity is half that of the intensity of a lobe peak, as shown in Figure 15(b). In other words, if in a no strain situation we choose a fixed quadrature point in space to monitor on the three lobe pattern that both has an intensity of exactly half that of the peak intensity and is located on the circular path that contains the

lobe peaks, then for small increases in strain the intensity at this point will increase or decrease, as the patterns rotates, in direct proportion to the increase in strain.

If we define the azimuthal coordinate ϕ to take on the value $\phi=0$ at our quadrature point, then equation (3.1.8) becomes

$$I = I_p \cos^2\left(\frac{\Delta\beta z - \Delta\psi}{2} \right) \quad . \tag{3.1.9}$$

By now noticing that the $\Delta\beta z - \Delta\psi$ term in equation (3.1.9) represents an ensemble differential phase of the modes contributing to the rotating three lobe pattern, we can use arguments analogous to those used to prove the result of equation (2.4.6) so that the photoelastic effects may be included in equation (3.1.9), as the fiber is strained, to give

$$I = I_p \cos^2\left(\frac{\Delta\beta\, \varepsilon_z L_f \alpha + \phi_o}{2} \right) \quad , \tag{3.1.10}$$

where ε_z is the axial strain, L_f is the gage length of the fiber sensor, α is a constant less than unity that arises due to photoelastic effects and ϕ_o is the ensemble differential phase of the modes in a no strain situation. If we now choose the quadrature point, or Q-point, such that the intensity at this point

increases with strain from an unstrained value of $I = I_p/2$, we must require that $\phi_o = -\pi/2$ so that at the Q-point

$$I = I_p \cos^2\left(\frac{\Delta\beta\, \varepsilon_z\, L_f\, \alpha}{2} - \frac{\pi}{4} \right) \quad . \tag{3.1.11}$$

In practice, however, once the quadrature point has been set it will often be of more use to measure the change in intensity from the Q-point as a function of strain. This is found simply to be

$$\Delta I(\Delta\varepsilon_z) = \frac{\partial I}{\partial \varepsilon_z} \Delta\varepsilon_z = I_Q(\Delta\beta\, L_f\, \alpha)\Delta\varepsilon_z \quad , \tag{3.1.12}$$

where $I_Q = I_p/2$. Note that this result was obtained from an assumed no strain initial condition; however, it is still valid if the quadrature point is set with the fiber initially under strain. This is useful in a practical situation so that $\pm\,\Delta\varepsilon_z$ can be detected. Also note that this result is valid only for small changes in axial strain and that for small $|\Delta\varepsilon_z|$, the function $\Delta I(\Delta\varepsilon_z)$ is linear.

Some other observations should be made at this point. First of all, since the response $\Delta I(\Delta\varepsilon_z)$ is linear, we can use the same sensor arrangement to measure static strain or small amplitude sinusoidal strain, where

$$\Delta I(\Delta\varepsilon_{peak}, t) = I_Q\, (\Delta\beta\, L_f\, \alpha)\, \Delta\varepsilon_{peak}\, \cos(\omega t) \quad , \tag{3.1.13}$$

if $\Delta\varepsilon_{peak}$ is the amplitude of the sinusoidal axial strain. This result will also hold for small amplitude vibrational strain such as would be caused if a fiber was bonded to a vibrating structure. "Small amplitude vibrational strain" is meant to indicate that the peak deflection of the vibrating structure is such that the fiber is tensioned without being appreciably bent. Second, since for small amplitude sinusoidal perturbations in the fiber the resulting change in intensity is also sinusoidal at the same frequency, the sensor has obvious uses as a vibration sensor. And finally, it should be noted that in an actual sensor arrangement, a detection circuit will be used to convert intensity to voltage. If a small spatially filtering pinhole is placed between the fiber end face and the photodetector to monitor the intensity pattern at the Q-point this voltage will be directly related to the area of the spatial filter, the responsivity of the photodetector and the load resistance of the detection circuit such that

$$\Delta V(\Delta\varepsilon_z) = V_Q\,(\Delta\beta\, L_f\, \alpha)\, \Delta\bar{\varepsilon}_z$$

or

$$\Delta\bar{\varepsilon}_f = \frac{\Delta V}{V_Q\,(\Delta\beta\, L_f\, \alpha)} \quad , \tag{3.1.14}$$

for the case of static strain in the fiber and

$$\Delta V(\Delta\varepsilon_{peak},t) = V_Q\,(\Delta\beta\, L_f\, \alpha)\, \Delta\bar{\varepsilon}_{peak}\, \cos(\omega t)$$

or

$$\Delta\bar{\varepsilon}_f(t) = \frac{\Delta V_{peak}\cos(\omega t)}{V_Q\,(\Delta\beta\, L_f\,\alpha)} \quad , \tag{3.1.15}$$

for the case of small amplitude time harmonic strain and small peak displacement vibrational strain. Note that in equations (3.1.14) and (3.1.15) the notation $\Delta\bar{\varepsilon}_f$ has been used to indicate the average measured axial strain in the fiber. This has been done since strain is a localized quantity and fiber optic strain sensors are only able to detect strain as averaged along their gage length. See Appendix A for further details of strain averaging. In addition, the results of equations (3.1.14) and (3.1.15) will likely be of most use in an actual system with V_Q measured at quadrature and ΔV_{peak} and ω measured, say, using a spectrum analyzer.

Before discussing sensitivity let us discuss some of the practical aspects of the MDS/9-633 sensor. First, it should be noted that the interest in studying the rotating three lobe pattern of the MDS/9-633 sensor arose due to its ability to be created using simple optical components. Also, once created, this pattern is easy to work with due to its well defined rotational behavior and due to the fact that 633 nm light is visible and requires no special viewing equipment. Creating the rotating three lobe pattern, however, is not at all an easy task. Indeed, it often seems that obtaining this pattern requires a fair amount of luck.

Once created, though, the modal content of the pattern is unique and can be studied, as has been done in the past few pages, leading to the simple strain measurement results of equations (3.1.14) and (3.1.15). These equations state very simply how small changes in strain can be measured in the optical fiber of a MDS/9-633 sensor once the quadrature point has been properly set.

Setting the Q-point of the MDS/9-633 sensor, however, is another difficult task to accomplish. Typically, in order to position a small spatial filter at the proper quadrature point, one must apply a small signal sinusoidal disturbance to the sensor via a piezoelectric device and use linear positioners to move the spatial filter until one locates the position of the pattern that gives the largest amplitude and least distorted sinusoidal signal at the output of the photodetection circuit, as displayed on, say, an oscilloscope. Note that the spatial filter *must* be placed between the output end of the fiber sensor and the photodetector and *must* be small so that any intensity variation, which is a point function, can be accurately simulated and monitored. One may also set the quadrature point by aligning the spatial filter at the peak of a lobe and by then causing a static strain in the fiber, via some static strain control device, so that the pattern rotates until the quadrature point is properly aligned with the spatial filter. The use of both of these techniques for setting the Q-point will be discussed in chapter 4.

It should be obvious now that the MDS/9-633 sensor has practical limitations. In addition, due to the expected ease of use of the MDS/9-850 sensor to be discussed in the next section, no analysis has been given for the injection conditions necessary for the rotating three lobe pattern to exist in a MDS/9-633 sensor. Therefore, from this point on it will be assumed that if one wishes to use a MDS/9-633 sensor that a rotating three lobe pattern can be obtained and that there is available equipment which allows the quadrature point to be set. The results of equations (3.1.14) and (3.1.15) can then be used. With this in mind the sensitivity of the MDS/9-633 sensor can now be addressed.

Although in a typical measurement situation one would measure $\Delta\bar{\varepsilon}_f$ as a function of the change in voltage at the output of a photodetection circuit with respect to its Q-point value, we may still relate $\Delta\bar{\varepsilon}_f$ to the change in optical power through the spatial filter with respect to *its* Q-point value. This is done simply by dividing the numerator and denominator of equation (3.1.14), say, by $\mathscr{R}R_L$, where $\mathscr{R}$ is the responsivity of the photodiode and R_L is the load resistance of the detection circuit. This yields

$$\Delta\bar{\varepsilon}_f = \frac{\Delta P}{P_Q \Delta\beta L_f \alpha} \quad . \tag{3.1.16}$$

By refering to Figure 4 we can see that $b_{11} = 0.55$ and $b_{21} = 0.22$. Using equations (2.2.9) and (2.2.10) and Figure 4 we can therefore find that $\Delta\beta$ for the

MDS/9-633 sensor is $\Delta\beta = 1.2x10^4\, m^{-1}$ when $V = 4.616$, $n_1 = 1.458$, $a = 4.5\ \mu m$ and $\lambda_o = 633\ nm$. In addition we will reasonably assume for our detection circuit that for *pin* diode detection the fiber gage length L_f is $0.5\ m$, the bulk dark current I_d of the photodiode is approximately 1 nA, the detection bandwidth B is 1 Hz, the responsivity $\mathcal{R}$ of the photodiode is approximately 0.5 A/W at 633 nm, the operating temperature T is 300°K and the load resistance is $R_L = 10\ k\Omega$. We further assume that the optical power through the spatial filter at quadrature is $P_Q = 1\ \mu W$. Using these values we may calculate the minimum detectable change in optical power through the spatial filter using equation (2.3.10). We thus find

$$\Delta P_{min} = 3.8x10^{-12}\, W \quad .$$

If we now substitute this value into equation (3.1.14) and assume $\alpha = 0.78$ as discussed in section 2.4 we find that a reasonable minimum detectable strain expected for a typical MDS/9-633 sensor is

$$\Delta\bar{\varepsilon}_{min} \cong 10^{-9}\, m/m \quad .$$

The MDS/9-633 sensor is thus seen to be a highly sensitive strain detector. It is not, however, as sensitive as say a Mach-Zehnder interferometer since modal domain sensors are based on differential modal phase modulation, whereas the interferometer is based on absolute phase modulation [2]. By sacrificing some sensitivity, though, the modal domain sensor will likely gain

increased stability and immunity to environmental noise over the interferometer, making modal domain sensors, in general, a more practical approach to strain detection in many real world situations.

3.2 The MDS/9-850 Sensor

Similar to the MDS/9-633 sensor, it has been observed that when 850 nm light from a semiconductor laser diode is injected into a 9 μm core diameter fiber a symmetric two lobe pattern can be created at the fiber output which oscillates as a function of axial strain. Considering the same fiber as discussed in section (3.1) we see that the normalized frequency at $\lambda_o = 850\ nm$ is

$$V = 2.405 \frac{1215\ nm}{850\ nm} = 3.44 \quad .$$

From Figure 4 we find that this allows for the propagation of only the LP_{01} and LP_{11} modes, including all degeneracies. We will now show for the case of x-polarized injection that the oscillatory two lobe pattern is caused by the interference of the LP_{01} and even LP_{11} modes.

From equation (2.2.4) we see that the electric fields in the fiber core of the x-polarized LP_{01} and even LP_{11} are, respectively

$$\vec{E}_{01} = A_1 J_0(U_{01} r/a)\, e^{-j(\beta_{01} z - \psi_{01})}\, \hat{a}_x \qquad (3.2.1)$$

and

$$\vec{E}_{11} = A_2 J_1(U_{11} r/a) \cos\phi\, e^{-j(\beta_{11} z - \psi_{11})}\, \hat{a}_x \quad . \qquad (3.2.2)$$

Using equation (3.1.2) we can find the intensity distribution created by the interference of these modes to be

$$I = I_0 \left(A_1^2 J_0^2\left(\frac{U_{01} r}{a}\right) + A_2^2 J_1^2\left(\frac{U_{11} r}{a}\right) \cos^2\phi + 2A_1 A_2 J_0\left(\frac{U_{01} r}{a}\right) J_1\left(\frac{U_{11} r}{a}\right) \cos(\Delta\beta z - \Delta\psi) \cos\phi \right) . \qquad (3.2.3)$$

In equation (3.2.3) $\Delta\beta = \beta_{01} - \beta_{11}$, $\Delta\psi = \psi_{01} - \psi_{11}$ and $I_o = Y_1/2$. In addition, from Figure 4 we can find that $b_{01} = 0.730$ and $b_{11} = 0.325$, so that if equations (2.2.9) and (2.2.10) and Figure 4 are used with $V = 3.44$, $n_1 = 1.458$, $a = 4.5\ \mu m$ and $\lambda_o = 850\ nm$ we calculate $\Delta\beta$ to be $\Delta\beta = 1.1 \times 10^4\ m^{-1}$.

Note that in equation (3.2.2) the first term is the intensity of the LP_{01} mode alone and the second term is the intensity of the LP_{11} mode alone while the third term arises due to the interference of the LP_{01} and LP_{11} modes. For discussion purposes let us rewrite equation (3.2.3) as

$$I = I_o\{I_1(r) + I_2(r, \phi) + I_3(r, \phi, z)\} \quad . \tag{3.2.4}$$

Notice that $I_1(r)$ is azimuthally symmetric while $I_2(r, \phi)$ has a maximum at $\phi = 0$ and $\phi = \pi$. The third term $I_3(r, \phi, z)$ also has a maximum at $\phi = 0$ but has a minimum at $\phi = \pi$. In addition $I_3(r, \phi, z)$ is modified by the $\cos(\Delta\beta z - \Delta\psi)$ term which varies between -1 and +1 as z is varied. Thus we can see that for proper choices of A_1 and A_2 we should expect to see an output intensity pattern consisting of two lobes, one of which gets brighter as z varies, while the other gets dimmer. Figures 16-22 help visualize this behavior. Figures 16 and 17 show the intensity distributions of $I_1(r)$ and $I_2(r, \phi)$, respectively, while Figure 18 shows a sketch of the LP_{11} mode, which is similar in the coordinate ϕ to the output of the MDS/9-850 sensor at quadrature. Figure 19 shows $I_1(r) + I_2(r, \phi)$ when $I_3(r, \phi, z) = 0$, while Figure 20 shows $I_3(r, \phi, z)$ at a maximum. Finally, Figure 21 shows the entire intensity distribution of equation (3.2.4) when $I_3(r, \phi, z)$ is a maximum, with Figure 22 being a three dimensional plot of $I_1(r) + I_2(r, \phi)$ when $I_3(r, \phi, z) = 0$. In these figures it is assumed that $A_1 = 2A_2$, with all but Figure 18 showing plots normalized to $I_1(r)$ having a maximum intensity of unity. The choices of A_1 and A_2 are somewhat arbitrary and give indications as to the ratio of the input power existing in each mode. Here the choice of $A_2 = 2A_1$ was done to enhance the visualization of the behavior of the two lobes as a function of strain, which has been observed. This choice was made after evaluating

several plots of equation (3.2.3), with the amplitude coefficients taken as parameters. With $A_2 \cong 2A_1$ it was seen that the calculated output intensity distribution of the MDS/9-850 sensor most closely agrees with experimental observation. One must realize, however, that the ratio A_2/A_1 will be determined by source input conditions and must be some moderate value greater than one. If A_2/A_1 is less than unity the LP_{01} mode will dominate and only a single lobe will present at the output. If A_2/A_1 is much greater than unity only negligible power will exist in the LP_{01} mode and thus no interference will take place. For convenience we will proceed under the assumption that $A_2 \cong 2A_1$.

Some further comments concerning Figures 16-22 should be made. First, it should be noted that all line graphs are plotted in the plane where $I_1(r)$, $I_2(r, \phi)$ and $I_3(r, \phi, z)$ have maxima. Second, all the units of the spatial dimensions in Figures 16-22 are in microns. Third, the 3-D plot in Figure 22 is only valid in the region where $r = \sqrt{x^2 + y^2} \leq 4.5\,\mu m$. And finally, the sketches of Figure 18 are included to give a better visualization as to how the pattern caused by LP_{01} and LP_{11} modal interference will appear as seen looking toward the fiber end face. As with similar plots in earlier sections, these plots, with the exception of Figure 18, were generated with aid of the material in both Appendix C and Appendix D.

At this point it should be easily seen how this modal interference phenomena can be used as a sensor mechanism. If one adjusts the input conditions in such a way that $I_3(r, \phi, z)$ is zero at the fiber output end face, a maximum sensitivity quadrature point will have been created. If one then monitors one of the peaks at this quadrature point by spatially filtering out all but a small portion of the output pattern at this peak, a change in optical power through the aperture of the spatial filter will be directly related to any perturbations in the fiber.

Notice now that in Figure 21 if we monitor the peak of a lobe, then a maximum intensity at some amount of strain will occur at $r \cong 2.38\ \mu m$ in the maximum intensity plane. If we choose the lobe at say $\phi = 0$ and if it can be shown that

$$J_0^2\left(\frac{U_{01}r}{a}\right) + 4J_1^2\left(\frac{U_{11}r}{a}\right) \cong 4\,J_0\left(\frac{U_{01}r}{a}\right)J_1\left(\frac{U_{11}r}{a}\right) \qquad (3.2.5)$$

at $r \cong 2.38\ \mu m$, for $A_2 \cong 2A_1$, then we can obtain the reduced form for the core field intensity, equation (3.2.3), as

$$I = I'_0\{1 + \cos(\Delta\beta\, z - \Delta\psi)\}$$

or

$$I = I_p \cos^2\left(\frac{\Delta\beta\, z - \Delta\psi}{2}\right), \qquad (3.2.6)$$

where I'_0 has incorporated into it the terms of equation (3.2.5) after being factored from equation (3.2.3) and where $I_p = 2I'_0$ represents the peak intensity of a lobe. Indeed, by recalling the fiber parameters and using Figure 3 we can show for $r \cong 2.38\,\mu m$ that the quantities of equation (3.2.5) are the same to within 4.8 percent, with $A_2 \cong 2A_1$, so that the above simplification of the core intensity function is valid in the region of a lobe peak at either $\phi = 0$ or $\phi = \pi$. The only difference, recall, in these two lobes is that one will increase in intensity while the other decreases for small amounts of strain. Also, since the peaks of $I_2(r, \phi)$, $I_3(r, \phi, z)$ and $I_1(r) + I_2(r, \phi, z)$ don't precisely align with one another, with the peak radius of $I_2(r, \phi)$ being the largest, it is expected that the above simplification of the core intensity function should be valid for reasonable ratios of $A_2/A_1 > 2$ in the regions of the lobe peaks at $\phi = 0$ and $\phi = \pi$. Therefore from now on it will be assumed that we are discussing a sensor system in which the input has been adjusted so that two lobes of equal intensity are observed at the output under a no strain situation. Further, it will be assumed that the ratio A_2/A_1 is some reasonable value so that the interference takes place and that in the region about the peaks of the lobes the intensity can be approximated by equation (3.2.6).

We recall that by using equation (2.4.6), we can include in equation (3.2.6) the photoelastic effects of the fiber under strain, at the radial coordinate of a lobe peak, to give

$$I = I_p \cos^2\left(\frac{\Delta\beta\, \varepsilon_z\, L_f\, \alpha + \phi_o}{2} \right) , \qquad (3.2.7)$$

where $\phi_o = -\pi/2$ if we consider that we are monitoring the lobe which increases with strain from $I = I_p/2$ under a no strain situation. We recall that at quadrature $I_3(r, \phi, z) = 0$ and we have two lobes of equal intensity, one of which increases while the other decreases as a function fo strain. Using the same arguments as were used to arrive at the results of equations (3.1.14) and (3.1.15), we can show for small changes of strain, as averaged over the gage length of the sensing fiber, that $\Delta\bar{\varepsilon}_f$ can be measured from quadrature with the MDS/9-850 sensor as

$$\Delta\bar{\varepsilon}_f = \frac{\Delta V}{V_Q(\Delta\beta\, L_f\, \alpha)} , \qquad (3.2.8)$$

for the case of static strain and

$$\Delta\bar{\varepsilon}_f = \frac{\Delta V_{peak} \cos(\omega t)}{V_Q\, (\Delta\beta\, L_f\, \alpha)} , \qquad (3.2.9)$$

for the case of small amplitude time harmonic strain and small peak displacement vibrational strain. Note the similarity of these results (only $\Delta\beta$ takes on a different value) and those of equations (3.1.14) and (3.1.15) even though the sensing techniques are rather different. The sensitivities of the

MDS/9-850 and MDS/9-633 sensors are also comparable and equations (3.2.8) and (3.2.9) may be used to detect $\pm \Delta\bar{\varepsilon}_f$ from quadrature if there is an initial strain in the fiber.

As expected, using a laser diode in a modal domain sensor provides several advantages. First, due to the fundamental mode (LP_{01}) not needing to be extinguished for proper sensor operation, it is much easier to align the input. Also, since information will be taken from the sensor by monitoring the intensity variations of a lobe peak, alignment of the Q-point of the sensor is expected to be relatively simple. In addition, laser diodes are light weight, physically small and it is possible to find highly linearly polarized laser diodes operating at $\lambda_o = 780\ nm$ that are relatively inexpensive.

Although the preceding analysis has been for $\lambda = 850\ nm$, it is still valid for any source wavelength such that $V < 3.8$ so that the LP_{21} mode is still cutoff. For $\lambda_o = 780\ nm$, $V = 3.75$. In addition, for $\lambda_o = 780\ nm$, $\Delta\beta \cong 1.1x10^4\ m^{-1}$ as with 850 nm injection so that sensitivity is preserved.

The only apparent drawback to using laser diodes as sources is that they require special viewing equipment to observe the infrared radiation. This problem may, however, be overcome through the use of small, light weight in-line detection techniques presently under investigation. And finally, as laser diodes may be operated in a pulsed fashion, it may be possible to

simulate the use of a beam chopper in a detection system so that signal-to-noise ratio may be preserved for low frequency noise as would be present if there was, say, excess thermal drift.

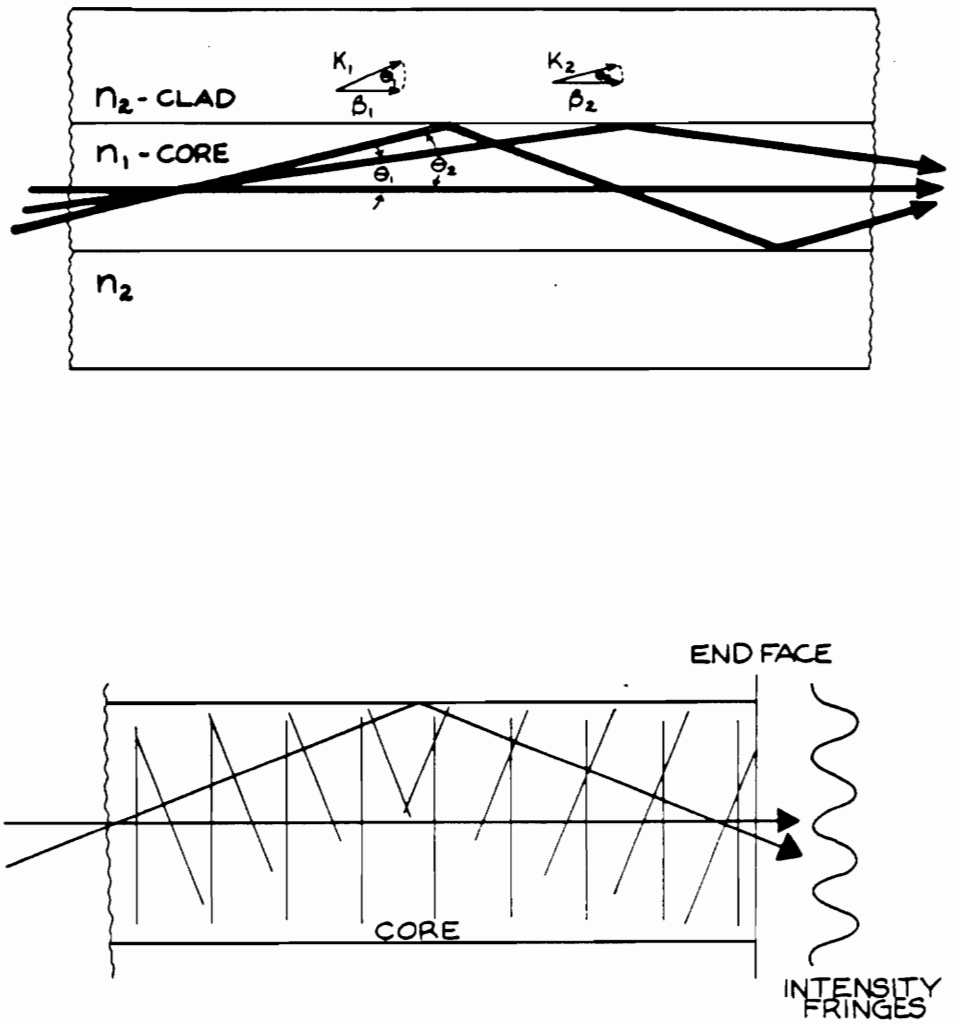

Figure 10. A simplistic look at modal interference

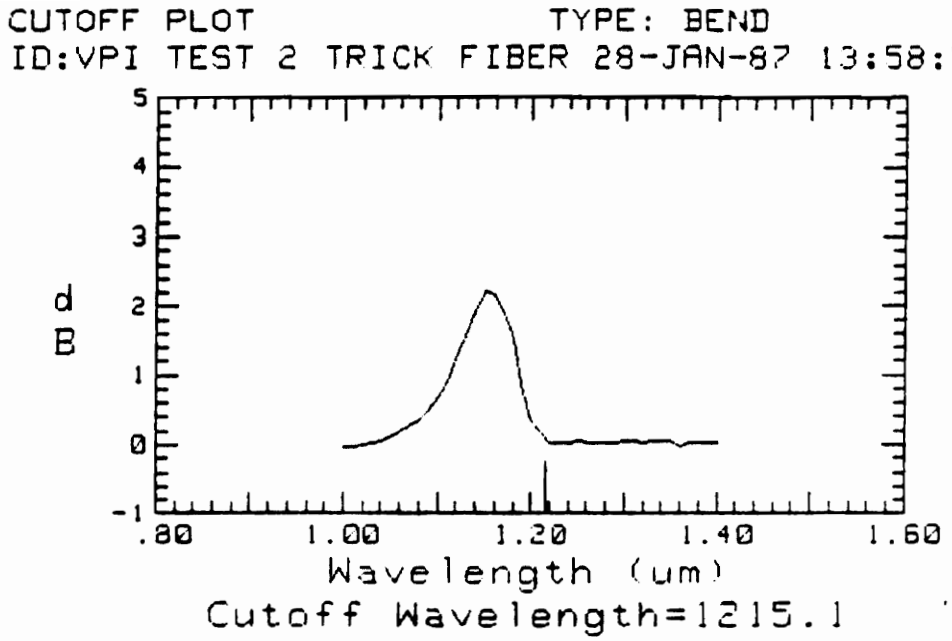

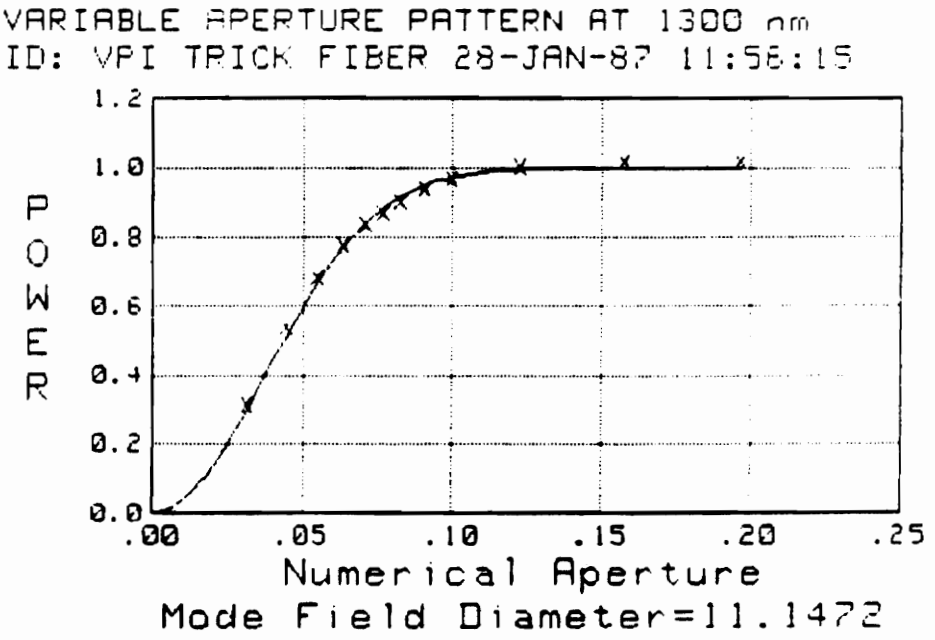

Figure 11. FOA-2000 fiber optic analyzer data

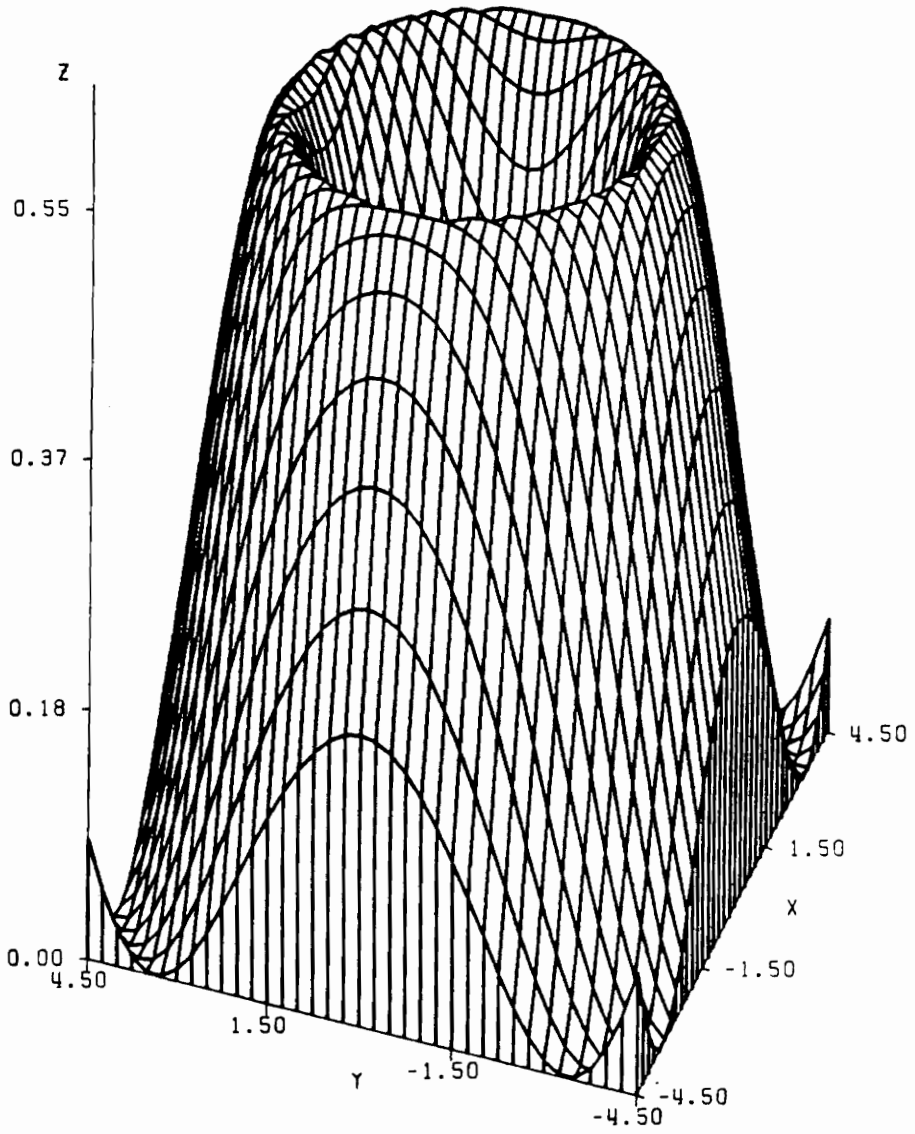

Figure 12. The MDS/9-633 background intensity term

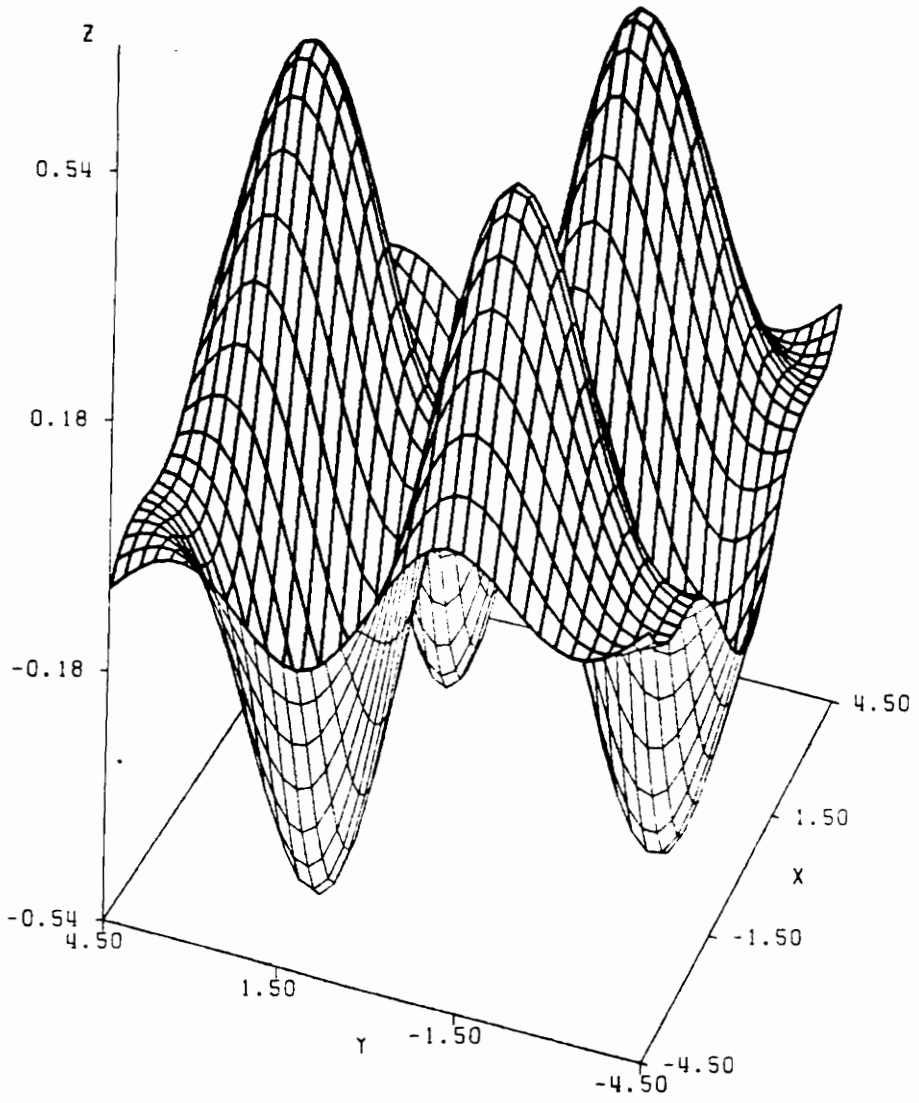

Figure 13. The MDS/9-633 strain modulated intensity term

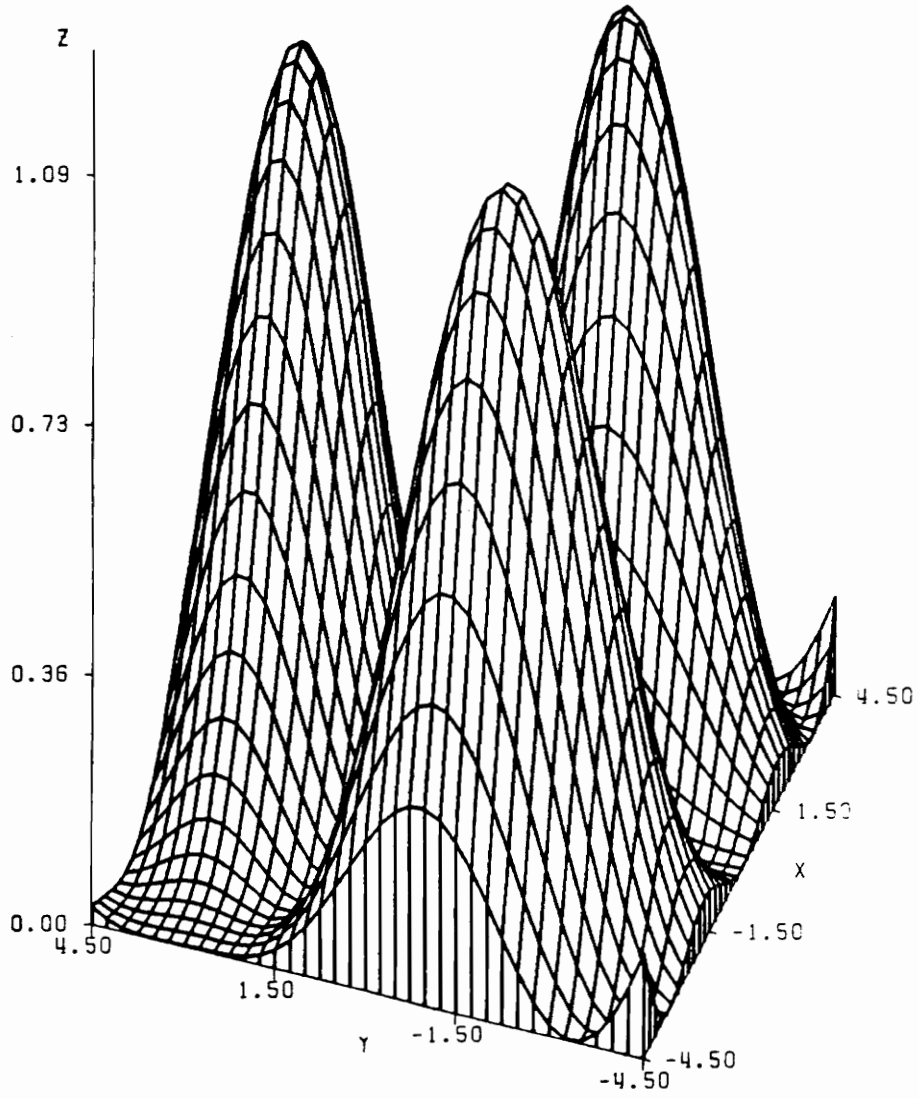

Figure 14. The total MDS/9-633 output intensity distribution

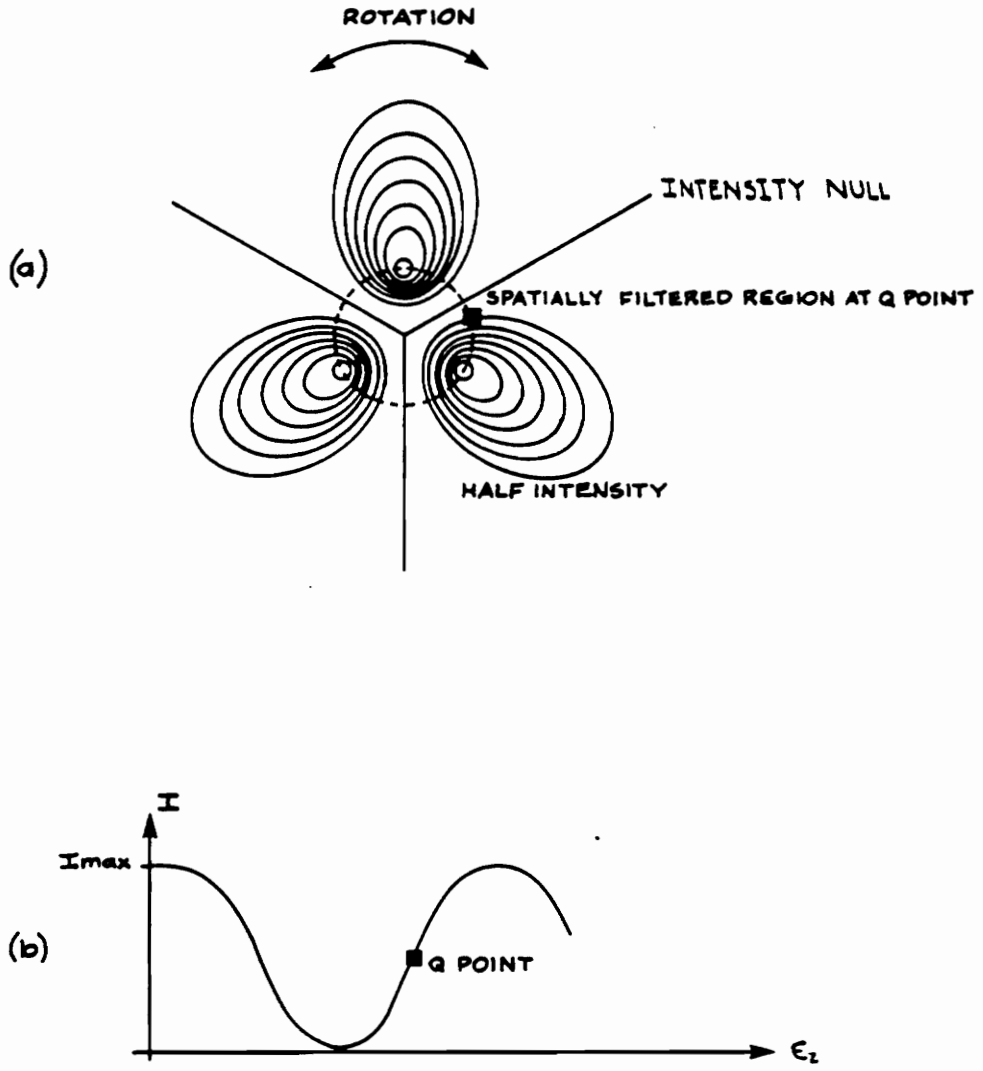

Figure 15. Axial view of the MDS/9-633 intensity distribution

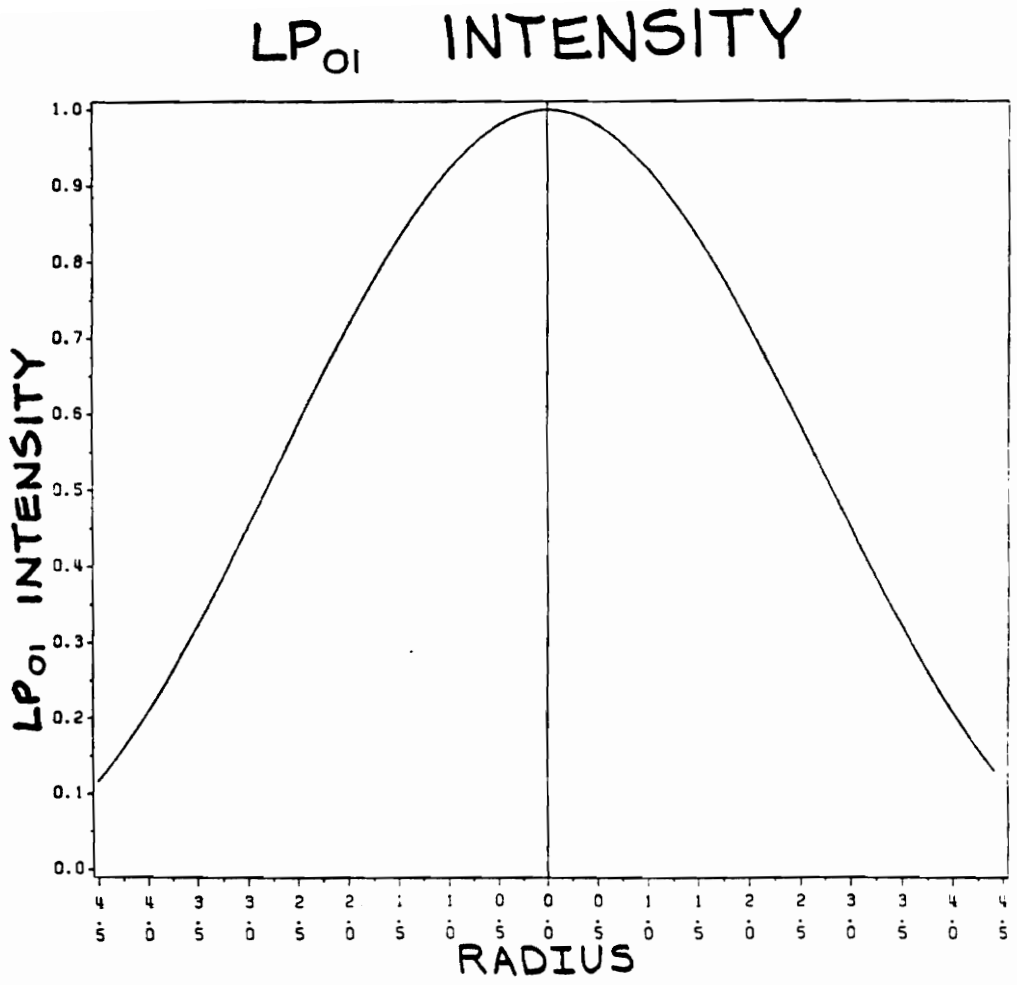

Figure 16. The LP_{01} mode intensity distribution of the MDS/9-850 sensor

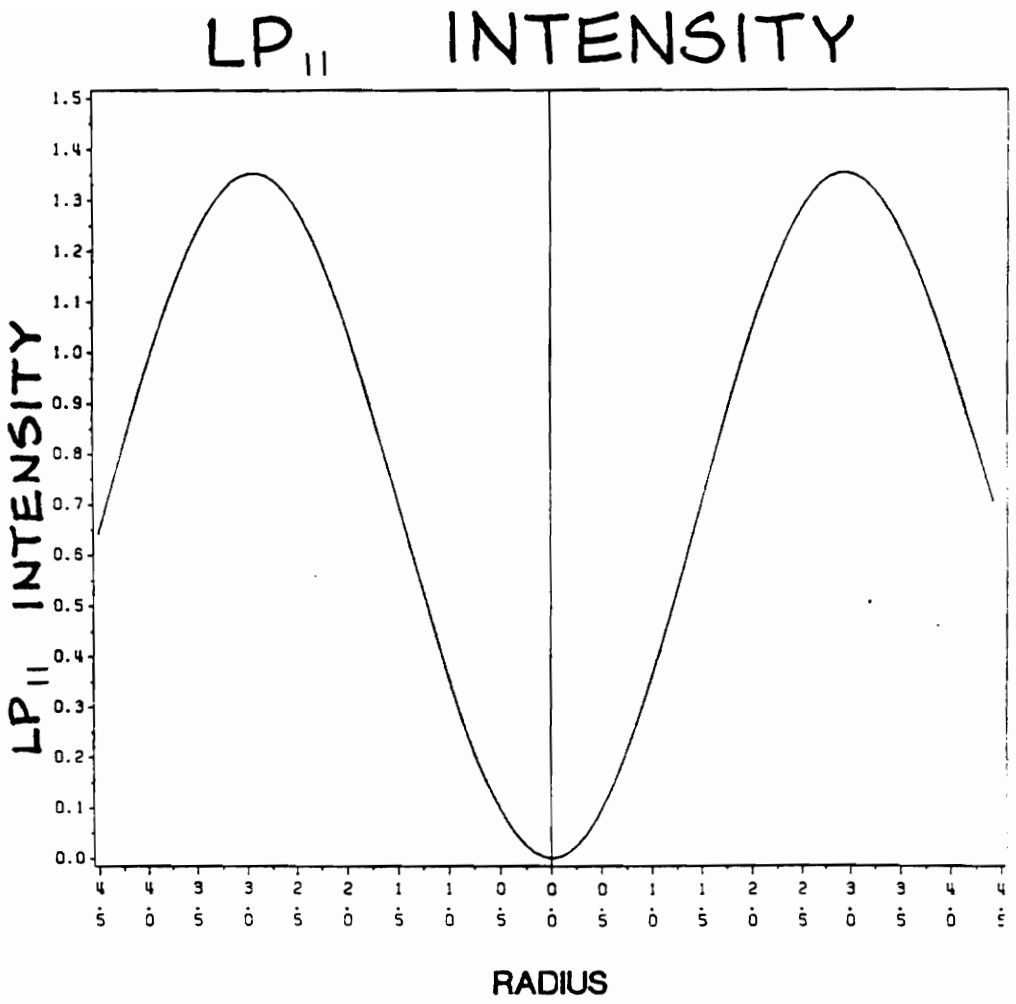

Figure 17. The LP_{11} mode intensity distribution of the MDS/9-850 sensor

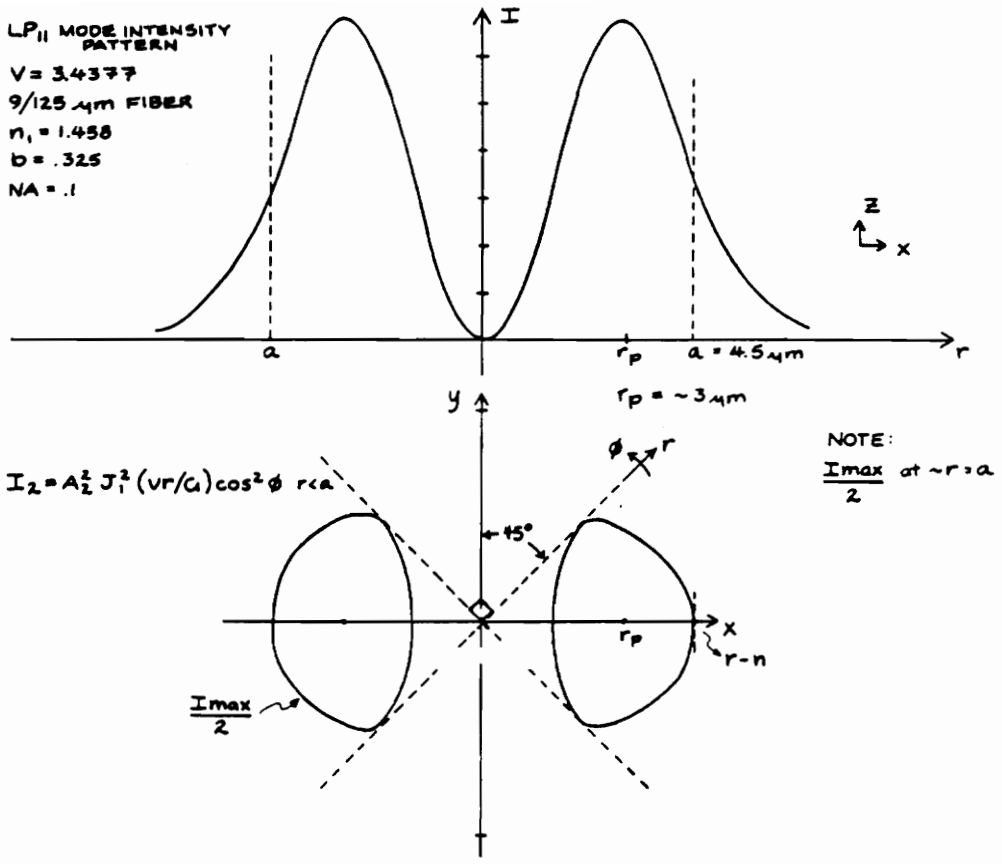

Figure 18. The LP_{11} mode intensity pattern

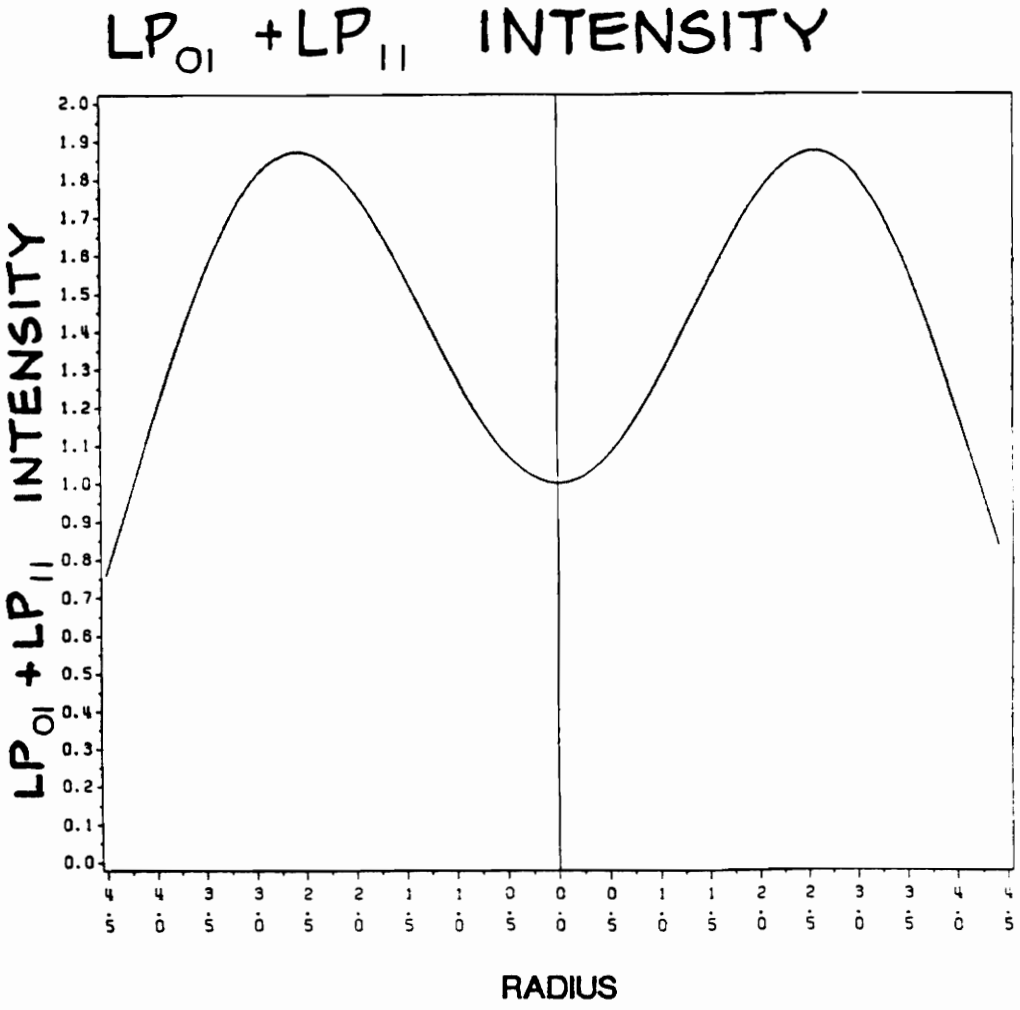

Figure 19. MDS/9-850 Intensity variation of $I_1(r)+I_2(r,\phi)$, at quadrature

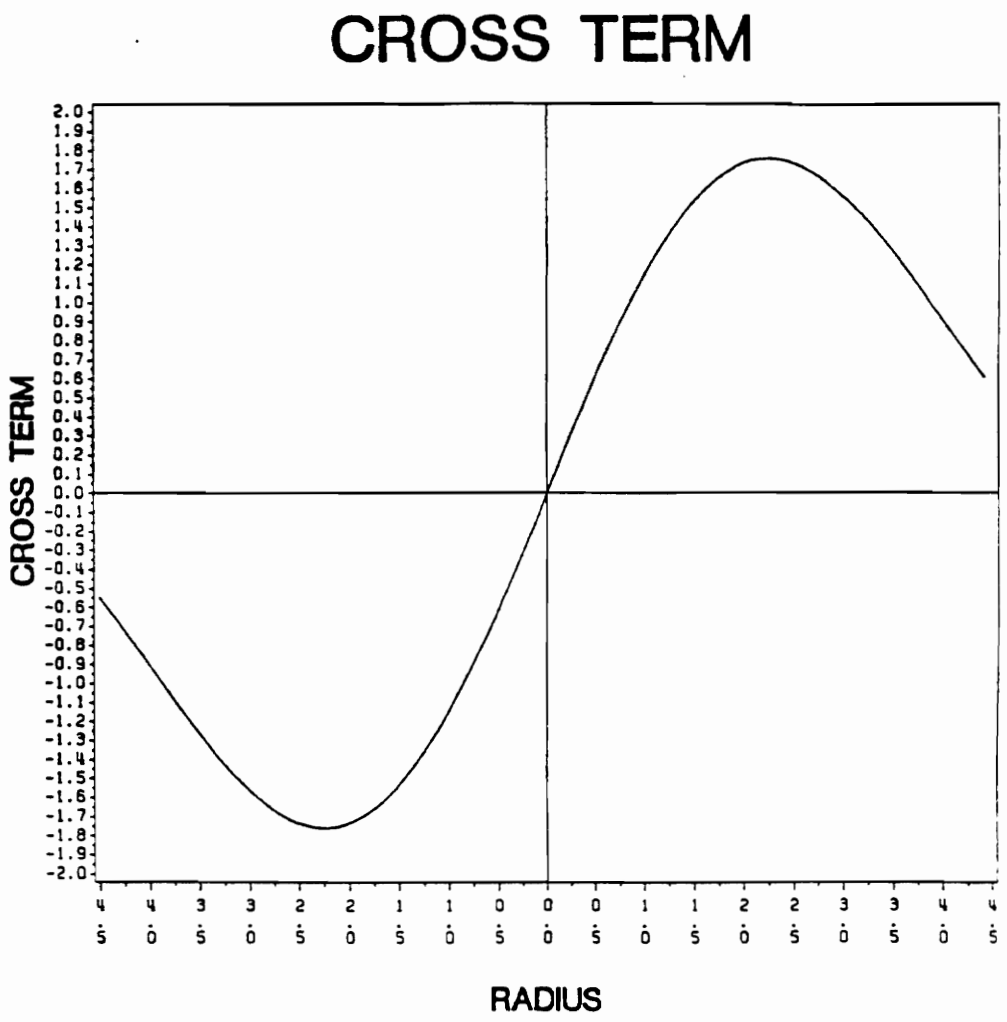

Figure 20. Intensity variation of the MDS/9-850 cross term $I_3(r,\phi,z)$, at a maximum

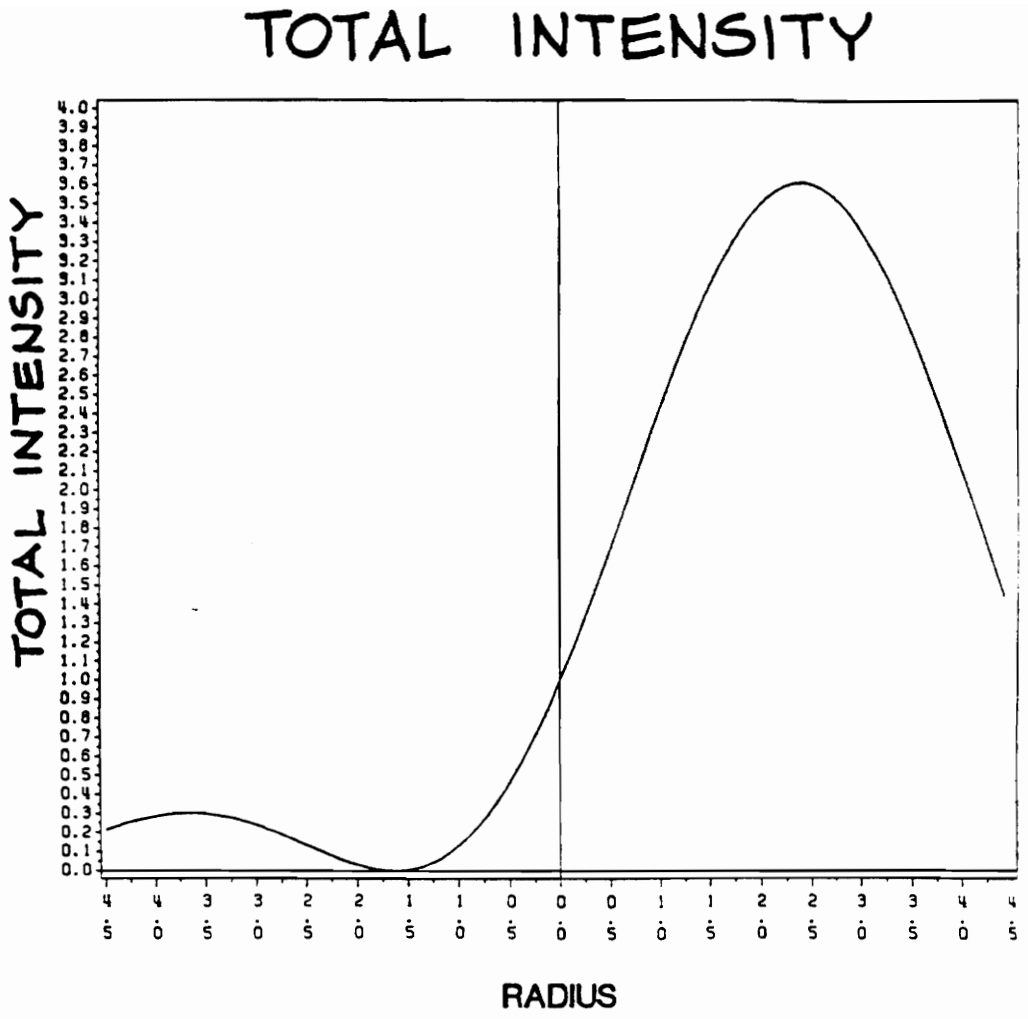

Figure 21. Total intensity pattern of the MDS/9-850 output when $I_3(r,\phi,z)$ is maximum

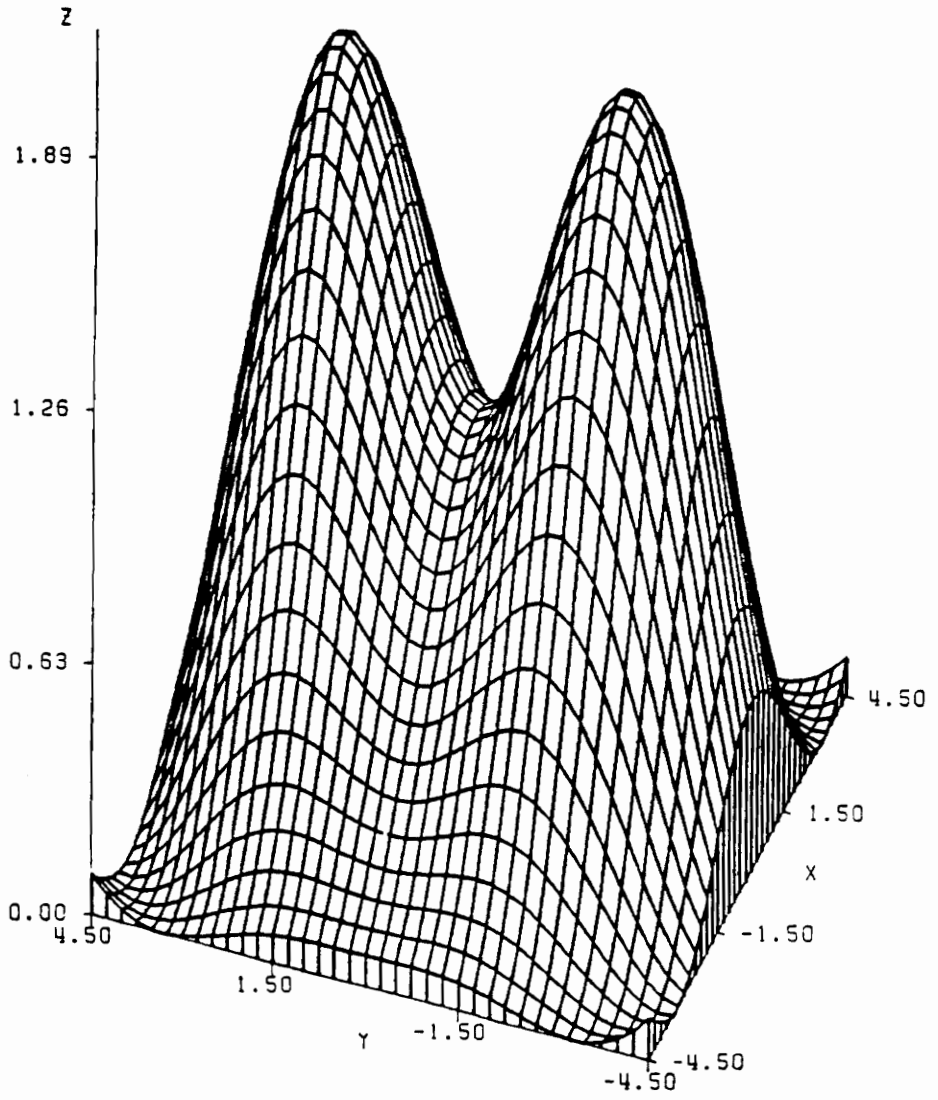

Figure 22. The MDS/9-850 intensity distribution at quadrature (3-D)

4.0 MDS/9-633 SENSOR EVALUATION

Although an MDS/9-633 sensor system will have practical limitations, it is easy to construct a working sensor system based of the MDS/9-633 technique using readily available optical laboratory equipment. In addition, by evaluating the MDS/9-633 sensor one can obtain insight about the practical aspects and performance characteristics of modal domain sensors in general. We begin with a description of the experimental system used to evaluate the MDS/9-633 sensor technique.

The experimental setup is shown diagrammatically in Figure 23. As seen, the emission from a He-Ne gas laser is focused through a microscope objective onto the end face of a 9μm core diameter fiber held in a fiber positioner. This fiber is of the same characteristics as the fiber discussed in section 3.1 and is attached in sequence to a static strain control device, a piezoelectric PZT

cylinder, a cantilever beam and a holding post at the output. The static strain control device simply consists of two plastic disks on which the fiber is wound, one of which has an attached push rod and is mounted on a rotateable base. As seen in Figure 24, tension is applied to the fiber between the two disks as force is placed on the push rod via a micrometer screw. In addition, so as to avoid appreciable bend loss in the fiber, the radius of the disks was approximately three inches.

The PZT cylinder following the static strain control device had wound upon it several turns of the 9 μm core diameter fiber and obtained its excitation from an external signal generator. As with the static strain control device, the purpose of the PZT cylinder was to aid in aligning the system quadrature point. For reasons to be discussed later, however, only the PZT cylinder was able to help achieve this goal.

After the PZT cylinder, the fiber was attached, along with a resistive strain gage, to a cantilever beam. Appendix A presents a detailed analysis of the strain characteristics of a loaded cantilever beam, as well as a discussion of the geometry of the fiber path on the beam necessary so that the strain induced in the optical fiber is identical to that induced in a resistive strain gage placed at the geometric center of the beam surface. The reader is encouraged

to review Appendix A before proceeding. Referring to Appendix A, the dimensions of the cantilever beam and the optical fiber path were chosen as

$$\begin{aligned} L &= 0.288\,m \\ L_1 &= 0.0254\,m \\ b &= 0.071\,m \\ h &= 0.0022\,m \\ r &= 0.0159\,m \end{aligned} \quad ,$$

where L is the beam length, L-L_1 is the length of the straight fiber segments and r is the radius of the curved portion of the fiber, with b and h being the beam width and thickness, respectively. With this geometry the change in average strain induced in both the optical fiber and the resistive strain gage is given as a function of load by

$$\Delta\bar{\varepsilon} = \frac{3mgL}{Ebh^2} \quad , \tag{4.0.1}$$

as shown in Appendix A, where m is the change in initial load mass and g is the acceleration due to gravity. Young's modulus E for the beam depends on the beam material and as our beam was constructed of aluminum $E = 6.9\text{x}10^{10}\,Pa$. In addition, for this beam the Poisson's ratio is $\nu = 0.33$, while the gage length of the fiber on the beam is

$$L_f = 2(L - L_1) + \pi r = 0.575\,m \quad .$$

Further, the optical fiber was mounted to the beam unstripped to prevent breaking and both the fiber and resistive strain gage were bonded to the beam using thermal-set epoxy.

The output end of the fiber sensor was attached to a holding post positioned a few centimeters from the photodetection circuit. The detection circuit consisted simply of a photodiode, reverse biased at nine volts, mounted on an x-y-z positioning stage. Load resistance was provided via a decade box. In addition, epoxied to the front of the photodiode (UDT model PIN-10D) was an iris which served as a spatial filtering device. Fully open the iris was 1.2 cm in diameter and when closed a 1.0 mm aperture remained. Typically, spatial filtering was done with the iris closed; however, the actual size of the spatial filter aperture is mostly irrelevant as long as it is small with respect to the output intensity distribution being monitored.

Not shown is the Wheatstone bridge and amplifier circuit used to detect small changes in resistance of the resistive strain gage. The output of this circuit and the photodetector were both connected in parallel to a digital voltmeter, an oscilloscope and a spectrum analyzer for data collection purposes. In addition, the entire system, except for measurement equipment, was mounted to a floating (pneumatically supported) optical table.

Finally, throughout the discussions to follow no account will be given to any system noise arising from sources other than the photodetection circuit and its associated load resistor. In addition, it will be assumed that the bonding of both the optical fiber and the resistive strain gage to the cantilever beam is perfect with no shearing of the fiber jacket occuring as strain is applied. These assumptions will not likely be valid outside of a laboratory environment.

4.1 Resistive Strain Gage Evaluation

As the resistive strain gage is a commonly used and well accepted instrument for measuring strain it was decided that a resistive strain gage would be used as a standard with which to compare the performance of the MDS/9-633 sensor. It was therefore important to evaluate the performance of the resistive strain gage used in our sensor system prior to all other measurements. As mentioned previously, the resistive strain gage was placed at the geometric center of the cantilever beam surface, so that as a function of load, the induced strain characteristics of the gage follow equation (4.0.1). In addition, as shown in Appendix B, the change in average strain in the beam as *measured* by the resistive strain gage is given by

$$\Delta\bar{\varepsilon} = \frac{-V_{out}}{V_{in}} \frac{4R_5}{S_g R_6} \left[\frac{1 - k_t \nu_0}{1 - k_t \nu} \right] , \qquad (4.1.1)$$

where V_{out} is the negative voltage measured (for positive strain) at the output of the inverting amplifier following the Wheatstone bridge circuit. The bridge, recall is used to allow small changes in strain to be detected. In addition the input V_{in} to the bridge circuit, as supplied by a regulated power supply, was measured to be 10.0 V, while the gain of the amplifier was measured to be $|R_6/R_5| = 179.78$. Individual values of R_5 and R_6 were measured to be 102.834 MΩ and 572.0 kΩ, respectively. These measurements and other similar ones to be presented later were made on a Solartron model 7061 digital voltmeter that was capable of displaying seven significant digits.

The specific resistive strain gage used was manufactured by Micro-measurements Corporation and had a nominal resistance R_o of 120.0 ± 0.18 Ω. In addition, the gage factor S_g was given as 2.095 ± .05 at 300°K, while the transverse sensitivity factor k_t was given as $k_t = 0.006$. Finally the Poisson's ratios in equation (4.1.1) are given as $\nu_0 = 0.285$ and $\nu = 0.33$ and represent the Poisson's ratios of the factory gage calibration beam and the aluminum experimental test beam, respectively. Refer to Appendix B for further details.

In order to evaluate our resistive strain gage, the beam was initally loaded with a 200 gram mass using the loading technique depicted in Figure 25(b). This was done to take any "slack" out of the system. The gage resistance was then measured and the other resistances of the bridge circuit adjusted (trimpots were used) so as to null the output. Additional load mass was then added to the beam with readings of V_{out} being taken as the excess load mass reached the values of 5, 10, 20, 30, 40, 50 and 100 grams. This procedure was repeated several times and a representative plot of data depicting the measured versus induced change in average beam strain is given in Figure 26. In particular, note the regression polynomial calculated for this data. As is seen, the calculated slope of the line deviates only slightly from the ideal case of unity slope. In addition, the y-axis crossing value can be shown to very closely correspond to the measurement uncertainty of the resistive strain gage.

If we now conservatively assume that our Solartron volt/ohm meter is uncertain to within plus or minus one digit in the fourth decimal place (for a given scale factor) we may calculate our minimum change in strain measurable with the resistive strain gage using the procedure outlined in Appendix B. With $dV_{out} = \pm 10^{-4}\ V$, $V_{in} = 10.0 \pm 10^{-4}\ V$, $R_5 = 572.0 \pm 10^{-4}\ k\Omega$ and $R_6 = 102.834 \pm 10^{-4}\ M\Omega$ we find that our minimum detectable change in average beam strain is $\Delta\bar{\varepsilon}_{min} = 0.21\ \mu m/m$, as measured with the resistive

strain gage. As this value also represents twice the absolute measurement uncertainty of the resistive strain gage (even with no applied load) it is seen that the y-axis crossing of the regression polynomial of Figure 26 very closely matches with the predicted value. We therefore see that our resistive strain gage provides a justifiable strain measurement standard.

4.2 Dynamic Strain Measurements

With confidence now gained in the performance of the resistive strain gage, the next task was to investigate the performance of the MDS/9-633 sensor. A discussion will be given in this section relating to the modal domain sensor's abilities to serve as a dynamic strain measurement device. Sections 4.4 and 4.5 will discuss static strain measurements.

Dynamic strain was induced in the cantilever beam using a setup as shown in Figure 25(a). As is seen, the action of the vibration exciter (Brüel & Kjær type 4809) was transmitted to the beam via a push rod. The ball and socket joint was used so that the deflecting force on the beam remained normal to the surface and so that the shaft of the vibration exciter was not subjected to any off axis stress. Notice, however, that this setup does not provide a way by which the force on the beam or the beam tip deflection can be measured as it

vibrates. All is known is that the beam can be caused to vibrate at the frequency of the signal input to the vibration exciter and that the amplitude of this vibration may be varied (in an uncalibrated way) by adjusting the input signal amplitude. For this reason it was important that the resistive strain gage behave properly so that the MDS/9-633 sensor readings could be compared to a reliable standard.

It was decided that as the beam vibrated the amplitude of the sinusoidally varying average beam strain, or peak average strain, would be the quantity to be measured. For the modal domain sensor, we have from section 3.1 that the measured peak average strain is given as

$$\bar{\varepsilon}_{f\,peak} = \frac{V_{peak}}{V_Q\,(\Delta\beta\, L_f\,\alpha)} \quad . \tag{4.2.1}$$

For the resistive strain gage we have from Appendix B that this same quantity is measured as

$$\bar{\varepsilon}_{RSG\,peak} = \frac{V_p}{V_{in}}\;\frac{4R_5}{S_g R_6}\left[\frac{1 - k_t v_0}{1 - k_t v}\right] \quad . \tag{4.2.2}$$

Note that in equations (4.2.1) and (4.2.2) we are considering that the beam is initially unloaded and that V_{peak} and V_p correspond to the amplitudes of the

sinusoidal signals generated at the output of the MDS/9-633 and resistive strain gage sensors, respectively.

To avoid both resonance conditions and damping of the vibration induced into the cantilever beam it was decided that the beam would be excited at as far below its fundamental frequency of vibration as possible. This frequency was determined by plucking the beam and allowing it to vibrate freely (with the push rod removed) and by then monitoring the output of the resistive strain gage sensor on a spectrum analyzer. As seen in Figure 27 the fundamental frequency of vibration was measured to be 21.6 Hz. Since the vibration exciter could not be reliably operated below 10 Hz this was chosen as the excitation frequency for dynamic strain measurements.

To conduct the experiment the fiber launch conditions were adjusted until a rotating three lobe pattern was observed. This was often facilitated by adjusting the tension in the length of fiber between the spools of the static strain control device, although no good explanation for this effect presently exists. The photodetector was then typically moved toward the fiber till the pattern just filled the open iris (a somewhat arbitrary act) and the Q-point was set using the PZT cylinder.

It was observed that when the PZT cylinder was excited at its resonance frequency of 38.5 kHz an appreciable small signal sinusoidal strain could be

imparted to the fiber, causing a small sinusoidal response at the photodetector output. The Q-point of the system was then set by using an x-y positioner to position the closed iris over the point of the pattern that gave the highest amplitude and least distorted sinusoidal response. This proved to be the most reliable way of setting the quadrature point and Figure 28 shows a highly aligned MDS/9-633 output signal observed during such an alignment. The top trace is the modal domain signal and has a peak-to-peak voltage of 80 mV. The bottom trace is the input to the PZT cylinder and has a peak-to-peak voltage of five volts. Both traces are at 38.5 kHz.

Conceivably, it should be possible to set the Q-point by locating the iris over the peak of a lobe and causing a static strain in the fiber so as to cause the pattern to rotate to the point where the iris is located half way between the maximum and minimum of a lobe. In practice this proved to be difficult, though, as it was often difficult to align the input in such a way that the three lobe pattern rotated properly through more than about twenty to thirty degrees. This was fine for small signal work but made alignment of the Q-point difficult using the "bulk effect" technique just described. Therefore only the "small signal" method of setting the Q-point, using the excited PZT cylinder, was used.

With the Q-point properly set, data was taken by recording the peak voltage out of each of the sensors on the cantilever beam, for varying amplitudes of the signal input to the vibration exciter, at the 10 Hz peak observed on a Spectrum analyzer. Recall that for all dynamic measurements the beam excitation is at 10 Hz. Plots of some of this data, converted to strain measurements using equations (4.2.1) and (4.2.2) are given in Figures 29, 30 and 35 with several polaroid photos corresponding to the data of Figure 30 being shown in Figures 31-34. These shall be discussed shortly.

For the data of Figures 29, 30, and 35, the load resistance was 50 kΩ and the input to the Wheatstone bridge V_{in} was taken from a nine volt battery. The value of α was taken to be $\alpha = 0.78$ in equations (4.2.1) and (4.2.2), as per the discussion of section 2.4, although this value will be seen to change when static strain measurements are undertaken. Recall also that $\Delta\beta = 1.2x10^4\, m^{-1}$ for the MDS/9-633 sensor. In addition, so as to make the data sets independant, the pattern and quadrature point were readjusted before each set of data was collected. For the data sets of Figure 29, 30 and 35 the Q-point voltages V_Q for the MDS/9-633 sensor were 1.2 V, 0.55 V and 0.35 V, respectively. Since the sensitivity of the MDS/9-633 sensor directly depends on the Q-point value of optical power through the spatial filter aperture, it is easy to see why the y-axis crossing is at a much higher value of strain in Figure 35 than it is in Figure 29, Note, however, the linearity and near unity

slope of all data in Figures 29, 30 and 35. Especially note that the y-axis crossings of the extrapolated data in each of these figures agrees well with the minimum expected detectable average beam strain calculated in section 3.1

Figure 31 shows a spectrum analyzer trace for both the MDS/9-633 sensor (top trace) and the resistive strain gage (bottom trace) at a point where the beam excitation is small. Note the output of each sensor is precisely at 10Hz and that the MDS/9-633 sensor has a much higher signal to noise ratio than the resistive strain gage sensor, thus indicating that the modal domain sensor will be able to provide strain measurement data long after the resistive strain gage has reached its minimum. Also, the spectrum analyzer gave the amplitude of each detected signal in *dBV RMS* so that peak voltage was calculated using the conversion

$$V_p = \sqrt{2}\ 10^{\left(\frac{V_{dBV\ RMS}}{20}\right)} \quad . \tag{4.2.3}$$

Furthermore, the data of Figure 31 corresponds to the first blackened data point in Figure 30 and is seen to be at the low end of the usable range of the resistive strain gage. Similarly, the polaroids of Figure 32 correspond to the second blackened data point of Figure 30 and are the result of a larger beam excitation. All data shown in these photographs were averaged eight times for visual purposes only. Finally, Figures 33 and 34 show the vibration exciter input signal and the noise floors of the strain sensors at quadrature with no

excitation, respectively. The bottom trace in Figure 34 corresponds, at 10 Hz, to the noise (-104.5 dBV RMS) of the MDS/9-633 sensor, while the top trace corresponds to the noise (-86.0 dBV RMS) of the resistive strain gage sensor. Using equations (4.2.1), (4.2.2) and (4.2.3) it is easily seen that these noise figures correspond to minimum detectable average beam strains of $\bar{\varepsilon}_f = 2.8x10^{-9}\, m/m$ and $\bar{\varepsilon} \cong 0.1x10^{-6}\, m/m$ for the MDS/9-633 and resistive strain gage sensors, respectively. This is in very good agreement with the predicted minimum detectable strains for each sensor and lends validity to the assumption of negligible excess environmental noise.

There are two final comments to make before moving to the next section. First, it should be mentioned that the maximum tip deflection never exceeded more than a few millimeters for all dynamic measurements. Second, although no values for beam displacement have been given, this can be calculated if the average strain in the beam is known using the relation

$$d = \bar{\varepsilon}\frac{4L^2}{3h} \quad , \tag{4.2.4}$$

where d is the beam tip displacement from its undisturbed position, L is the length of the cantilever beam and h is the beam thickness [1]. For the modal domain sensor, this gives us

$$d = \frac{V_{peak}}{V_Q \Delta\beta L_f \alpha}\left(\frac{4L^2}{3h}\right) , \qquad (4.2.5)$$

where the beam is assumed to be initially unloaded.

4.3 Extraneous Dynamic Modulation

At this point it is reasonable to wonder if there are any effects other than rotation of the three lobe intensity distribution which give rise to the signals discussed in the previous section. In order to investigate this, a properly rotating three lobe pattern was obtained and the detector positioned, with the iris fully open, so that the pattern filled the area of the detector face. The beam was then caused to vibrate at 10 Hz using the vibration exciter, with data taken as peak voltage readings at the output of both the photodetector and the resistive strain gage sensor circuits. Figure 36 shows this data taken for a series of varying signal amplitudes into the vibration exciter. The data is plotted as millivolts of extraneous modulation out of the photodetector versus resistive strain gage detected strain.

Figure 37 shows polaroid photos of the spectrum analyzer traces for large (top photo) and moderate (bottom photo) beam excitations. These correspond to

their respective blackened data points in Figure 36. Similarly, Figure 38 shows a polaroid photo of the spectrum analyzer trace for small beam excitation and corresponds to the blackened data point nearest the origin in Figure 36. For all photos in Figures 37 and 38 the top trace shows the output of the resistive strain gage sensor while the bottom trace shows the extraneous modulation output of the photodetector. Figure 39 shows the noise floors, with no excitation, for the measurements of extraneous modulation. Again, the top trace corresponds to the noise of the resistive strain gage (-88 dBV RMS) while the bottom trace corresponds to the noise of the photodetector output (-99.5 dBV RMS).

In a typical measurement situation, recall, the iris will be closed, leaving only a 1.0 mm aperture. This means that with the diameter of the iris open being 1.2 cm, only one 144^{th} of the pattern is spatially filtered in a normal measurement situation. This spatial filtering also takes place at approximately the average intensity of the pattern, at quadrature, so that the extraneous modulation figures shown in Figure 36 will be divided by 144 for measurement situations such as those described in section 4.2. For the largest extraneous modulation reading of Figure 36 (-62.1 dBV RMS or 1.11 mV), the corresponding value after spatial filtering is 7.7μV (-105.26 dBV RMS). This is easily seen to be well within the noise of the optical sensor output, even as shown in Figure 34. We thus conclude that the results presented in section 4.2

are entirely due to three lobe rotation and that extraneous modulation effects are entirely negligible.

As a final comment for this section, it has been suggested that, though small, the extraneous modulation effects are due to bend loss. If this were true, however, a peak at 20 Hz would be found due to bend loss occuring when the fiber both goes into tension and compression as the beam vibrates, but no such peak was observed. A more likely reason for the extraneous 10 Hz modulation is that some 10 Hz excitation is being transmitted to the floating table as the cantilever beam is forced to vibrate. Because the 10 Hz extraneous modulation figures are small, though, it is evident that the floating table is properly performing its function of excess vibration suppression, as expected, even though a vibrating structure is attached rigidly to it.

4.4 Static Strain Measurements (First Attempt)

It was also of interest to study the static strain measurement capabilities of the MDS/9-633 sensor. As with the resistive strain gage evaluation measurements, the cantilever beam was loaded as shown in Figure 25(b), with masses periodically added to the basket in excess of an initial load mass of 200 grams. Now, however, the change in average beam strain, as measured by the

MDS/9-633 sensor, was to be compared to the known *induced* change in average beam strain caused by varying the load mass. Recall that the induced change in average beam strain is given as

$$\Delta\bar{\varepsilon} = \frac{3mgL}{Ebh^2} \quad , \tag{4.4.1}$$

where m is the change in load mass. Further recall that this same quantity, as measured by the MDS/9-633 sensor, is given by

$$\Delta\bar{\varepsilon}_f = \frac{\Delta V}{V_Q \Delta\beta L_f \alpha} \quad , \tag{4.4.2}$$

as was shown is section 3.1 and where $\Delta\beta = 1.2x10^4\, m^{-1}$.

As before, the input to the optical fiber was adjusted until a properly rotating three lobe pattern was observed and the Q-point was adjusted, with the initial load mass in place, using the excited PZT cylinder. Mass was then added to the basket and ΔV measured (this time through use of a strip chart recorder) as the excess load mass reached 50, 100, 150, 200, 250 and 300 grams. It was observed, however, during early static loading tests that there was appreciable pattern drift over a period of a minute or so. It is believed that this drift is attributable to the static strain control mechanism and due in part to jacket shear for large amounts of induced static strain (recall it was mentioned

earlier that obtaining a rotating three lobe pattern was often facilitated by tensioning the fiber using the static strain control device). As the need for loading, unloading and settling the basket make the procedure for taking static strain data much more lengthy (1-2 minutes) than the procedure for taking dynamic strain data (<30 seconds) it was necessary to fully release the tension of the fiber in the static strain control device when static strain measurements were to be attempted.

In addition, preliminary plots of measured versus induced strain data gave regression lines whose slope was often noticeably different from unity. This was believed to be due to the physical parameters leading to the calculation of α, in equation (4.4.2), not being precisely known for the fiber being used.

In an attempt to directly measure α, the launch conditions were adjusted until a three lobe pattern was obtained which exhibited proper rotation over greater than 300°. With the fiber between the spools of the static strain control device just taut, the tension in the fiber was increased by turning the micrometer screw until the pattern rotated 120° (lobe peak to lobe peak). The change in the micrometer setting was then recorded and the tension in the fiber quickly released. This procedure was repeated several times and it was determined that the micrometer was advanced an average of 691μm for 120° rotation. The

change in length ΔL_{120} of the fiber between the spools was therefore approximately

$$\Delta L_{120} = r_1 \sin^{-1}\left(\frac{691\mu m}{r_2}\right) = 564.75\,\mu m \quad ,$$

where $r_1 = 7.62$ cm and $r_2 = 9.32$ cm represent, respectively, the radius of the rotating spool and the length of the push rod. This indicates that a change in length of 141.19 μm is needed to cause a rotation from quadrature to the nearest lobe peak (a 30° rotation).

From equation (3.1.11) we can solve for the change in fiber length required to cause pattern rotation from quadrature to the nearest lobe peak as

$$\Delta L_{30} = \frac{2\pi}{4\,\Delta\beta\,\alpha} \quad , \qquad (4.4.3)$$

where, recall, $\Delta\beta = 1.2x10^4\,m^{-1}$ for the MDS/9-633 sensor. With $\Delta L_{30} = 141.19\,\mu m$ we can thus solve for α to find $\alpha = 0.92$, on average, for our fiber.

New data was now taken for $\alpha = 0.92$, with $R_L = 50\,k\Omega$. See Figures 40 and 41 for plots of this data and note the near unity slope for each of these figures. In addition, the quadrature point voltage V_Q was 25.8 mV and 23.1 mV for the data of Figures 40 and 41, respectively.

It is interesting to note that the highest point on the regression line of Figure 40 occurs at $\Delta\bar{\varepsilon}_f = 104.5\ \mu m/m$ or $\Delta L_f = \Delta\bar{\varepsilon}_f L_f = 60.1\ \mu m$. This indicates that the response of the MDS/9-633 sensor stays linear for ΔV, in equation (4.4.2), approximately as large as $0.66V_Q$. The dynamic range for this linear response region can thus be found, in decibels, as

$$DR = 10 \log \left| \frac{\Delta P_{max}}{\Delta P_{min}} \right|$$

$$DR = 10 \log \left| \frac{0.66 P_Q}{\frac{1}{\mathscr{R}} \left(4qB(\mathscr{R} P_Q + I_D) + \frac{8k_B TB}{R_L} \right)^{\frac{1}{2}}} \right| . \qquad (4.4.4)$$

where ΔP_{min} was given in equation (2.3.10) and where P_Q is the optical power through the spatial filter aperture at quadrature. Recall that the voltage at the output of the photodetection circuit is directly related to the optical power through the spatial filter by the photo diode responsivity $\mathscr{R}$ and the load resistance R_L. Using the system parameters used in section 3.1 to determine the minimum detectable strain of the MDS/9-633 sensor we thus find that the dynamic range of this sensor, in the linear region, is approximately 52 dB.

4.5 Static Strain Measurements (Second Attempt)

Due to the drift problems encountered using the static strain control device shown in Figure 24 it was decided that this device would be redesigned and additional static strain measurements attempted. Shown in Figure 42 is the resulting new static strain control device. As seen, a length of optical fiber is attached to two axially aligned mounts, one of which exhibits axial translation as the motor shaft turns. The motor used was a 200 step per revolution stepping motor and connected between the motor shaft and the movable mount was a #2 threaded rod with fifty-six threads per inch. As the gage length of fiber between the two mounts was measured to be $L_f = 0.522\,m$, then for every step applied to the motor the change in induced average strain in the fiber was $\Delta\bar{\varepsilon} = 4.345\,\mu m/m$.

This new static strain control device provided several advantages. First, the induced strain in the fiber was purely axial, as opposed to the axial and possibly transverse strains induced in the fiber wound on the spools of the old static strain control device. Second, there was a very simple relation between the number of steps applied to the motor and the strain induced in the fiber, as discussed above. Most importantly, though, was that there was no jacket shear in the fiber between the stationary and movable mounts. This effect was

eliminated by first stripping the fiber of its jacket at the points where it was clamped and by then bonding directly to the bare fiber a length of stainless steel tubing. Due to the more rigid nature of the stainless steel tubing and the epoxy used to bond it to the bare fiber the, induced strain was more faithfully transmitted to the optical fiber, with no relaxation of the tension occuring due to elastic stretching of the polymer jacket. Indeed, it was observed that negligible pattern drift occurred over a period of several days with the fiber under significant tension. The only disadvantage to using the new static strain control device was that the fiber between the clamps had a tendency to break just at the point where the fiber exited the stainless steel tubing. This is believed to be due to slight axial misalignments of the fiber mounts causing high stress concentrations in the regions of these breaks.

As before, the input to the fiber was aligned such that a three lobed intensity distribution was present at the output that exhibited pure rotation. Pains were taken to ensure that the alignment was such that this rotation would occur over most of a full revolution. Then, using a linear x-y positioning stage the spatial filter aperture was positioned over the peak of a lobe, with steps then being applied to the motor to cause the pattern to rotate to the point where the spatial filter monitored the point located half way between the maximum and minimum intensity points of a lobe. Due to the discrete nature of the increases in applied strain, though, the proper quadrature point was often overshot,

requiring final alignment using the x-y positioning stage. With the operating point thus properly set, strain was measured as additional steps were given to the motor.

As before, the strain measured by the MDS/9-633 sensor followed equation (4.4.2). In addition, as before, it was noticed that plots of preliminary measured versus induced strain data gave a linear regression line with slope different from unity when α was taken as $\alpha = 0.78$. By fitting only the first point of this preliminary data to a regression line of unity slope it was determined that $\alpha = 0.86$ was a more acceptable value. Assuming $\alpha = 0.86$ additional data was taken and is shown in Figures 43 and 44.

Two final comments are necessary. First, the method by which α was determined for the data plotted in Figures 43 and 44 is admittedly questionable due to the preliminary data used to determine α possibly not being independant from the data subsequently taken and presented. There simply was no way in which a reliable and independant determination of α could be determined with the setup used. Indeed, an independant determination of the photoelastic coefficients used to calculate α is likely to be an involved task in itself. It is believed, however, that photoelastic effects must be considered as the fiber is subjected to strain and that the analysis leading to equation (4.4.2)

is correct. The value of α, however, and its constituent terms is very much open to question.

The other comment necessary is that this second round of static strain measurement data was taken using a UDT model 81 Optometer. This instrument directly displayed the optical power passing through the spatial filter aperture and incident on the face of the detector head. As per the discussion in section 3.1 leading to the result of equation (3.1.14), however, ΔP and P_Q may be directly substituted for ΔV and V_Q in equation (4.4.2). The value of P_Q was 0.13 μW and 0.16 μW for the data plotted in Figures 43 and 44, respectively.

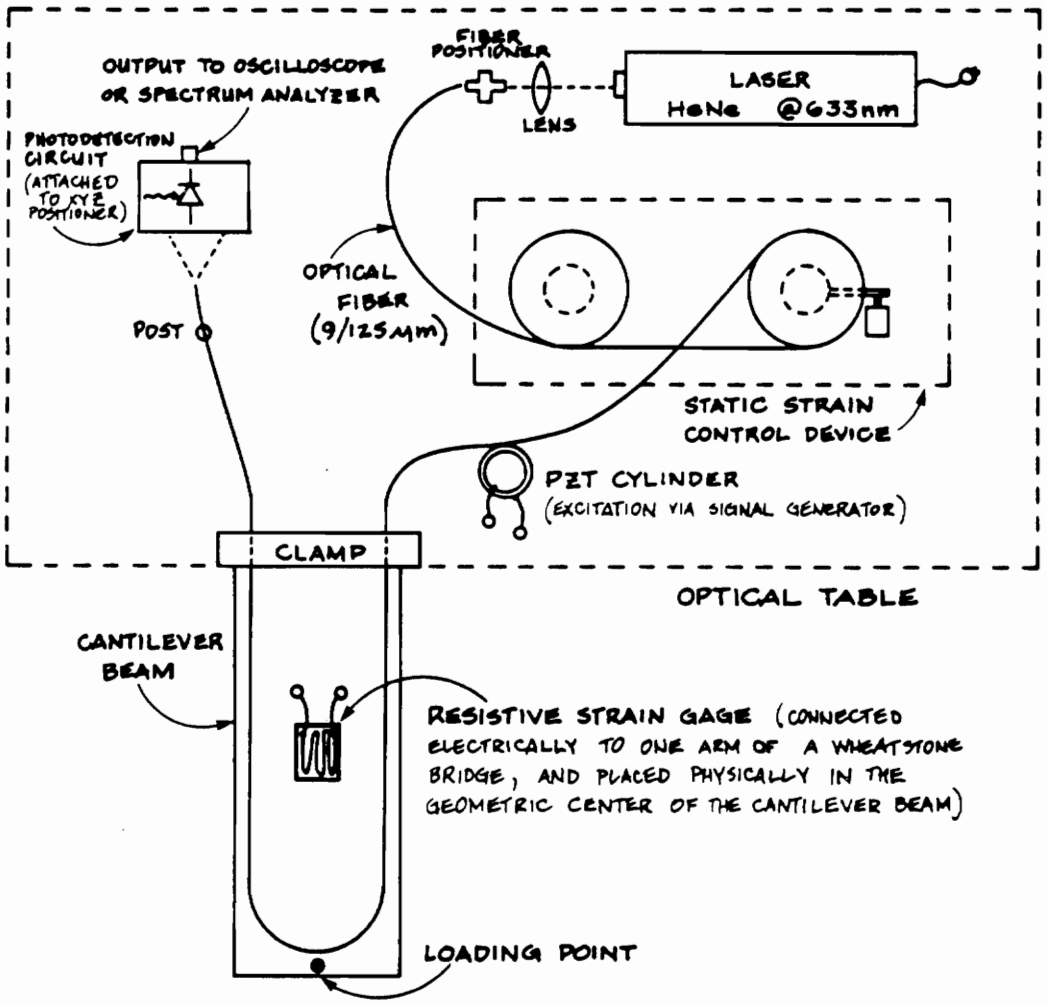

Figure 23. Experimental MDS/9-633 system

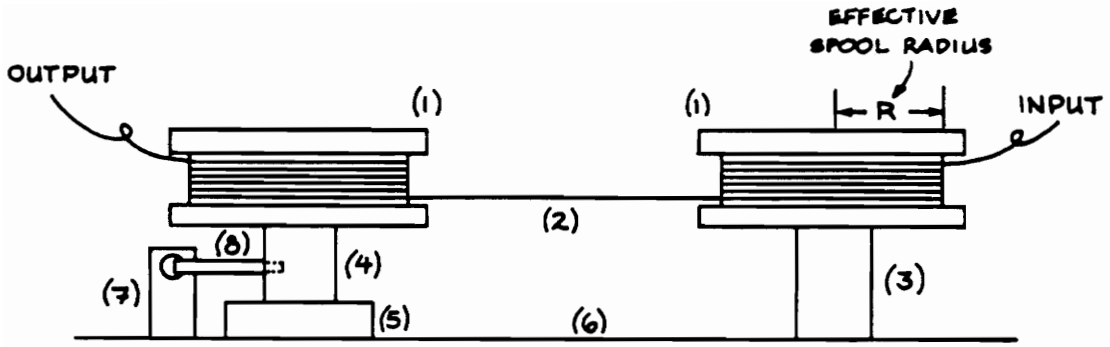

(1) SPOOL ON WHICH OPTICAL FIBER IS WOUND
(2) OPTICAL FIBER UNDER TENSION
(3) RIGID MOUNT BETWEEN SPOOL & OPTICAL TABLE
(4) RIGID MOUNT BETWEEN SPOOL & ROTATABLE BASE
(5) ROTATABLE BASE
(6) OPTICAL TABLE
(7) MICROMETER SCREW DEVICE TO PROVIDE FORCE ON THE PUSH ROD
(8) PUSH ROD

Figure 24. First static strain control device

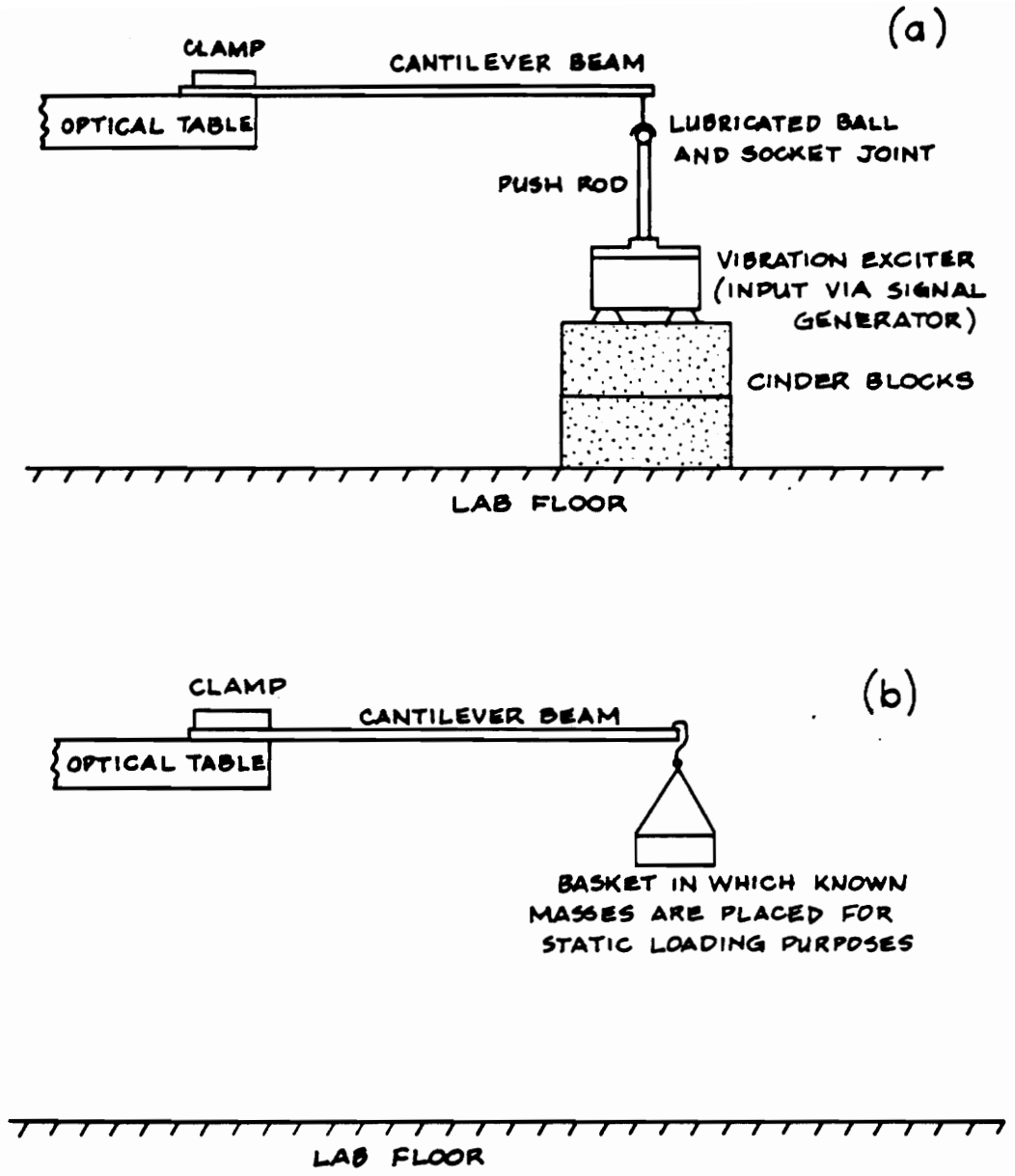

Figure 25. Loading schemes of the experimental MDS/9-633 sensor system

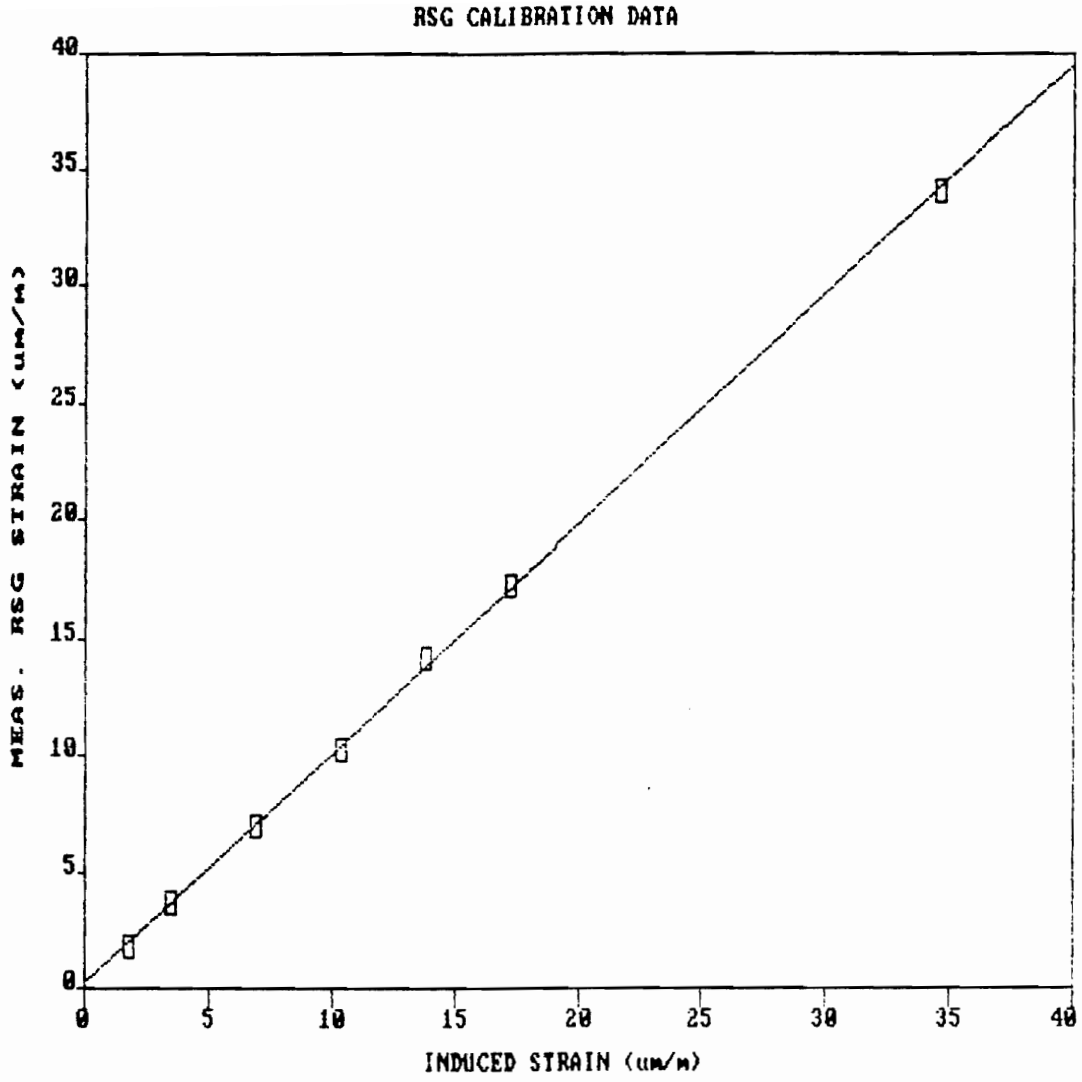

THE REGRESSION POLYNOMIAL OF LINE 1

(2.212E-01) + (9.822E-01)*X
THE VARIANCE - 2.304E-02

Figure 26. Resistive strain gage calibration/evaluation data

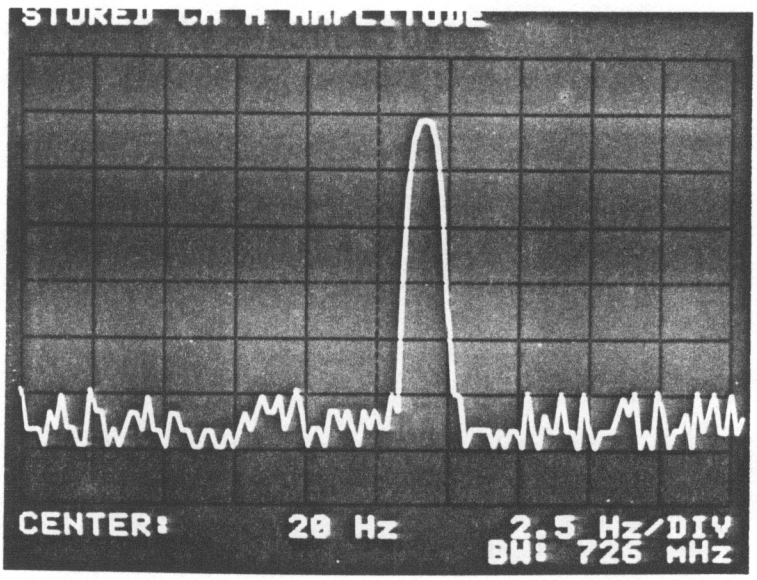

Figure 27. Cantilever beam natural frequency of vibration

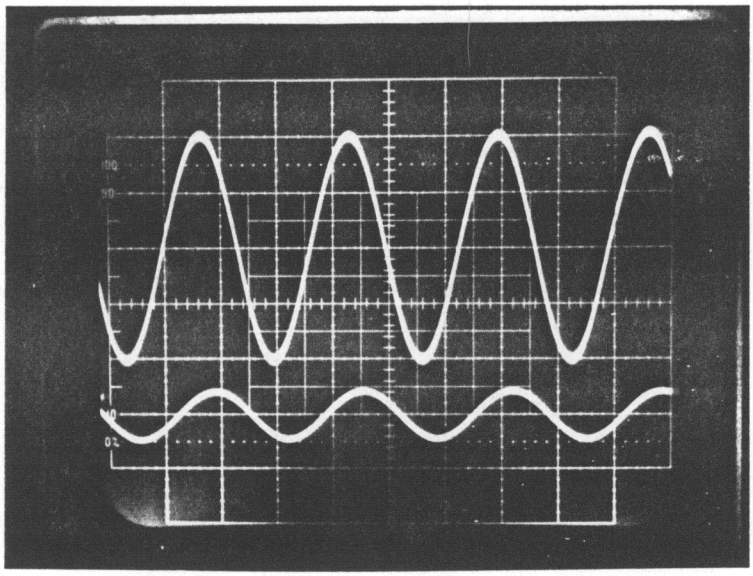

Figure 28. Highly aligned MDS/9-633 sensor output (see text for details)

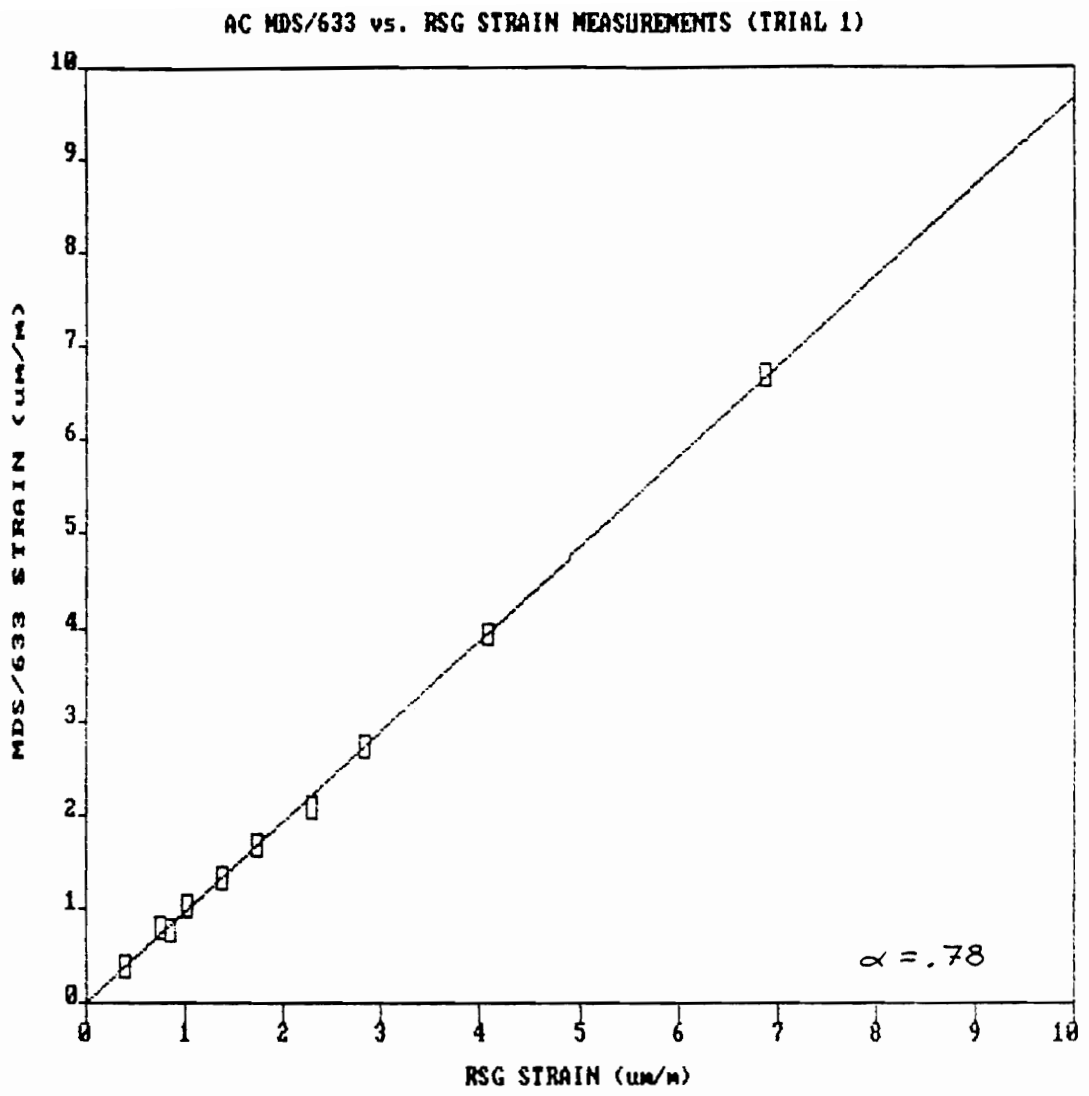

THE REGRESSION POLYNOMIAL OF LINE 1

(-6.875E-03) + (9.688E-01)*X
THE VARIANCE - 2.423E-03

Figure 29. MDS/9-633 dynamic strain measurement data (trial 1)

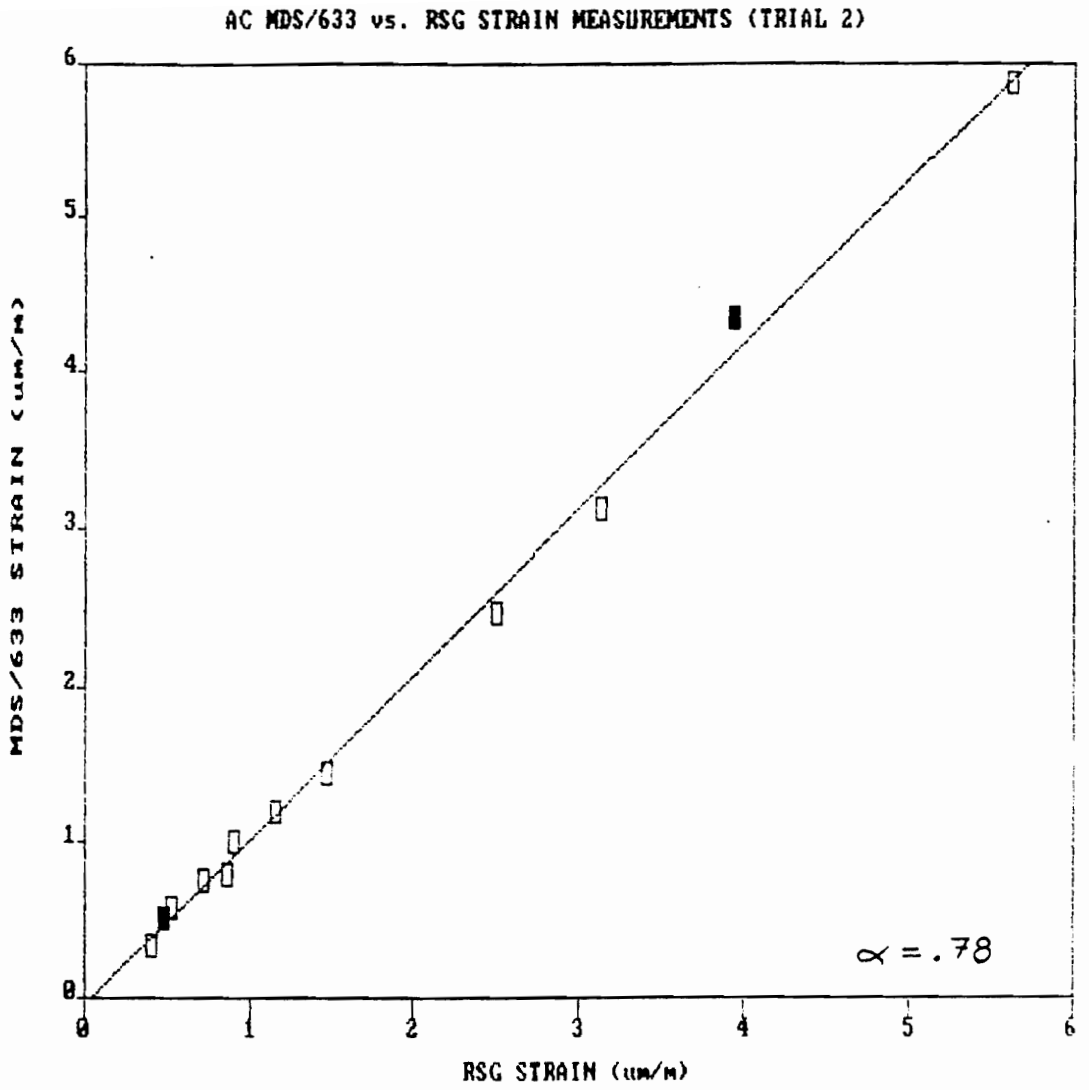

THE REGRESSION POLYNOMIAL OF LINE 1

(-4.101E-02) + (1.055E+00)*X
THE VARIANCE - 9.740E-03

Figure 30. MDS/9-633 dynamic strain measurement data (trial 2)

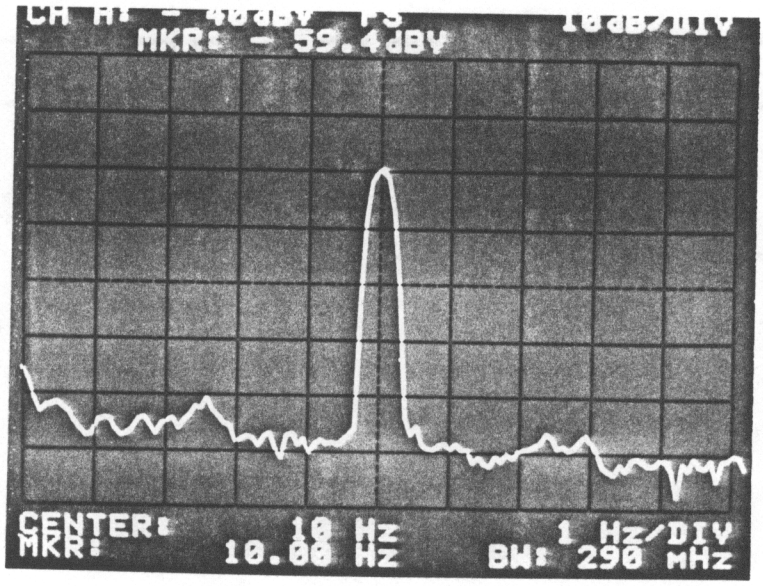

(a)

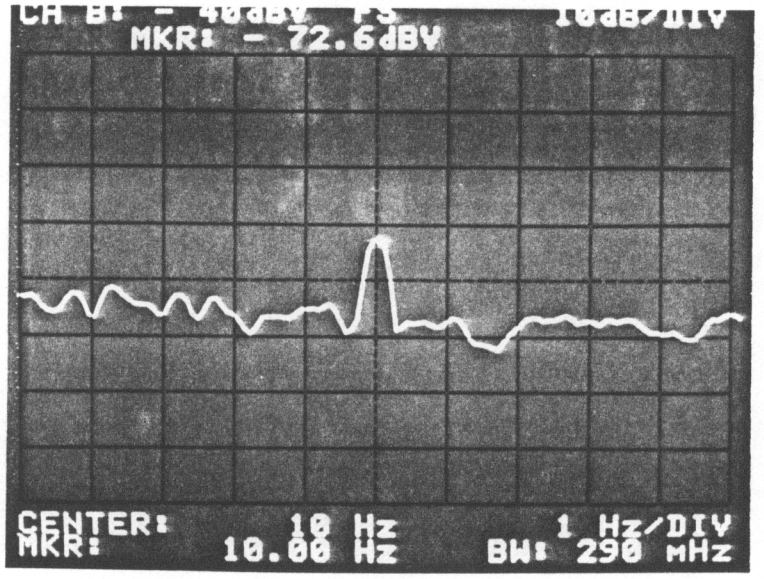

(b)

Figure 31. MDS/9-633 and resistive strain gage outputs for small excitation

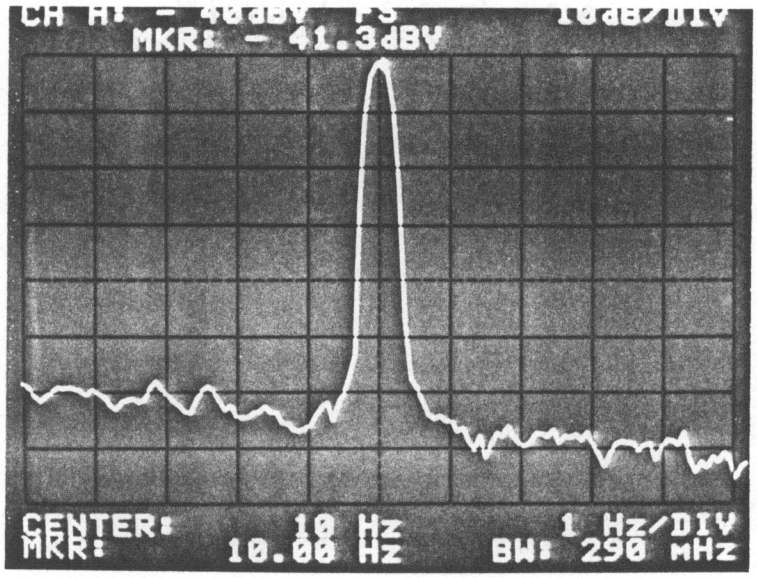

(a)

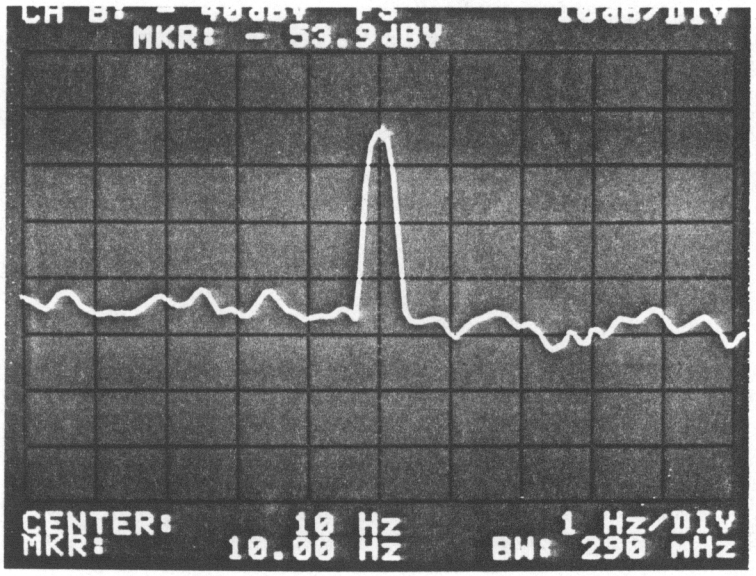

(b)

Figure 32. MDS/9-633 and resistive strain gage outputs for large excitation

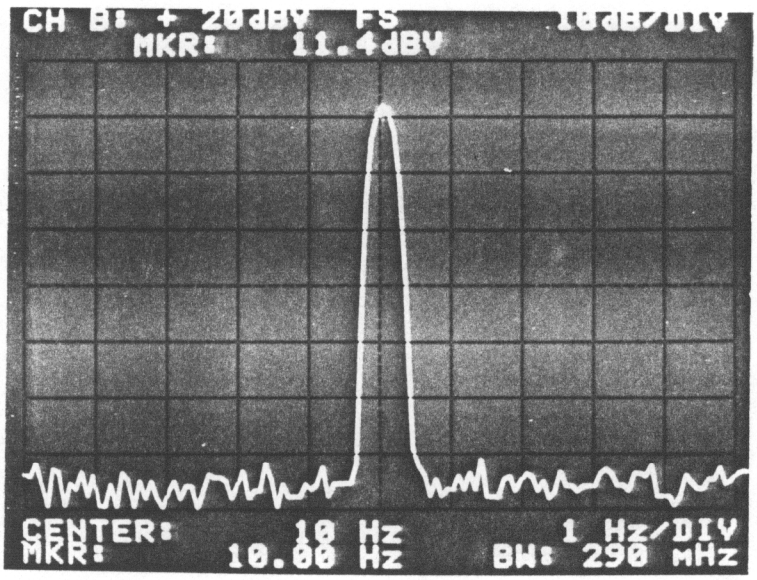

Figure 33. Input signal of the vibration exciter

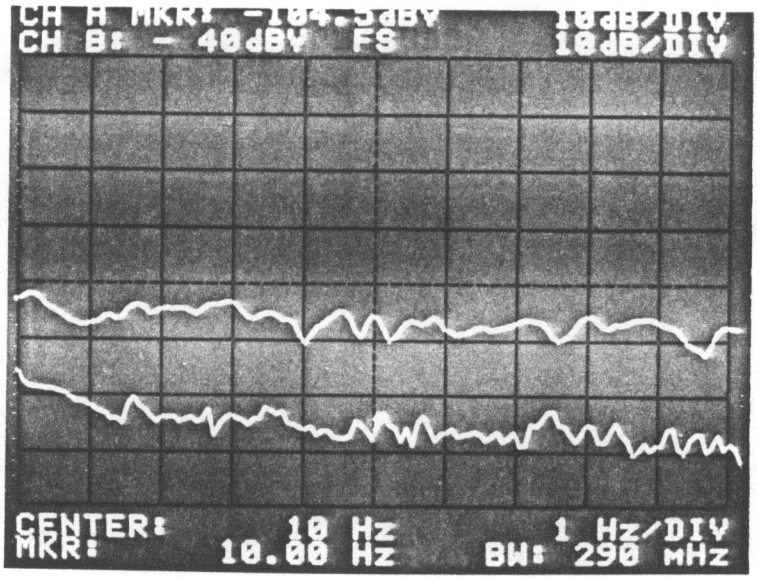

Figure 34. Noise floors of the MDS/9-633 and resistive strain gage sensors

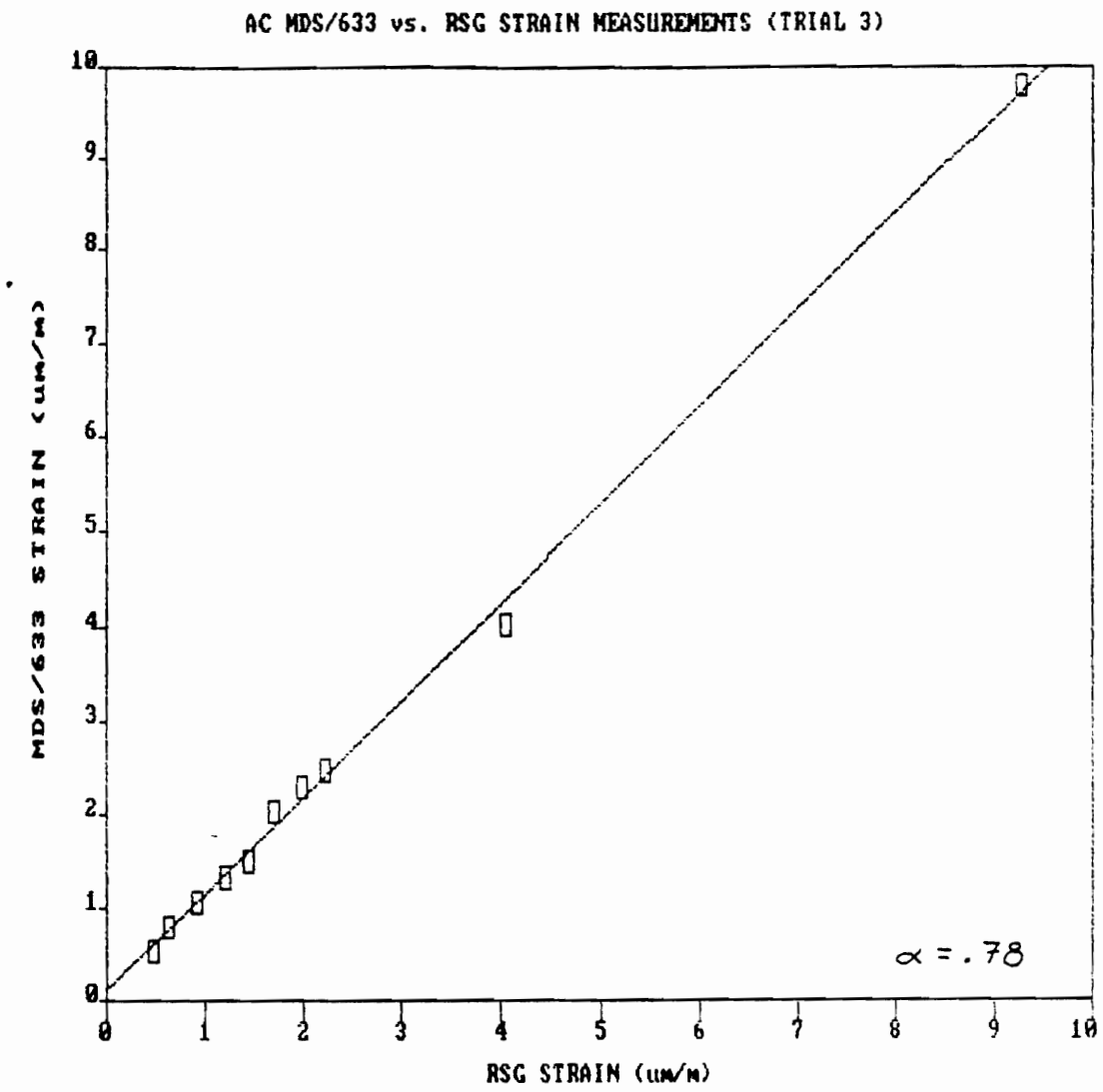

THE REGRESSION POLYNOMIAL OF LINE 1

(1.072E-01) + (1.036E+00)*X
THE VARIANCE = 1.408E-02

Figure 35. MDS/9-633 dynamic strain measurement data (trial 3)

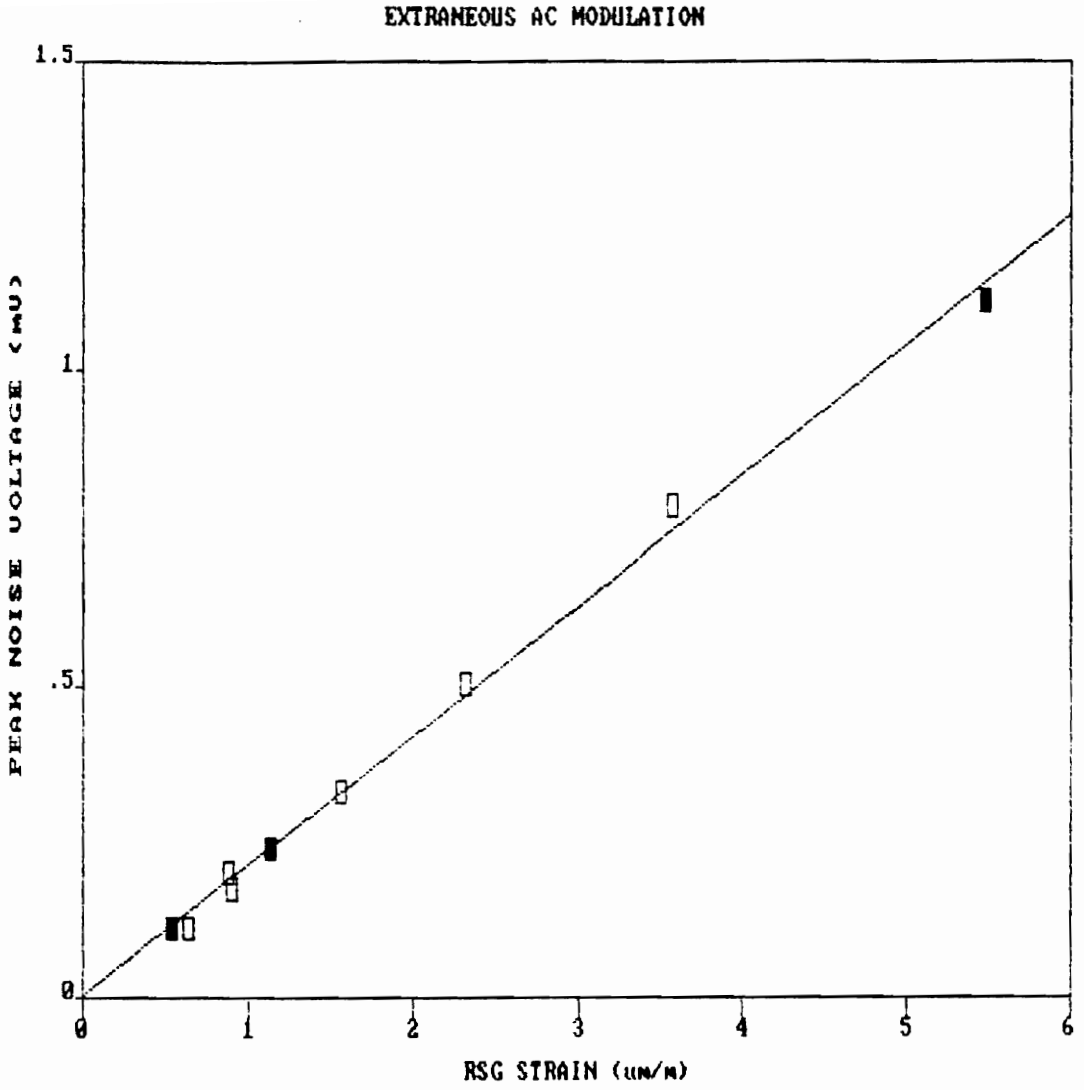

THE REGRESSION POLYNOMIAL OF LINE 1

(2.639E-03) + (2.079E-01)*X
THE VARIANCE = 4.095E-04

Figure 36. Extraneous dynamic modulation

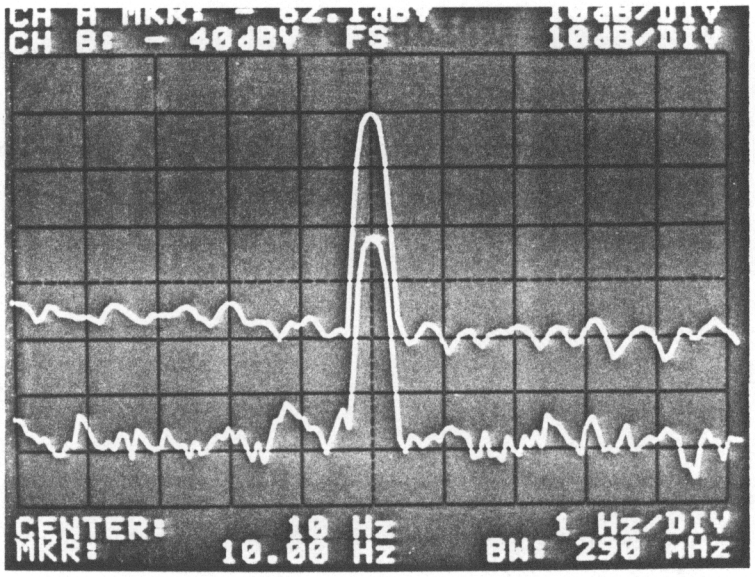

(a)

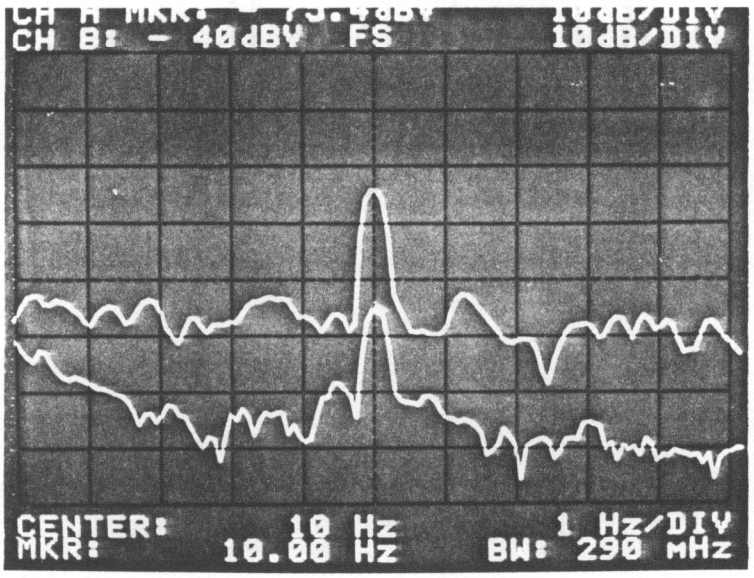

(b)

Figure 37. Extraneous modulation signals for large and moderate excitations

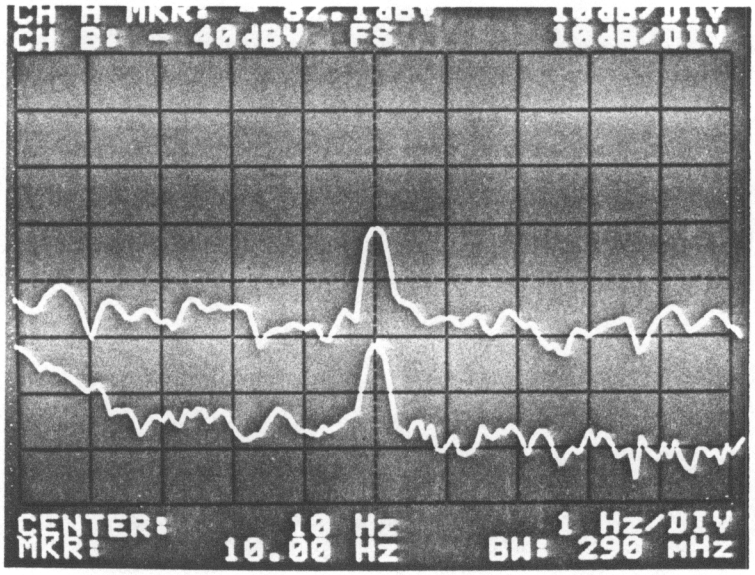

Figure 38. Extraneous dynamic modulation signals for small beam excitation

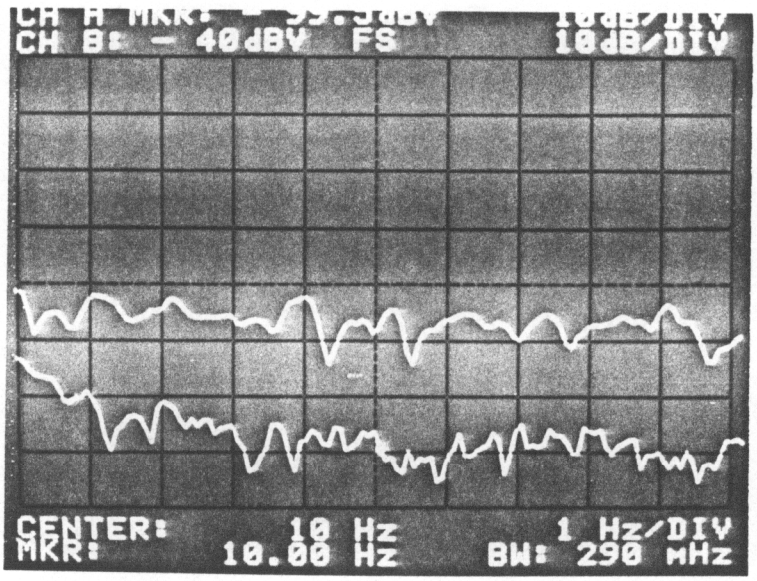

Figure 39. Extraneous dynamic modulation noise floors

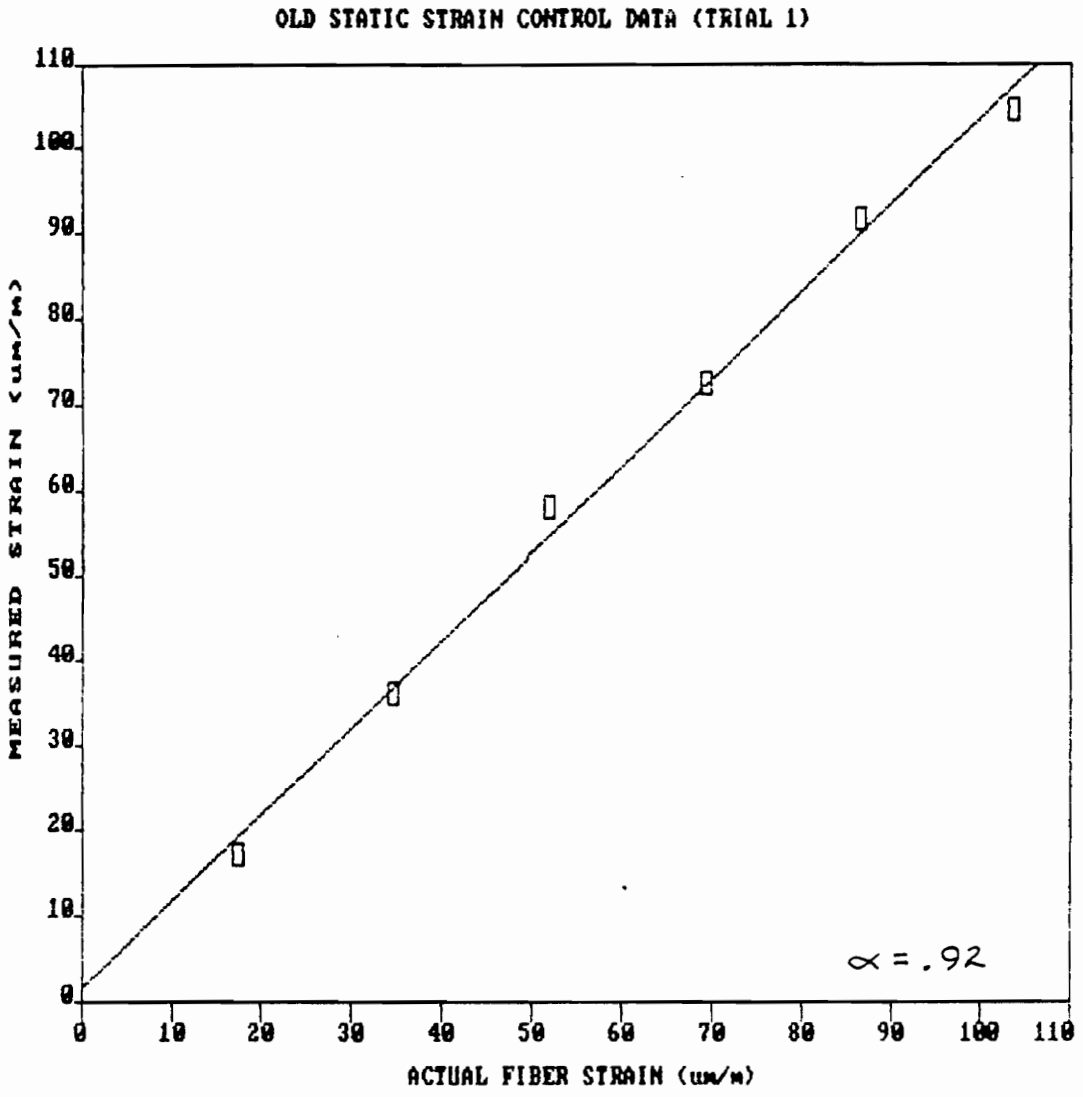

THE REGRESSION POLYNOMIAL OF LINE 1

(1.624E+00) + (1.019E+00)*X
THE VARIANCE - 4.704E+00

Figure 40. MDS/9-633 static strain measurements (first attempt; trial 1)

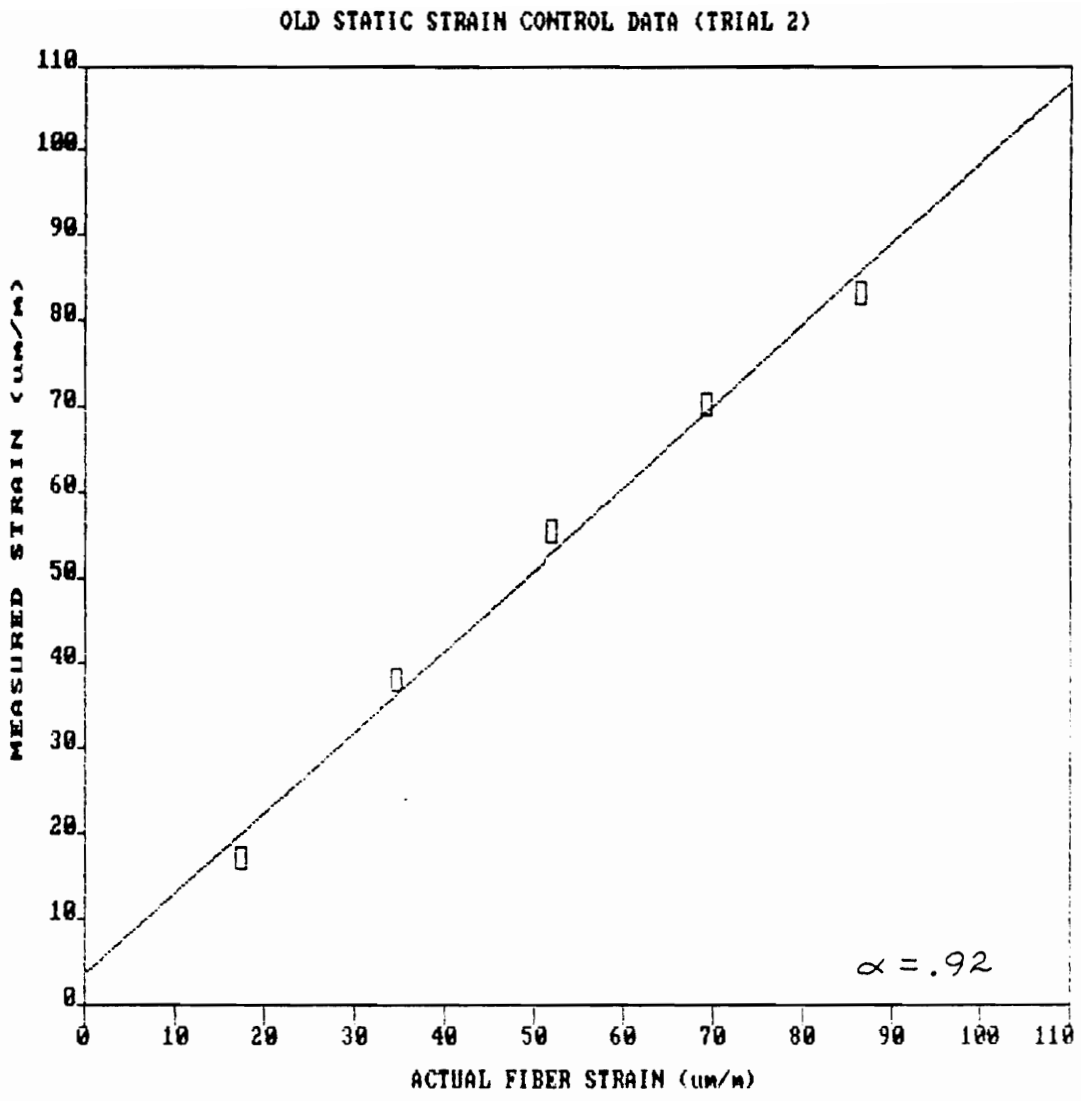

THE REGRESSION POLYNOMIAL OF LINE 1

(3.613E+00) + (9.483E-01)*X
THE VARIANCE = 5.349E+00

Figure 41. MDS/9-633 static strain measurements (first attempt; trial 2)

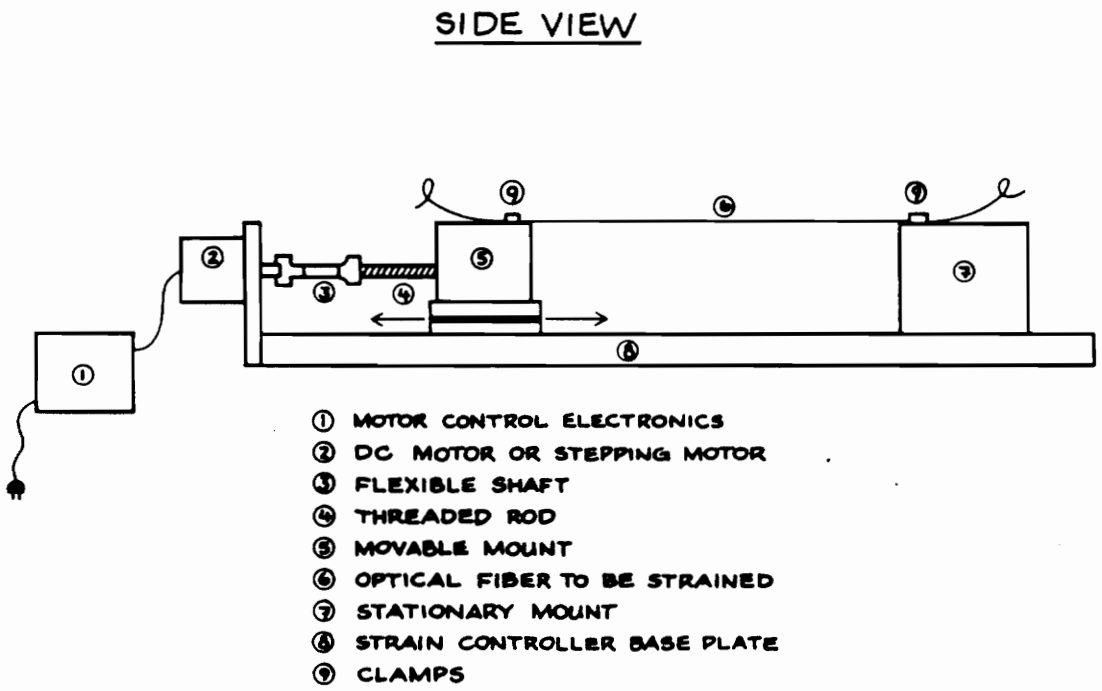

Figure 42. Redesigned static strain control device

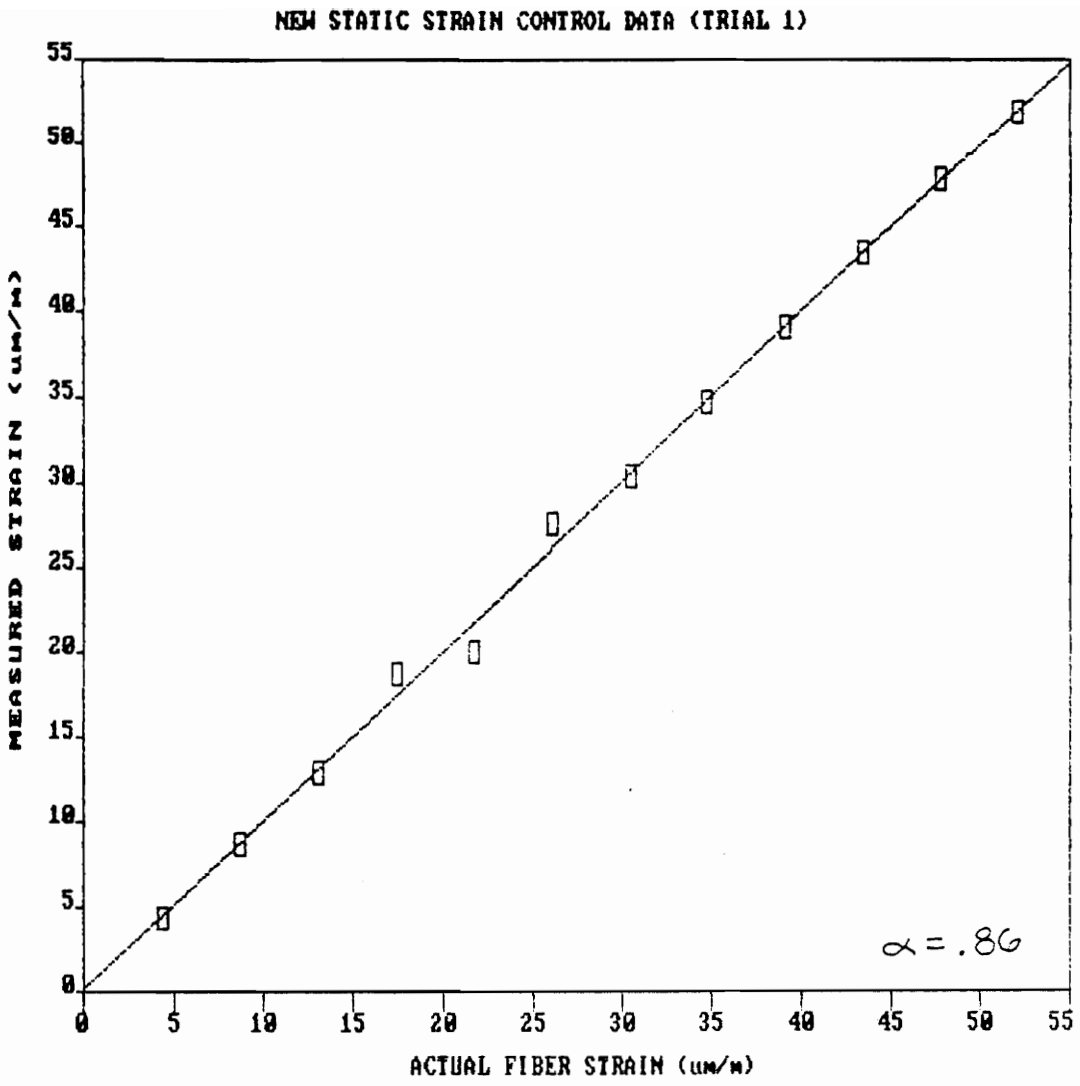

THE REGRESSION POLYNOMIAL OF LINE 1

(1.785E-01) + (9.947E-01)*X
THE VARIANCE - 5.671E-01

Figure 43. MDS/9-633 static strain measurements (second attempt; trial 1)

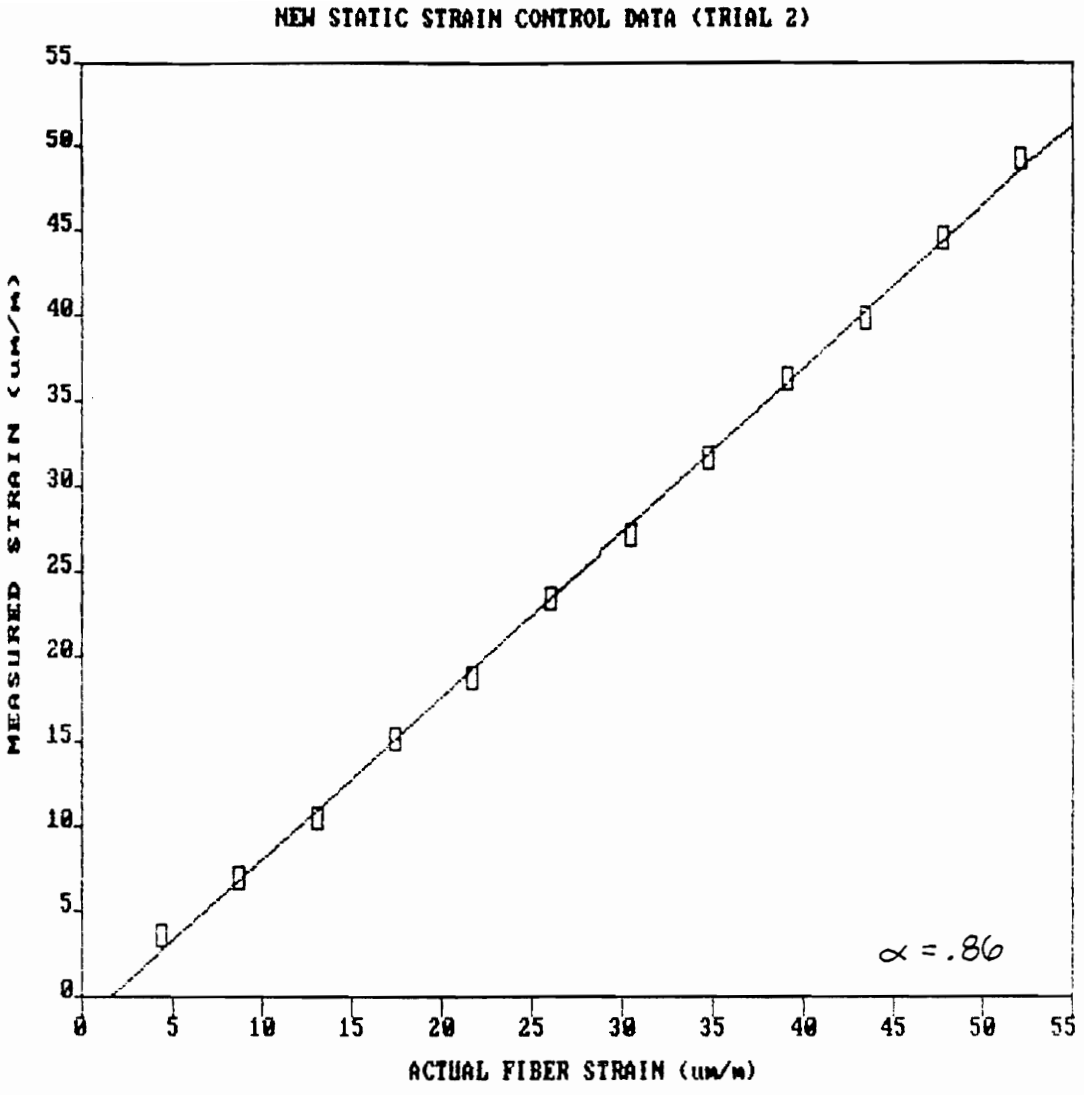

THE REGRESSION POLYNOMIAL OF LINE 1

(-1.527E+00) + (9.597E-01)*X
THE VARIANCE - 2.179E-01

Figure 44. MDS/9-633 static strain measurements (second attempt; trial 2)

5.0 CONCLUSION

Modal domain sensors using 9 μm core diameter fiber at source wavelengths of 633 nm and 850 nm have been thoroughly described. The mode content of the most commonly observed intensity distributions at the fiber/sensor outputs, for each wavelength, have been discussed and the resulting strain modulated behavior of these intensity distributions has been proven from first principles. In addition, it has been shown how this strain modulated behavior may be used as a strain detection mechanism and suggestions have been made concerning how micro-optical components can be used to construct a MDS/9-850 sensor.

The linear and highly sensitive nature of modal domain sensors has also been predicted and experimentally verified for small amounts of strain and the dynamic range of a typical modal domain sensor has been calculated.

Furthermore, the many advantages and disadvantages of the various modal domain techniques have been addressed in great detail.

It is hoped that future work with modal domain sensors will involve a complete experimental evaluation of a MDS/9-850 sensor and that further investigations will result in the realization of additional in-line micro-optical injection/detection techniques for modal domain sensor use. In addition, an independant study into the values of the individual photoelastic coefficients of the optical fiber used in the previously described experiments should be undertaken with a parallel study undertaken to determine the radial changes of the core index of refraction as a function of strain and how this will affect the propagating modes.

Finally, it was assumed in section 4.2 that for quasi-static induced beam vibrations at frequencies well below the fundamental natural frequency of vibration, with small peak beam tip displacements, that the cantilever beam stress-strain relations held just as if the beam was statically loaded, with only a sinusoidal multiplicative factor appearing for the quasi-static strain case. It was also assumed that only the fundamental mode of vibration was excited. Although the corresponding nature of the experimental results and the theoretical predictions as to the behavior of the MDS/9-633 sensor lend

validity to these two assumptions, further investigation may be necessary to finally prove that these assumptions are valid.

APPENDIX A: Strain Characteristics of Loaded Cantilever Beams

One of the simplest and most fundamental ways in which a newly developed strain sensor may be evaluated is by attaching it to the surface of a cantilever beam which is placed under load. If the beam is constructed from some homogeneous material, such as aluminum or steel, then the strain characteristics of the beam are quite easily described as a function of load, thus making the loaded cantilever beam a convenient strain standard. Consider for instance the cantilever beam of Figure 45. Assuming the beam is made of a homogeneous material, the stress at any location on or within the beam is given by

$$\sigma = \frac{M_g z}{I} \quad [Pa] \ , \qquad (A.1)$$

where z is the distance above or below the neutral axis, $M_g = F \times \ell$ is the bending moment and I is the moment of inertia given as

$$I = \frac{h^3 b}{12} \quad . \tag{A.2}$$

If we now consider only the surface which is in tension when the beam is loaded we find that the surface stress σ_{sur} is

$$\sigma_{sur} = \frac{F\ell(h/2)}{hb^3/12} = \frac{6F\ell}{h^2 b} \quad . \tag{A.3}$$

Recalling that strain ε is related to stress by the relation $\varepsilon = \sigma/E$, where E is the modulus of elasticity, we see that the strain along the tensed surface of the cantilever beam is

$$\varepsilon_x(\ell) = \frac{6F\ell}{Eh^2 b} \quad . \tag{A.4}$$

Note that this result indicates that the strain along the surface of the beam increases linearly as a function of ℓ, being zero at the free end and being maximum at the clamped end. The average strain in the beam thus occurs at $\ell = L/2$. Also note that by changing the sign of the strain relation in equation (A.4) one can describe the strain induced in the beam surface being compressed. The negative sign simply indicates the compressional force.

Often, though, one is interested in the change in average strain in a situation where the loading force is changed by varying masses attached to the beam. We will call this change in average strain $\Delta\bar{\varepsilon}$ which is simply given by

$$\Delta\bar{\varepsilon} = \frac{3mgL}{Ebh^2} \quad , \tag{A.5}$$

where m is the change in mass, g is the acceleration due to gravity and the fact that average strain occurs at $\ell = L/2$ has been used. This quantity can easily be measured by a resistive strain gage placed at the geometric center of the beam surface [12].

A.1 Average Strain Induced in an Optical Fiber

In the evaluation of fiber optic strain sensors it is often desirable to loop a sensing length of fiber along a cantilever beam as indicated in Figure 46. Since the output of an optical fiber strain sensor is actually a measure of the *average* strain in the fiber sensor length (more commonly called the gage length) we can calculate the average change in strain, $\Delta\bar{\varepsilon}_f$, to which the fiber is subjected along its path by evaluating

$$\Delta\bar{\varepsilon}_f = \frac{\Delta L}{L_f} = \frac{1}{L_f}\int_0^{L_f} \varepsilon_x \, d\ell \quad , \tag{A.6}$$

where ΔL is the total elongation of the fiber path and L_f is the gage length. Using equation (A.4) we can evaluate ΔL as follows:

$$\Delta L = 2\int_{AB} \varepsilon_x \, d\ell + \int_{BC} \varepsilon_x \, d\ell$$

$$\Delta L = 2\int_{L_1}^{L} \frac{6F\ell}{Eh^2b} \, d\ell + 2r\int_0^{\pi/2} \frac{6F(L_1 - r\cos\phi)}{Eh^2b} \sin\phi \; d\phi$$

$$\Delta L = \frac{6mg}{Eh^2b}(L^2 - L_1^2) + \frac{12mgr}{Eh^2b}\left(L_1 - \frac{r}{2}\right)$$

$$\Delta L = \frac{6mg}{Eh^2b}(L^2 - L_1^2 + 2L_1r - r^2) \quad . \tag{A.7}$$

Note that a simple transformation from rectangular to polar coordinates was necessary to integrate the strain effects in the curved portion of the fiber. Now, by dividing equation (A.7) by the fiber gage length and recalling that m is the change in load mass we find that $\Delta\bar{\varepsilon}_f$ is

$$\Delta\bar{\varepsilon}_f = \frac{6mg}{Eh^2bL_f}(L^2 - L_1^2 + 2L_1r - r^2) \quad , \tag{A.8}$$

where

$$L_f = 2(L - L_1) + \pi r \quad . \tag{A.9}$$

Notice in equation (A.8) that if $r = L_1$ so that the curved portion of fiber just touches the free end of the cantilever beam then

$$\Delta\bar{\varepsilon}_f = \frac{6mg}{Eh^2b}\,\frac{L^2}{L_f} \quad , \tag{A.10}$$

which, if $L_f \simeq 2L$, is approximately the same result expressed in equation (A.5). More precisely, if we choose L_1, L and r properly, it is possible to make the results of equations (A.5) and (A.8) express the same quantity. Assuming L and L_1 to be fixed, we can solve for r as follows:

$$\frac{6mg}{Eh^2bL_f}(L^2 - L_1^2 + 2rL_1 - r^2) = \frac{3mgL}{Ebh^2}$$

$$L^2 - L_1^2 + 2rL_1 - r^2 = \frac{L}{2}\left(2(L - L_1) + \pi r\right)$$

$$r^2 - r\left(2L_1 - \frac{\pi L}{2}\right) - (L_1L - L_1^2) = 0$$

$$r = \left(L_1 - \frac{\pi L}{4}\right) + \left\{L_1 L\left(1 - \frac{\pi}{2}\right) + \left(\frac{\pi L}{4}\right)^2\right\}^{1/2} . \qquad (A.11)$$

These last considerations are interesting in that they demonstrate that by using simply loaded cantilever beams an optical fiber strain sensor can be subjected to known strain effects while having its performance evaluated simultaneously against more commonly used strain sensors such as resistive strain gages. Finally, it should be mentioned that due to the relatively insensitive nature of both resistive strain gages and optical fibers to transverse strain, no considerations in the previous formulations have been given to transverse beam contractions [13].

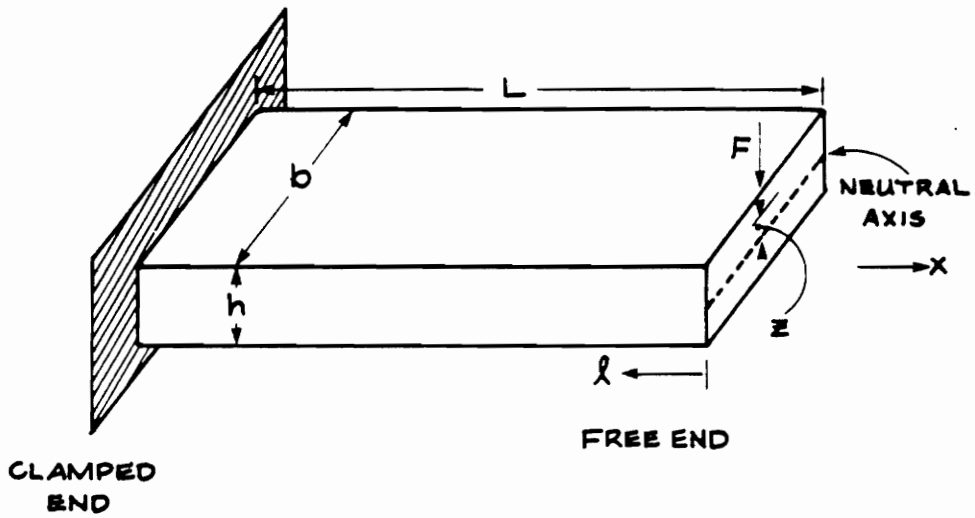

Figure 45. Cantilever beam geometry

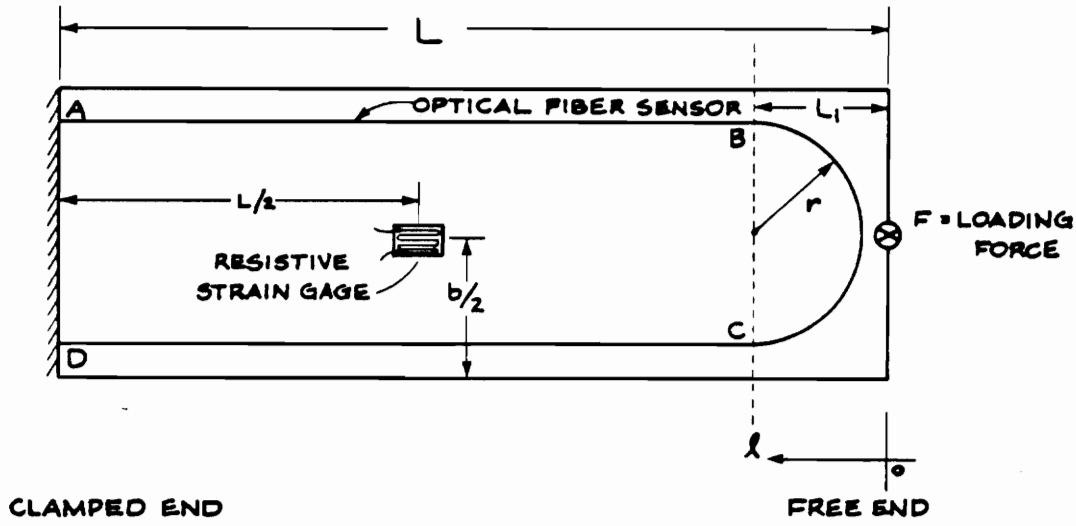

L = CANTILEVER BEAM LENGTH
$L-L_1$ = LENGTH OF FIBER WHICH IS STRAIGHT
b = BEAM WIDTH
r = RADIUS OF CURVED FIBER SECTION

Figure 46. Optical fiber and resistive strain gage placement parameters

APPENDIX B: The Resistive Strain Gage

Lord Kelvin first observed that a change in strain imposed on a wire is accompanied by a change in resistance ΔR of the wire. The relationship between resistance change ΔR and strain ε can be derived by considering a uniform conductor of length L, cross-sectional area A, and resistivity ρ. The resistance R of such a conductor is given by

$$R = \frac{\rho L}{A} \quad . \tag{B.1}$$

Differentiating equation (B.1) and dividing by R gives

$$\frac{dR}{R} = \frac{d\rho}{\rho} + \frac{dL}{L} - \frac{dA}{A} \quad . \tag{B.2}$$

However,

$$\frac{dA}{A} = -2\nu\frac{dL}{L} + \nu^2\left(\frac{dL}{L}\right)^2 \qquad (B.3)$$

under elastic deformations where ν is the Poisson's ratio of the conductor material. The strain sensitivity S_A of the conductor is defined as

$$S_A = \frac{dR/R}{dL/L} \quad . \qquad (B.4)$$

Substituting equations (B.2) and (B.3) into equation (B.4) gives us

$$S_A = \frac{d\rho/\rho}{dL/L} + 1 + 2\nu - \nu^2\left(\frac{dL}{L}\right) \quad . \qquad (B.5)$$

The last three terms of equation (B.5) are due to dimensional changes in the conductor. The first term is due to changes of resistivity with strain. The last term is usually neglected for elastic strains since it is small ($< 0.1\varepsilon$) compared to the other terms (~ 1.60). The derivation of (B.5) is modified slightly for large strains since the conductor undergoes plastic deformation [13].

B.1 Strain Gage Calibration

In practice equation (B.5) is not very useful since it is only valid for a single filament conductor and because the first factor which describes the change of resistivity with respect to strain is often unknown. Typically the conductor of a resistive strain gage is formed into a grid to reduce its size as shown in Figure 47. This causes the gage to exhibit sensitivity to both axial and transverse strain. The response of a surface mounted gage that is subjected to a axial strain ε_a, a transverse strain ε_t and a shearing strain γ_{at} can be expressed by

$$\frac{dR}{R} = S_a\varepsilon_a + S_t\varepsilon_t + S_s\gamma_{at} \quad , \tag{B.6}$$

where S_a, S_t *and* S_s are the sensitivities of the gage to axial, transverse and shearing strains, respectively. In general, the gage sensitivity to shearing strain is small and thus neglected so that

$$\frac{dR}{R} = S_a(\varepsilon_a + k_t\varepsilon_t) \quad , \tag{B.7}$$

where $k_t = S_t/S_a$ is defined as the transverse sensitivity factor for the gage.

Strain gage manufacturers provide the transverse sensitivity factor k_t and a calibration constant known as the gage factor for each gage. The gage factor S_g represents the calibration constant for a batch or lot of gages and is determined by testing sample gages drawn from a lot of gages in a given production run. Resistance change dR experienced by a gage is related to the gage factor and the axial strain by

$$\frac{dR}{R} = S_g \varepsilon_a \quad . \tag{B.8}$$

The stress field in the calibration beam used for the determination of S_g is always unaxial; therefore, the gage is subjected to a biaxial strain of

$$\varepsilon_t = -\nu_0 \varepsilon_a \quad , \tag{B.9}$$

where $\nu_0 = 0.285$ is Poisson's ratio for the calibration beam material. Substituting equation (B.9) into equation (B.7) and comparing with equation (B.8) yields

$$S_g = S_a(1 - k_t \nu_0) \quad ,$$

or

$$S_a = \frac{S_g}{1 - k_t \nu_0} \quad . \tag{B.10}$$

Therefore when the strain gage is used to measure unaxial strain in a material other than the calibration beam we see that

$$\frac{dR}{R} = \frac{S_g}{1 - k_t \nu_0}(\varepsilon_a + k_t \varepsilon_t) = \frac{S_g \varepsilon_a}{1 - k_t \nu_0}(1 - k_t \nu)$$

or

$$\varepsilon_a = \frac{dR}{R}\left(\frac{1 - k_t \nu_0}{1 - k_t \nu}\right)\frac{1}{S_g} \quad , \tag{B.11}$$

where ν is the Poisson's ratio of the structure to which the strain gage is attached. It should be evident from equation (B.11) that the calibration procedure used to determine k_t *and* S_g allows transverse strain effects to be "calibrated out" of the actual strain gage measurement [13]. Also, it should be evident that the change in average strain in a loaded cantilever beam as described in Appendix A could be measured using a resistive strain gage placed in the geometric center of the beam by using the relation

$$\Delta\bar{\varepsilon} = \frac{\Delta R}{R}\left(\frac{1 - k_t \nu_0}{1 - k_t \nu}\right)\frac{1}{S_g} \quad , \tag{B.12}$$

where R is the initial gage resistance (often measured), ν is Poisson's ratio of the test material and ΔR is the measured change in gage resistance.

B.2 The Use of Wheatstone Bridges to Measure ΔR

In order to enable small changes in strain and therefore small changes in resistance to be measured in a resistive strain gage, a Wheatstone bridge circuit with an amplifier output stage is often used. A constant-voltage excitation Wheatstone bridge circuit is shown in Figure 48. For this bridge circuit, the error voltage E_o is given by

$$E_0 = \frac{R_1R_3 - R_2R_4}{(R_1 + R_2)(R_3 + R_4)} V_{in} \quad . \tag{B.13}$$

Equation (B.13) indicates that the initial error voltage will vanish ($E_o = 0$) if

$$R_1R_3 = R_2R_4 \quad . \tag{B.14}$$

When equation (B.14) is satisfied, the bridge is said to be balanced. This means that the small unbalanced voltage caused by a change in resistance of any arm of the bridge is measured from a zero or near-zero condition. This small signal can easily be amplified to significant levels for recording.

If a single resistive strain gage is placed in the bridge circuit a indicated in Figure 48, a voltage ΔE_o developes at the input to the amplifier stage when the nominal resistance of the gage R is changed by an amount ΔR. Such changes

in resistance are in general due to strain or temperature variations; however, in the following analysis the change in ΔR due to temperature effects will be assumed negligible.

If the fixed resistors R_2, R_3 and R_4 are chosen to have the same resistance value as the nominal resistance R of the resistive strain gage, we have that

$$\Delta E_0 = \frac{1}{4} \frac{\Delta R}{R} (1 - \eta) V_{in} \quad , \tag{B.15}$$

where

$$\eta = \frac{\Delta R/R}{\Delta R/R + 2} \quad . \tag{B.16}$$

Substituting equation (B.16) into equation (B.15) we find that

$$\Delta E_0 = \frac{1}{4} \frac{\Delta R}{R} \left(1 - \frac{\Delta R/R}{\Delta R/R + 2} \right) V_{in}$$

$$\Delta E_0 = \frac{1}{4} \frac{\Delta R}{R} \left(\frac{2}{\Delta R/R + 2} \right) V_{in}$$

$$\Delta E_0 \simeq \frac{1}{4} \frac{\Delta R}{R} \left(1 - \frac{\Delta R}{2R} \right) V_{in} \quad ,$$

where the binomial expansion $(1 + a)^{-1} \simeq (1 - a)$ has been used since typically $\Delta R << R$. Continuing,

$$\Delta E_0 = \frac{1}{4} \frac{\Delta R}{R} V_{in} - \frac{\Delta R^2}{8R^2} V_{in} \quad . \tag{B.17}$$

Since the second term of equation (B.17) is very much smaller that the first, we have

$$\Delta E_0 = \frac{1}{4} \frac{\Delta R}{R} V_{in} \quad . \tag{B.18}$$

The output of the inverting amplifier is then given by the relation

$$V_{out} = -\frac{R_6}{R_5} \Delta E_0 = -\frac{1}{4} \frac{R_6}{R_5} \frac{\Delta R}{R} V_{in} \quad , \tag{B.19}$$

where R_5 is chosen large enough so as not to cause significant loading of the bridge network and where a near-zero initial condition is assumed for ΔE_0 (i.e., the bridge is assumed to be initially balanced) [14].

By substituting equation (B.12) into equation (B.19) and then rearranging terms we find that the change in average strain induced in a resistive strain gage is given by

$$\Delta\bar{\varepsilon} = -\frac{V_{out}}{V_{in}} \frac{4R_5}{S_g R_6} \left[\frac{1 - k_t \nu_0}{1 - k_t \nu} \right] . \qquad (B.20)$$

Due to the linear nature of resistive strain gages, Wheatstone bridges and simple inverting amplifiers, the peak change in average strain as induced in a resistive strain gage by a sinusoidally varying strain field is given by

$$\Delta\bar{\varepsilon}_p = \frac{V_p}{V_{in}} \frac{4R_5}{S_g R_6} \left[\frac{1 - k_t \nu_0}{1 - k_t \nu} \right] , \qquad (B.21)$$

where the negative sign has been dropped in equation (B.21) since V_p, which represents the amplitude of the sinusoidally varying output voltage, is independant of phase. Considering once again the case of measuring the change in average strain in a cantilever beam we see that equation (B.20) will be most useful when the beam is subjected to a static load and that equation (B.21) will be most useful when the beam is forced to vibrate under the influence of a sinusoidally varying load.

Finally, in order to investigate the minimum detectable strain for a resistive strain gage used in a detection network such as that of Figure 48, we differentiate equation (B.21) and divide by $\Delta\bar{\varepsilon}_p$ to obtain

$$\frac{d\Delta\bar{\varepsilon}_p}{\Delta\bar{\varepsilon}_p} = \frac{dV_p}{V_p} + \frac{dR_5}{R_5} - \frac{dV_{in}}{V_{in}} - \frac{dS_g}{S_g} - \frac{dR_6}{R_6} , \qquad (B.22)$$

where in equation (B.21) k_t, ν_0 and ν are assumed to be constant and where dR_5, dR_6 and dS_g represent manufacturer stated tolerances on the values R_5, R_6 and S_g, respectively. Also, dV_p and dV_{in} represent the inaccuracies of measuring V_p *and* V_{in} on, say, digital voltmeters, oscilloscopes or spectrum analizers. By then setting the ratio $d\Delta\bar{\varepsilon}_p/\Delta\bar{\varepsilon}_p$ equal to unity and solving for V_p we will have a minimum value of V_p needed for reliable measurements which when substituted into equation (B.21) will give the minimum reliable value of $\Delta\bar{\varepsilon}_p$. Minimum detectable strain values on the order of 10^{-6} are not uncommon for resistive strain gages used in typical measurement situations, with higher sensitivities expected in controled laboratory environments [13].

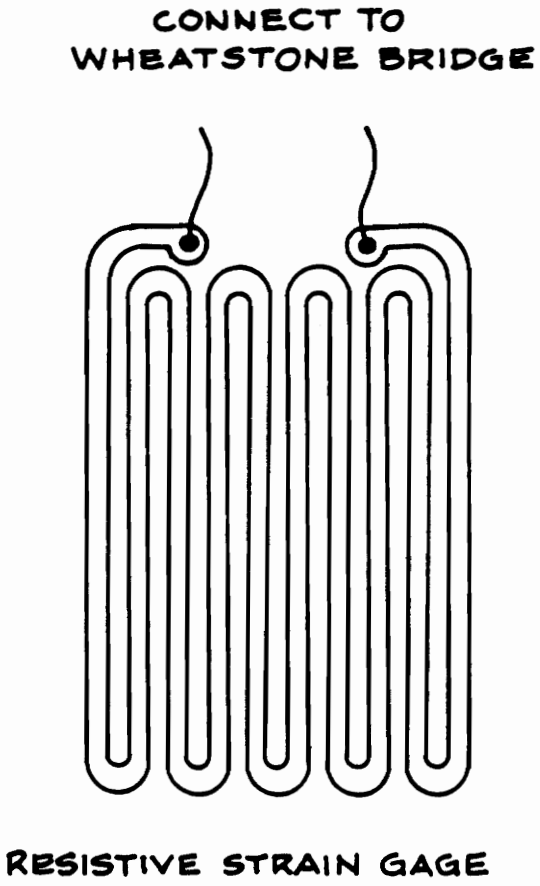

Figure 47. A resistive strain gage

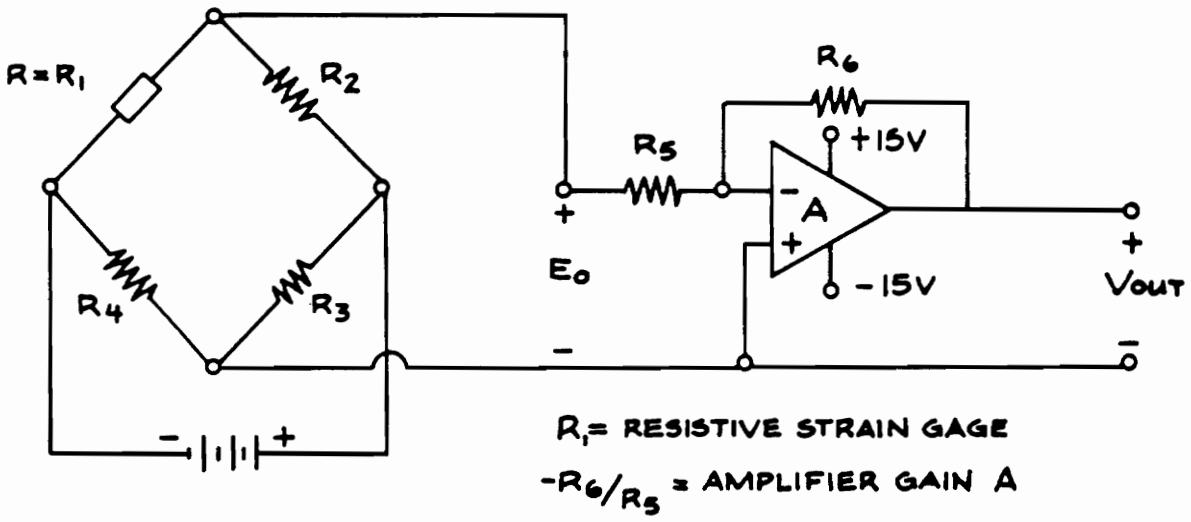

Figure 48. A Wheatstone bridge circuit with amplifier

APPENDIX C: Bessel Function Numerical Expansions

The following numerical expansions for $J_0(x)$ and $J_1(x)$ can be used to aid in plotting modal intensity patterns [15]:

$$J_0(x) = 1 - A\left(\frac{x}{3}\right)^2 + B\left(\frac{x}{3}\right)^4 - C\left(\frac{x}{3}\right)^6 + D\left(\frac{x}{3}\right)^8 - E\left(\frac{x}{3}\right)^{10} + F\left(\frac{x}{3}\right)^{12} ,$$

where

$$A = 2.2499997$$

$$B = 1.2656208$$

$$C = 0.3163866$$

$$D = 0.0444479$$

$$E = 0.0039444$$

$$F = 0.0002100$$

and

$$x^{-1}J_1(x) = 0.5 - G\left(\frac{x}{3}\right)^2 + H\left(\frac{x}{3}\right)^4 - I\left(\frac{x}{3}\right)^6 + J\left(\frac{x}{3}\right)^8 - K\left(\frac{x}{3}\right)^{10} + L\left(\frac{x}{3}\right)^{12} ,$$

where

$$G = 0.56249985$$

$$H = 0.21093573$$

$$I = 0.03954289$$

$$J = 0.00443319$$

$$K = 0.00031761$$

$$L = 0.00001109$$

These expansions give eight significant digits for $-3 \leq x \leq 3$. For reasonable departures of $|x| \geq 3$ these expansions also give very good results for plotting purposes.

APPENDIX D: FORTRAN Programs

The following FORTRAN programs are useful for generating the data needed to create the line and surface plots of the various intensity distributions of interest in modal domain sensing.

```
CCCCCCCCCCCCCCCCCCCCCCCCCCCCCCCCCCCCCCCCCCCCCCCCCCCCCCCCCCCCCCCCCCCCCCCCCC
C                                                                       C
C     THIS PROGRAM GENERATES THE VALUES WHICH WHEN PLOTTED RESULT       C
C     IN THE LINE PLOTS WHICH DESCRIBE THE TWO LOBE PATTERN OF          C
C     INTEREST IN MODAL DOMAIN SENSING                                  C
C                                                                       C
CCCCCCCCCCCCCCCCCCCCCCCCCCCCCCCCCCCCCCCCCCCCCCCCCCCCCCCCCCCCCCCCCCCCCCCCCC
C
      REAL J0(100),J1(100),XVAL(100),I,J,K,L
C
      A = 0.56249985
      B = 0.21093573
      C = 0.03954289
      D = 0.00443319
      E = 0.00031761
      F = 0.00001109
      G = 2.2499997
      H = 1.2656208
      I = 0.3163866
      J = 0.0444479
      K = 0.0039444
      L = 0.0002100
C
      RBAR = -4.59
C
     DO 10 N = 1,100
C
           RBAR = RBAR + 0.09
           XVAL(N) = RBAR
           X1 = .628*RBAR/3.0
           X0 = .400*RBAR/3.0
C
           J0(N) = 1.0 - G*(X0**2) + H*(X0**4) - I*(X0**6)
     $                 + J*(X0**8) - K*(X0**10) + L*(X0**12)
C
           J1(N) = (0.5 - A*(X1**2) + B*(X1**4) - C*(X1**6)
     $                + D*(X1**8) - E*(X1**10) - F*(X1**12))
     $                *3.0*X1
C
  10  CONTINUE
C
     DO 20 N = 1,100
C
           OUT =   (J0(N)**2)
     $           + (J1(N)**2)
     $           + (2.0*J0(N)*J1(N))
C
           WRITE(08,*) XVAL(N),OUT
C
  20  CONTINUE
C
      STOP
      END
```

```
CCCCCCCCCCCCCCCCCCCCCCCCCCCCCCCCCCCCCCCCCCCCCCCCCCCCCCCCCCCCCCCCCCCCCCCCCCC
C                                                                           C
C                                                                           C
C     THIS PROGRAM CALCULATES THE VALUES WHICH WHEN PLOTED CREATE           C
C     THE THREE LOBE PATTERN OF INTEREST IN MODAL DOMAIN SENSING.           C
C     NOTE THAT THIS ROUTINE EXHIBITS HIGHEST ACCURACY WHEN THE             C
C     ARGUMENTS OF THE BESSEL FUNCTIONS ARE IN THE RANGE (-3,3).            C
C                                                                           C
C     (THIS ROUTINE USES THE LP11 AND LP21 EVEN AND ODD MODES!!!)           C
C                                                                           C
C         **************************************************                C
C       **                                                  **              C
C      ***  GO DOWN 38 LINES TO CHANGE PLOT PARAMETERS!!!  ***             C
C       **                                                  **              C
C         **************************************************                C
C                                                                           C
C                                                                           C
CCCCCCCCCCCCCCCCCCCCCCCCCCCCCCCCCCCCCCCCCCCCCCCCCCCCCCCCCCCCCCCCCCCCCCCCCCC
C
      IMPLICIT DOUBLE PRECISION (A-Z)
      INTEGER N,M
C
      A = 0.56249985D0
      B = 0.21093573D0
      C = 0.03954289D0
      D = 0.00443319D0
      E = 0.00031761D0
      F = 0.00001109D0
      G = 2.24999970D0
      H = 1.26562080D0
      I = 0.31638660D0
      J = 0.04444790D0
      K = 0.00394440D0
      L = 0.00021000D0
C
      PI = 3.141592654D0
C
CCCCCCCCCCCCCCCCCCCCCCCCCCCCCCCCCCCCCCCCCCCCCCCCCCCCCCCCCCCCCCCCCCCCCCCCCCC
C                                                                           C
C                                                                           C
C                                                                           C
C      CHANGE THESE PARAMETERS TO MODIFY THE PLOTS COMPLETELY.              C
C      A1 AND A2 ARE THE AMPLITUDE TERMS.  DTHETA IS THE RELATIVE           C
C      PHASE TERM AND Z IS SOME DISTANCE ALONG THE FIBER.                   C
C      (PHOTOELASTICITY IS NOT CONSIDERED IN THIS PROGRAM.)                 C
C                                                                           C
C                                                                           C
                           A1   = 1.0D0
                           A2   = 1.0D0
                       DTHETA = 0.00D0
                           Z    = 0.00D-4
C                                                                           C
C                                                                           C
C                                                                           C
C                                                                           C
```

```
CCCCCCCCCCCCCCCCCCCCCCCCCCCCCCCCCCCCCCCCCCCCCCCCCCCCCCCCCCCCCCCCCCCCCCCCCCC
C
      B1 = 1.20D4
C
      X = -4.7501D0
      Y = -4.7501D0
C
      DO 10 N = 1,37
            X = X + 0.25D0
            DO 20 M = 1,37
                  Y = Y + 0.25D0
C
                  RSQR = (X**2) + (Y**2)
                  RBAR = DSQRT(RSQR)
                  PHI = DATAN2(X,Y)
C
                  X1 = .688D0*RBAR/3.0D0
                  X2 = .906D0*RBAR/3.0D0
C
                  J02 = 1.0D0 - G*(X2**2) + H*(X2**4) - I*(X2**6)
     $                        + J*(X2**8) - K*(X2**10) + L*(X2**12)
C
                  J12 = (0.5D0 - A*(X2**2) + B*(X2**4) - C*(X2**6)
     $                         + D*(X2**8) - E*(X2**10) + F*(X2**12))
     $                         *3.0D0*X2
C
                  J2 = (J12*2.0D0/(X2*3.0D0)) - J02
C
                  J1 = (0.5D0 - A*(X1**2) + B*(X1**4) - C*(X1**6)
     $                        + D*(X1**8) - E*(X1**10) + F*(X1**12))
     $                        *3.0D0*X1
C
                  INTENS =
     $                    ((A1*J1)**2)
     $                  + ((A2*J2)**2)
     $                  + (2.0D0*A1*A2*J1*J2*DCOS(3.0D0*PHI
     $                                            - B1*Z + DTHETA))
C
                  WRITE(8,*) X,Y,INTENS
C
  20          CONTINUE
C
      Y = -4.7501D0
C
  10  CONTINUE
C
      STOP
      END
```

References

1. Butter, C.D. and G.B. Hocher; *Fiber Optics Strain Gage,* Applied Optics, Vol. 17, No. 18, 15 September 1987.

2. Culshaw, Brian; *Optical Fibre Sensing and Signal Processing,* Peter Peregrinus Ltd., London, 1984.

3. Shankaranarayanan, N.K.; *Mode-Mode Interference In Optical Fibers: Analysis and Experiment,* M.S. Thesis, VPI, 12 March 1987.

4. Shankaranarayanan, N.K., et. al.; *Mode-Mode Interference in Axially Strained Few-Mode Optical Fibers,* Proceedings, SPIE, San Diego, CA, August, 1987.

5. Ehrenfeuchter, P.A.; *Modal Domain Detection of Vibration in Beams,* M.S. Thesis, VPI, December 1986.

6. Shankaranarayanan, N.K., et. al.; *Optical Fiber Modal Domain Detection of Stress Waves,* Proceedings, IEEE Ultrasonics Symposium, Williamsburg, VA, November 1986.

7. Cherin, Allen H.; *An Introduction to Optical Fibers,* McGraw-Hill Book Company, New York, 1983.

8. Safaai-Jazi, A.; *Optical Waveguide Theory (EE:5980 Class Notes),* VPI Department of Electrical Engineering, Fall Quarter, 1987.

9. Keiser, Gerd; *Optical Fiber Communications,* McGraw-Hill Book Company, New York, 1983.

10. Gloge, D.; *Weakly Guiding Fibers,* Applied Optics, Vol. 10, No. 10, October 1971, p. 2252.

11. Safaai-Jazi, A.; *A Study of Interference Patterns in Few-Mode Optical Fibers,* Internal Report, VPI Department of Electrical Engineering, December 1987.

12. Timoshenko, S.; *Strength of Materials,* D. Van Nostrand Company, Inc., New York, 1940.

13. Kobayashi, Albert S., ed.; *Handbook on Experimental Mechanics,* Prentice-Hall, Inc., Englewood Clifts, NJ, 1987.

14. Nilsson, James W.; *Electric Circuits,* Addison-Wesley Publishing Co., London, 1983.

15. Abramowitz, Milton and Irene Stegun, eds.; *Handbook of Mathematical Functions,* Dover Publications Inc., New York, 1972.

16. *Designers Guide to Fiber Optics,* AMP Incorporated, Harrisburg, PA, 1982.

Vita

Bradley D. Duncan was born in Bristol, Tennessee, on June 4, 1963 and attended Abingdon High School in Abingdon, Virginia. He received the B.S. and M.S. degrees in Electrical Engineering From Virginia Polytechnic Institute and State University in June, 1986 and May, 1988, respectively. His research interests include intrinsic fiber optic sensor techniques and optical fiber sensor system design.

Mr. Duncan is a member of the IEEE Lasers and Electro-Optics Society.